

1 **Tropical upper tropospheric trends in ozone and carbon** 2 **monoxide (2005–2020): observational and model results**

3 Lucien Froidevaux¹, Douglas E. Kinnison², Benjamin Gaubert², Michael J. Schwartz¹, Nathaniel
4 J. Livesey¹, William G. Read¹, Charles G. Bardeen², Jerry R. Ziemke^{3,4}, and Ryan A. Fuller¹

5 ¹Jet Propulsion Laboratory, California Institute of Technology, Pasadena, California, USA

6 ²NSF National Center for Atmospheric Research (NSF NCAR), Boulder, Colorado, USA

7 ³NASA Goddard Space Flight Center, Greenbelt, MD, USA

8 ⁴Goddard Earth Sciences Technology and Research (GESTAR)/Morgan State University,
9 Baltimore, MD, USA

10 *Correspondence to:* Lucien Froidevaux (lucienf@jpl.nasa.gov)

11 **Abstract.** We analyze tropical ozone (O₃) and carbon monoxide (CO) distributions in the upper
12 troposphere (UT) and their temporal changes for 2005–2020 using Aura Microwave Limb Sounder
13 (MLS) observations and chemistry climate model simulations. The simulations are from the Whole
14 Atmosphere Community Climate Model (WACCM6) and two variants of the Community
15 Atmosphere Model with Chemistry (CAM-chem), each variant using different anthropogenic
16 emissions for CO. Upper tropospheric trends and variability diagnostics are obtained from multiple
17 linear regression analyses.

18 We compare the model and MLS annual climatologies, focusing on 147 and 215 hPa pressure
19 levels; the model abundances are typically ~5–15% smaller than MLS O₃ at 215 hPa, but larger
20 than the MLS values at 147 hPa by ~20%. MLS O₃ has an averaged UT zonal mean trend at 20°S–
21 20°N of $+0.39 \pm 0.28$ %yr⁻¹; the WACCM simulation (WACCM-CEDS) and both CAM-chem
22 simulations have similar trends, although the WACCM-CEDS result is somewhat smaller. Our
23 analyses for specific latitude/longitude bins yield positive O₃ trends up to 1.4 %yr⁻¹ over Indonesia
24 and East of that region, as well as over tropical Africa and the tropical Atlantic. Positive tropical
25 UT mapped O₃ trends are generally captured by the model simulations, although in a more muted
26 way. We find broad similarities (and some differences) between the mapped MLS-derived UT O₃
27 trends and corresponding mapped trends of tropospheric column ozone.

28 Regarding UT CO, the model climatologies generally show an underestimate versus the MLS
29 climatology, with model average biases usually about -10% to -20%. Also, in the northern
30 hemisphere tropics, we find significantly poorer model fits to the observed phasing of CO seasonal
31 changes at 215 hPa than at 147 hPa. This discrepancy is much smaller for the comparison of

32 modeled and Measurements of Pollution in the Troposphere (MOPITT) V9J CO columns. We also
33 find that the sensitivity of UT CO to El Niño / Southern Oscillation (ENSO) is positive at all
34 tropical longitudes, in contrast to the dipolar longitudinal structure that exists for UT O₃ ENSO
35 sensitivity. The MLS zonal mean CO UT trend is $-0.25 \pm 0.30 \text{ \%yr}^{-1}$, whereas the corresponding
36 model CO trends are close to zero ($0.0 \pm 0.14 \text{ \%yr}^{-1}$) when the anthropogenic emissions used in
37 CAM-chem and WACCM are taken from Community Emissions Data System (CEDDS) version 2.
38 The non-CEDDS version of CAM-chem (the CAM-chem-CAMS simulation) yields averaged CO
39 UT trends of $0.22 \pm 0.19 \text{ \%yr}^{-1}$, in contrast to the negative tendencies prevalent in the MLS CO
40 trends throughout the tropics. The negative MLS tropical UT CO trends for 2005–2020 agree with
41 (but tend to be smaller in magnitude than) previously published total column CO trends.

42 The MLS-derived upper tropospheric tropical trends in O₃ and CO arise from a well-sampled
43 multi-year data set, with the results showing a first-order correlation to large-scale changes in
44 lower tropospheric composition (O₃ increases and CO decreases). We find that there are
45 similarities (and a few differences) between the measured UT trends and corresponding results
46 from model simulations, which incorporate state-of-the-art representations of the complex
47 interplay between emissions, photochemistry, convection, and transport in the upper troposphere
48 and lower stratosphere. These results will contribute to the continuing assessments of tropospheric
49 evolution, in particular the large community efforts regarding TOAR-II and CMIP-7.

50 **1 Introduction**

51 Tropospheric ozone (O₃) can be influenced by downward transport from the stratospheric ozone
52 layer, but the main O₃ source in the troposphere is in situ photochemical formation through the
53 oxidation of carbon compounds in the presence of (catalyzing) nitrogen oxides (NO_x = NO + NO₂)
54 (Crutzen, 1973; Logan, 1985); tropospheric ozone loss is dominated by in situ photochemistry and
55 by deposition at the Earth's surface (Monks et al., 2015). Past studies have also shown that the
56 main sources of tropospheric NO_x are fossil fuel combustion, biomass burning, soil microbial
57 activity, and lightning. Global anthropogenic emissions dominate the natural NO_x sources and
58 biomass burning plays quite a significant role in the tropics. There is evidence from in situ
59 measurements from ozonesondes and commercial aircraft for slow increases in tropospheric and
60 upper tropospheric O₃ abundances (e.g., Cooper et al., 2014; Gaudel et al., 2020; Thompson et al.,
61 2021; Wang et al., 2022). At the surface, regional differences have been noted, for example, a

62 leveling off in ozone increases over western Europe and parts of the United States after the 1990s,
63 including some decreases, depending on the season. Changes in tropospheric ozone precursor
64 emissions (e.g., from NO_x, carbon monoxide – CO, and volatile organic compounds) have been
65 implicated as causes for global tropospheric ozone change over the past few decades (Zhang et al.,
66 2016; Zheng et al., 2018; Liu et al., 2022; Wang et al., 2022). Souri et al. (2017) and Zhang et al.
67 (2016), for example, discussed the existence of decreases in NO_x emissions over developed
68 countries following emission regulations after the turn of the century. In the North Atlantic region,
69 both surface O₃ and CO have decreased; Kumar et al. (2013) showed this for 2001–2011. Such
70 decreases have been attributed to a decline in anthropogenic emissions from North America that
71 more than compensate for emission increases over parts of Asia. Furthermore, after the dramatic
72 reduction in global economic activity following the COronaVirus Disease 2019 pandemic,
73 significant reductions in northern hemisphere (NH) tropospheric ozone values were observed in
74 2020 and 2021, although the tropical decreases are much smaller (Ziemke et al., 2022; Steinbrecht
75 et al., 2021; Bouarar et al., 2021; Miyazaki et al., 2021).

76 Carbon monoxide is another important pollutant in the troposphere. Its primary tropospheric
77 sources are incomplete combustion (biomass burning emissions and pollution from industrial and
78 traffic-related emissions), and the oxidation of methane and other hydrocarbons (Logan et al.,
79 1981; Crutzen and Andreae, 1990; Khalil and Rasmussen, 1990); its main tropospheric loss
80 pathway is oxidation by the hydroxyl radical (OH). Lower tropospheric CO anomalies are
81 propagated upward by convection and general ascent to produce a tropical “CO tape recorder”
82 (Schoeberl et al., 2006), primarily as a result of biomass burning episodes near the equinoxes
83 (Duncan et al., 2003, 2007; Logan et al., 2008; Nassar et al., 2009; Livesey et al., 2013; Huang et
84 al., 2016). Further insights into the transport of CO pollution into the upper troposphere and lower
85 stratosphere (UTLS) have been provided by Park et al. (2013), who examined CO and other species
86 from the Atmospheric Chemistry Experiment Fourier Transform Spectrometer (ACE-FTS) and
87 MLS. In the tropics, the clear signature of semiannual maxima centered around April and October
88 were observed, primarily over Africa, Indonesia, and South America, with connections to biomass
89 burning and convection patterns. Park et al. (2021) examined CO pollution transport to the UTLS
90 during and long after the highly enhanced 2015 Indonesian fire season, using a combination of CO
91 satellite data and model simulations (with the CAM-chem model), which generally showed
92 underestimates of satellite-derived tropospheric and stratospheric CO. In terms of tropospheric CO

93 trends, Worden et al. (2013a) found significant CO column decreases for the 2000–2011 period at
94 a rate of -1.5 \%yr^{-1} over Europe, East Asia, and the United States; this work was based mainly on
95 data from the Measurements of Pollution in the Troposphere (MOPITT) and the Atmospheric
96 Infrared Sounder (AIRS) (see also Warner et al., 2013). Using MOPITT data, Laken and Sahbaz
97 (2014) obtained a significant global CO trend of -0.6 \%yr^{-1} from 2000–2012; they also pointed to
98 significant increasing trends over parts of Asia, South America, and Africa. Buchholz et al. (2021)
99 found a similar result using 2002–2018 gridded time series from MOPITT CO, AIRS, and other
100 satellite instruments; the global trend for this period was found to be $-0.5 \pm 0.3 \text{ \%yr}^{-1}$, with a slower
101 decreasing trend during 2010–2018. Hedelius et al. (2021) also discussed MOPITT-inferred
102 decreasing trends in column CO for 2002–2017 and pointed out that decreases in CO emissions,
103 obtained from the Emissions Database for Global Atmospheric Research (EDGAR) version 4.3.2,
104 do not always match column CO trends. Analyses of ground-based in situ surface CO data also
105 point to a slowdown in the rate of decrease of CO after 2010, in comparison to the 2001–2010
106 decade (Patel et al., 2024). There is also a north-south interhemispheric difference in the CO
107 abundances (and total columns), along with faster rates of decrease in the northern hemisphere.
108 Decreasing CO emissions from anthropogenic and biomass burning sources appear to be the main
109 cause of global tropospheric CO decreases (Jiang et al., 2017, Andela et al., 2017), while secondary
110 CO resulting from methane oxidation is increasing (Gaubert et al., 2017). Some steeper CO
111 decreases have been observed in local extra-tropical near-surface data (Li and Liu, 2011; He et al.,
112 2013; Yoon and Pozzer, 2014; Gratz et al., 2015), apparently because of tighter air quality
113 standards and reduced pollution from industrial and traffic-related emissions.

114 The upper troposphere is a complex region where production of NO_x by lightning (Schumann
115 and Huntrieser, 2007; Murray et al., 2014), aircraft NO_x emissions (Hoor et al., 2009; Brasseur et
116 al., 2016; Lee et al., 2021; Wang et al., 2022), and stratosphere-troposphere exchange (STE) (Sudo
117 et al., 2003; Collins et al., 2003; Hegglin and Shepherd, 2009; Hess and Zbinden, 2013; Neu et al.,
118 2014) can significantly impact ozone concentrations; STE plays a larger role in the extra-tropics
119 than in the tropics (Hsu and Prather, 2014). Upper tropospheric trend analyses of in situ CO data
120 from commercial aircraft participating in the In-service Aircraft for a Global Observing System
121 (IAGOS, see Petzold et al., 2015) measurements have indicated decreasing trends from 1995 to
122 2013 in northern midlatitude UT CO, with some larger (and statistically robust) trends as high as
123 -2 to -3 \% yr^{-1} over eastern Asia (Cohen et al., 2018). The UT ozone trends from the latter analyses

124 were found to range between 0.25 to 0.45 ppbv yr⁻¹; this reflects changes of order 0.4–0.8% yr⁻¹.
125 In terms of variability, there are interannual composition changes in the troposphere and in the
126 UTLS associated with ENSO (Chandra et al., 1998; Ziemke and Chandra, 2003; Nassar et al.,
127 2009; Oman et al., 2011, 2013) and related sea surface temperature and pressure changes. It has
128 long been known that this important mode of climate variability that originates in the Pacific
129 Ocean, with alternating warm (El Niño) and cold (La Niña) phases, leads to disruptions in global
130 circulation patterns, and has impacts on fire and wetland emissions that affect tropospheric
131 composition (Feely et al., 1987; Jones et al., 2001; Sudo and Takahashi, 2001; Duncan et al., 2003;
132 Doherty et al., 2006; Calvo et al., 2010; Voulgarakis et al., 2015; Rowlinson et al., 2019).

133 How do changes in the upper troposphere relate to changes in the lower troposphere, such as
134 changes in emissions? There have not been many such studies in the past, in large part because of
135 the lack of well-sampled long-term data in the upper reaches of the troposphere, where ozone is of
136 radiative significance. While this region is not directly connected to surface pollution, fast
137 convection episodes in the tropics imply that there might well be some correlations between lower
138 tropospheric and upper tropospheric abundances, and even for long-term trends. Long-range
139 transport of pollution can, however, extend into the UT, and also back downward with cross-
140 continental impacts on surface pollution levels. Constraints on chemistry climate models are one
141 important goal for studies of long-term measurements of upper tropospheric composition. Such
142 studies are also expected to contribute to continuing assessments of pollutant trends in the
143 troposphere, such as the Tropospheric Ozone Assessment Report Phase II (TOAR-II), while
144 related model simulations are of interest to continuing assessments of chemistry climate models
145 (e.g., CMIP-7).

146 Tropical upper tropospheric profiles of O₃ and CO have been measured on a continuous daily
147 basis by the Microwave Limb Sounder on the Aura satellite, from a near-polar sun synchronous
148 orbit since late 2004. Here, we present results of trends and variability analyses of these data sets
149 (from 2005–2020), along with a similar treatment of UT O₃ and CO time series from two chemistry
150 climate models, “specified dynamics” versions of the Whole Atmosphere Community Climate
151 Model version 6 (WACCM6) and the Community Atmosphere Model with chemistry (CAM-
152 chem), both of which are configurations of the Community Earth System Model version 2.2
153 (CESM2.2). When using regression fits, as done here, to analyze broad-scale atmospheric time
154 series, one should pay attention to likely drivers (e.g., ENSO) of variability in that region, since a

155 better fitting of such variability can reduce the resulting trend uncertainties. Altogether, we use
156 one WACCM simulation as well as two separate CAM-chem simulations (the latter two having
157 different anthropogenic emission inputs for CO), as described in Sect. 2, where we provide more
158 details about the MLS data and these model simulations. Section 3 focuses on the trend analysis
159 methodology. In Sect. 4, we discuss the analysis results for O₃, and then for CO; we review the
160 UT climatologies for these species and some differences versus model simulations, and discuss
161 results from zonal mean and mapped trend analyses. We also place our results in the context of
162 past analyses. We then finish with some brief conclusions in Section 5.

163 **2 Observations, model simulations, and trend analysis methods**

164 For both MLS and the chemistry climate models, we analyze monthly averaged zonal mean
165 time series as well as monthly-averaged longitude/latitude binned time series. The models have
166 been designed to capture key dynamical and chemical processes well enough to be usefully
167 compared to the observations. We focus on a region that is somewhat below the tropopause, to
168 minimize potential effects from stratosphere-troposphere exchange and to avoid results that might
169 depend more on lower stratospheric rather than tropospheric change.

170 **2.1 Observations**

171 The Aura MLS observational dataset considered here is taken from sixteen full years (2005
172 through 2020) of global composition measurements, with about 3500 vertical profiles per day per
173 measured species. The MLS antenna performs scans of the atmospheric limb ahead of the Aura
174 satellite in its near-polar sun-synchronous orbit. MLS measures daytime and nighttime thermal
175 emission using microwave radiometers operating at frequencies near 118, 190, 240, and 640 GHz;
176 a 2.5 THz module measured OH during the early part of the mission. The 240 GHz radiometer
177 provides the standard O₃ and CO measurements. For an overview of the MLS measurement
178 technique, the reader is referred to Waters et al. (2006). Read et al. (2006) gave a description of
179 the simulated MLS forward model and related spectra. The MLS retrievals (Livesey et al., 2006)
180 use the optimal estimation approach (Rodgers, 2000); there is no assumption of atmospheric
181 homogeneity along the line of sight (see Livesey and Read, 2000), and the retrievals make use of
182 the MLS antenna's views along overlapping tangent rays during consecutive scans of the Earth's

183 limb. The specifics of MLS data characterization and data quality, along with estimated errors and
184 related information can be found in the documentation by Livesey et al. (2022).

185 Here, we have used the latest data version from MLS, labeled version 5.0 or v5. More
186 specifically, we use the binned MLS Level 3 data sets, with a latitude grid that includes the
187 equatorial bin (-2° to $+2^{\circ}$) and the 44 other adjacent 4° -wide bins. In this work, we use monthly
188 mean time series based on zonal averages as well as latitude bands divided into 12 longitude bins.
189 The typical number of MLS profiles in a monthly zonal mean 4° bin is of order 2400, and about
190 200 for each of the 12 mapped (monthly) longitude/latitude bins. Prior to averaging the MLS data,
191 the standard MLS data quality screening criteria (Livesey et al., 2022) have been applied to all the
192 O_3 and CO Level 2 profiles; this screening removes only a very small fraction (typically 1–3%) of
193 the retrieved profiles. In the troposphere and stratosphere, the MLS O_3 retrieval grid is defined by
194 a subset of the pressure levels given by $p(n) = 1000 \times 10^{-n/12}$ hPa, where n is the pressure level index
195 number; for CO, the grid is twice as coarse, meaning that $n/6$ is used as an exponent in the above
196 equation, rather than $n/12$. The bottom recommended levels for the O_3 and CO retrievals are at 261
197 and 215 hPa, respectively. Our tropical analyses will focus on results between 215 and 147 hPa,
198 in order to largely obtain upper tropospheric results, as more influence from the stratosphere occurs
199 as one gets closer to 100 hPa in the tropics. In the upper troposphere, the vertical resolution of the
200 O_3 and CO products is about 3 km and 5 km respectively (Livesey et al., 2022). In this region, the
201 single-profile precision (1σ random uncertainty) is 20–30 ppbv (meaning ~ 35 -50%) for O_3 and
202 15–20 ppbv (~ 20 –30%) for CO. For our analyses of monthly MLS averages, the relevant precision
203 for O_3 and CO reduces to ~ 0.5 ppbv ($\sim 1\%$) for 4° zonal means and ~ 2 ppbv ($\sim 4\%$) for the gridded
204 data using 30° longitude by 4° latitude bins. In addition, the methodology used by the MLS team
205 to assess the aggregate effects of estimated errors in various input parameters, coupled with
206 validation results (see Livesey et al., 2022), leads to systematic uncertainty estimates (1σ) of 5–12
207 ppbv (~ 10 –20%) and 15–25 ppbv (~ 20 –35%) for tropical upper tropospheric O_3 and CO,
208 respectively.

209 Following validation work on UT MLS O_3 and CO in the early few years since the Aura launch
210 (Livesey et al., 2008), studies of UT MLS O_3 by Livesey et al. (2013) focused on seasonal and
211 interannual variability and comparisons versus ozonesonde data. Despite sampling differences
212 between these measurement systems, the temporal patterns evident in the MLS UT O_3 data were
213 found to be generally well correlated with the *in-situ* data over different low latitude regions.

214 Distinct seasonality was evident in O₃ and CO (as well as MLS-derived ice water content) over
215 South America and South Africa. Other patterns such as the “wave-one” pattern in tropical O₃ (see
216 Thompson et al., 2000, 2003, Wang et al., 2006) and double peaks in O₃ variability over eastern
217 equatorial Africa (with enhancements around May/June and September to November) were
218 discussed; for MLS UT CO, distinct seasonal behavior was found, for example, in the northern
219 hemisphere tropics, over Eastern Asia and across the Pacific (see also Huang et al., 2012). Livesey
220 et al. (2013) and Huang et al. (2014) discussed the connection between emissions from intense
221 fires over Indonesia in 2006 (following the El Niño-related drought) and dramatic concomitant
222 enhancements in UT CO (from MLS data) over this region. This work has been expanded upon in
223 analyses by Park et al. (2013, 2021) of the significant and long-lasting impacts of more recent El
224 Niño-related droughts and wildfires on tropospheric and lower stratospheric CO abundances.

225 Regarding MLS ozone, previous work has shown vertical oscillations in zonal mean MLS
226 UTLS O₃ profiles (e.g., see Livesey et al., 2022). There are also some biases in MLS tropical UT
227 ozone values, which tend to be on the high side (by 10–20%) with respect to ozonesonde data (see
228 Hubert et al., 2016, Fig. 6), but the above issues are systematic in nature. While we think that
229 neither these biases nor the small vertical oscillations (a few % in magnitude in the region of
230 interest here) would play a major role in changing our MLS UT trend results, given the trend
231 uncertainties (discussed later), any time-dependent effect, if it exists, would be quite difficult to
232 characterize, or provide a fix for.

233 We also compare the CO simulations to CO data from Terra/MOPITT, obtained from
234 multispectral retrievals (V9J) Level 3 dry air total column data, or X_{CO} in ppbv (Deeter et al.,
235 2022). The simulated CO values are smoothed by using the MOPITT a priori columns as well as
236 the 10 layers a priori and averaging kernel profiles, as recommended for a quantitative comparison
237 of modelled and MOPITT X_{CO}.

238 **2.2 Model simulations**

239 We use the Whole Atmosphere Community Climate Model version 6 (WACCM6) and the
240 Community Atmosphere Model with Chemistry (CAM-chem), both of which are components of
241 the CESM2.2 (Danabasoglu et al., 2020). WACCM6 uses the “high-top” set of 70 model levels
242 between the surface and the lower thermosphere (~140 km), while CAM-chem uses 32 layers
243 (“low-top”) that stop in the middle of the stratosphere (~40 km). Both configurations run on a

244 horizontal resolution that is 0.95° latitude \times 1.25° longitude and share the same vertical grid in the
245 troposphere, with a vertical resolution in the upper troposphere of about 1.2 km. Both CAM-chem
246 and WACCM6 include the same representations of boundary layer processes, shallow convection,
247 liquid cloud macrophysics, and cloud microphysics (Gettelman et al., 2019). Each model employs
248 the same chemical mechanism processes (labeled TS1). The chemical scheme includes the O_x ,
249 NO_x , HO_x , ClO_x , and BrO_x families, along with CH_4 and its degradation products, as well as
250 primary non-methane hydrocarbons and related oxygenated organic compounds (Emmons et al.,
251 2020). Reaction rates follow the JPL Publication 19-5 recommendation (Burkholder et al., 2019).
252 TS1 includes a total of 231 species and 583 chemical reactions broken down into 150 photolysis
253 reactions, 403 gas-phase reactions, 13 tropospheric, and 17 stratospheric heterogeneous reactions.
254 The photolytic reactions are based on both inline chemical modules and a lookup table approach
255 (Kinnison et al., 2007). Secondary organic aerosols are represented through the Volatility Basis
256 Set approach (Tilmes et al., 2019). Comparisons of oxidants during the Korea–United States Air
257 Quality (KORUS-AQ) experiment in South Korea led to a revision of the heterogeneous aerosol
258 uptake of hydroperoxyl radicals (HO_2) to produce H_2O instead of H_2O_2 and a reduction of the
259 coefficient (γ) from 0.2 to 0.1 (Gaubert et al., 2020).

260 To accurately represent weather conditions as well as the Quasi-Biennial Oscillation (QBO)
261 and to reproduce various modes of middle atmospheric variability, both simulations are run in the
262 ‘specified dynamics’ (SD) mode. The model dynamical constraints are taken from meteorological
263 fields provided by the Modern-Era Retrospective Analysis for Research and Applications version
264 2 or MERRA-2 (Gelaro et al., 2017). Contrary to the previous SD approach, the MERRA-2 fields,
265 here the zonal and meridional winds and temperature, are first regridded to the model horizontal
266 and vertical grids. The model nudging (Davis et al., 2022) is updated at every (30 min) time step
267 using the closest 3-hourly MERRA-2 fields; nudging timescales are set at 6 hours for the CAM-
268 chem simulations and at 12 hours for WACCM6. The 11-year solar cycle variability is taken from
269 the Naval Research Laboratory’s (NRL) solar model, namely the NRL Solar Spectral Irradiance
270 version 2 (NRLSSI2; Coddington et al., 2016). Volcanic SO_2 emissions (used in sulfate aerosol
271 density calculations) are derived for significant volcanic eruptions using the Neely and Schmidt
272 (2016) database updated through the year 2020. The model scenario used here is based on historical
273 forcings (and recent updates) from the Climate Model Intercomparison Project – Phase 6
274 (Meinshausen et al., 2017). The forcings include greenhouse gases (CH_4 , N_2O , and CO_2) and

275 organic halogens. After 2014, the greenhouse gas and organic halogen inputs follow the CMIP6
276 SSP5-8.5 scenario that projects inputs beyond 2014 (O'Neill et al., 2016; Riahi et al., 2017;
277 Meinshausen et al., 2020).

278 The emissions from CMIP6 were updated to CAMS-GLOB-ANT_v5.1 in the simulation we
279 refer to as CAM-chem-CAMS (CAMS is the Copernicus Atmosphere Monitoring Service) and
280 CAMS-GLOB-ANT_v5.3 in the WACCM simulation (labeled WACCM-CEDS) for all surface
281 anthropogenic emissions (Soulié et al., 2024). CO anthropogenic emissions were found to be too
282 low in South Asia and China (Gaubert et al., 2023), so these emissions were replaced by the
283 Community Emissions Data System (CEDS) v2, presented in McDuffie et al. (2020), for the CAM-
284 chem-CEDS simulation also analyzed here, and for the only WACCM simulation used here. We
285 can thus exclude a change in CO secondary formation or sink between these two simulations.
286 Daily biomass burning emissions are obtained from the Quick-Fire Emissions Dataset (QFED) 2.5
287 (Darmenov and da Silva, 2014) in all three simulations.

288 The lightning NO_x production and its role in ozone formation is reviewed by Verma et al.
289 (2021). This study showed that most lightning activity occurs within deep convective clouds in the
290 tropical and subtropical region. In our study, the emission of NO from lightning is based on the
291 Price parametrization (Price and Rind, 1992; Price et al., 1997). This parameterization
292 is dependent on cloud height, which includes a stronger dependence over land versus ocean
293 (Emmons et al., 2010). The CAM-Chem and WACCM models used here derive tropical (and
294 global) lightning NO_x values of 2.34 (3.23) and 2.78 (4.11) Tg (N) yr⁻¹, respectively (Table 1),
295 with no significant trends over the course of these simulations. These global values are within the
296 generally accepted global range of 3–8 TgN yr⁻¹ for lightning NO emission (Schumann
297 and Huntrieser, 2007).

298 Aircraft emissions from CMIP6 were employed in WACCM6. Both CAM-chem simulations
299 use the version 2.1 of CAMS-GLOB-AIR for aircraft emissions described by Soulié et al. (2024).
300 Gaubert et al. (2020, 2023) found that this version of CAM-chem tends to overestimate
301 tropospheric oxidants, such as ozone, hydrogen peroxide, nitric acid, and hydroxyl radical,
302 resulting in a shorter lifetime of tropospheric methane and CO, mainly in the northern hemisphere
303 extra-tropics. Some of the main model characteristics (with a focus on the differences) are
304 summarized in Table 1.

305 In terms of the model run analyses, we follow the same basic approach as for the MLS data.
306 The daily model profiles are first interpolated (as a function of $\log(\text{pressure})$) onto the MLS
307 pressure grid and then binned and averaged to produce the monthly zonal means (on a 4° latitude
308 grid) and gridded data on the same latitude/longitude grid as is described in Sect. 2.1 for MLS. We
309 note also that we do not find much impact on the MLS versus model comparisons if we use a
310 vertically smoothed version of the model profiles, which more properly takes into account the
311 vertical resolution of the MLS observations, as the differences between smoothed and unsmoothed
312 zonal mean values are much smaller than the model biases. For general simplicity, and for the
313 above reasons, we use unsmoothed model values in this work. A more detailed example of
314 smoothed model profile analyses is provided further below, in connection with observed seasonal
315 CO differences between the models and the MLS measurements.

316 **2.3 Trend analysis methods**

317 For both MLS and model time series trend analyses in the upper troposphere, we use the
318 multivariate linear regression (MLR) method discussed as part of similar studies performed by
319 Froidevaux et al. (2019) for the stratosphere. We refer the reader to Appendix (A3) of the above
320 reference for more details on the regression fit model, which includes commonly used functional
321 terms, namely a linear trend, and cosine and sine functions with annual and semi-annual
322 periodicities, to account for these known variabilities in atmospheric composition, with 3- and 4-
323 month periodic components to better fit shorter-term (intra-seasonal) variations, which also helps
324 to reduce the trend error bars. In addition, we include functions describing multi-year variations
325 caused by the QBO (which mostly affects the stratosphere) and by ENSO, which has been tied, for
326 example, to regional droughts and biomass burning events, with related increases in convection
327 and transport of surface pollution into the upper troposphere. The QBO-related equatorial wind
328 dataset is obtained from the publicly available datasets at the Free University of Berlin. ENSO-
329 related data are in the form of a multivariate index, following the initial work of Wolter and Timlin
330 (2011), as updated by Zhang et al. (2019). We have also included a fitted component that follows
331 variations in solar radio flux (at 10.7 cm), based on Canadian solar measurements (Tapping, 2013);
332 this component typically plays a negligible role in our results. For trend uncertainty estimates, as
333 discussed also by Froidevaux et al. (2019, 2022), we use the block bootstrap resampling method
334 (Efron and Tibshirani, 1993), as done by Bourassa et al. (2014) and others in such atmospheric

335 composition analyses. For every fitted time series, we analyze thousands of re-samplings of the fit
336 residuals, with year-long blocks of residual values replaced by residual series from randomly
337 chosen years; twice the standard deviations in these random distributions' trends provide the (2σ)
338 trend uncertainty values that we use as trend error bars throughout this work.

339 **3 Results**

340 **3.1 Tropical UT O₃**

341 **3.1.1 O₃ climatologies**

342 Although this work focuses on variability and underlying trends, we start in Fig. 1 by showing
343 annually-averaged climatological ozone comparisons between MLS, the WACCM-CEDS
344 simulation, and the CAM-chem-CEDS simulation for 2005–2020 at 147 and 215 hPa for low
345 latitudes (4-degree bin centers between 24°S and 24°N); mapped fields and zonal mean line plots
346 are compared in this Figure. At 215 hPa near 20°N and 20°S, the zonal mean O₃ values from both
347 models are ~5–15% lower than the MLS fields; differences of this order are also observed in the
348 mapped fields. The differences reach about -20% in the deep tropics, as the MLS latitudinal
349 gradients are flat in this region, in contrast to the models' more curved behavior, with a minimum
350 at the equator (see panel (k)). The differences observed here are within the MLS systematic
351 uncertainties mentioned in Sect. 2.1 (up to 24 ppbv, 2σ). These two models agree quite well in the
352 UT region as a whole (typically within about 5 ppbv); such a good level of agreement is not too
353 surprising, given that these models are based on a very similar framework, with nearly identical
354 inputs (see Sect. 2.2). At smaller pressures (147 hPa and also for 100 hPa, which is not shown
355 here), the models follow the MLS latitudinal gradients better (see panel (d) for the comparison at
356 147 hPa), as well as the longitudinal features (including the well-known wave-one ozone pattern
357 discussed by Thompson et al., 2000, 2003, Wang et al., 2006, and others). However, the models
358 exhibit a positive average bias versus MLS at these two pressure levels (see panel (e), where the
359 model bias for 147 hPa is about +20%). However, MLS UT O₃ profiles have been found to be
360 biased positively (by about 10–20%) versus averaged tropical ozonesonde profiles (Sect. 2.1).
361 Thus, positive model biases versus MLS ozone in the tropical UT are not likely caused by a
362 significant underestimate by MLS. We note that the positive model biases (at 147 and 100 hPa)

363 occur for all months of the year (not shown here), so this is not caused by a very large bias in some
364 months, that could be partially compensated for by negative model biases in other months.

365 As mentioned previously, we focus on the upper tropospheric region, somewhat removed from
366 the tropopause, with 147 to 215 hPa being the main levels of interest in the analyses below; while
367 the UT average differences between model and MLS are worth noting, this is not a primary concern
368 in terms of the trend comparisons that we focus on here.

369 **3.1.2 O₃ zonal mean trends**

370 Figure S1 gives some time series examples for ozone at 12°N and 12°S at 147 and 215 hPa,
371 with the MLS and modeled (WACCM-CEDS) series and their respective regression fits, along
372 with the fitted trend lines. The linear correlation coefficients listed above each panel provide a
373 measure of how well the chemistry climate model can fit the MLS series variability. The UT O₃
374 WACCM-CEDS trends roughly follow the trends that are obtained from the MLS regression fits.

375 Regarding the ozone trends, we now switch to results from our analyses of the monthly zonal
376 mean MLS and model time series. Figure 2 displays ozone trend results for MLS and the three
377 simulations for 147, 178, and 215 hPa, based on a multiple linear regression analysis of the
378 respective time series from 2005 through 2020. Figure 2 shows that the tropical upper tropospheric
379 MLS ozone trends are generally positive and significant (meaning that a zero trend lies outside the
380 2σ estimate of trend uncertainty). The observed average ozone trends at all three pressure levels
381 lie within about 0.3 to 0.5 % yr⁻¹; the peak average trends occur at 178 hPa. There are fairly small
382 latitudinal differences at 178 and 215 hPa. At 147 hPa, the MLS results indicate ~50% larger trends
383 in the NH tropics than in the SH tropics, although this difference is not very significant. The zonal
384 mean MLS ozone trend (averaging the three pressure levels at 147, 178, and 215 hPa) for 2005–
385 2020 in the 20°S–20°N UT region is 0.39 ± 0.28 %yr⁻¹. The error bars here indicate the 2σ trend
386 uncertainty (calculated here as the root mean square of the 2σ trend uncertainties at all three
387 pressure levels in Fig. 2). This tropical UT O₃ trend is equivalent to 0.21 ± 0.15 ppbv yr⁻¹ (based
388 on the annual average tropical UT values of 56 ppbv measured by MLS). The corresponding model
389 O₃ zonal mean trend results obtained here for 2005–2020 have a positive trend, with excellent
390 agreement with MLS from CAM-chem-CEDS (0.38 ± 0.28 %yr⁻¹). This agreement is also apparent
391 in the latitudinal pattern, with larger trends in the NH than in the SH, even if the error bars are
392 large enough that there is no “statistically significant difference” between the hemispheres. There

393 is also good statistical agreement between the MLS zonal mean ozone trends and the slightly
394 smaller WACCM-CEDS trends ($0.21 \pm 0.23 \text{ \%yr}^{-1}$). We note that statisticians have been working
395 to guide or adjust “common practices” regarding statements of “significance”, and one should be
396 sensitive to some of the broad differences that occur even within the so-called formal criteria (such
397 as 2σ or a p-level of 0.05), which could sometimes be interpreted in too stringent a way
398 (Wasserstein et al., 2019), and as pointed out by Y. Cohen (private communication, 2024). We
399 keep this in mind in some of our discussions here, but we also wish to comment specifically on
400 the use of broader latitude bins. Indeed, if broader latitude regions were analyzed for trends, the
401 corresponding trend uncertainties would be reduced, which could make some of the compared
402 trends differ by more than their 2σ error bar variability. However, the trend error reduction in our
403 testing with a 20° -wide latitude bin instead of a 4° bin is only 5–10%, meaning that the
404 uncertainties get divided by much less than the square root of the number of small latitude bins
405 used (an error reduction result corresponding to zero correlation in the temporal variability
406 between bins, e.g., if random noise alone was present). Thus, we do not readily obtain more
407 significant differences in these comparisons by just averaging over broader regions. In Figure 3,
408 the MLS and CAM-chem-CEDS UT O₃ trend sensitivity analysis is repeated for 2005–2018,
409 2005–2019, 2006–2020, and 2007–2020, showing the relative insensitivity of the MLS results to
410 the choice of time period. This is also true for the CAM-chem-CEDS trends in the NH tropics,
411 although there is more ozone trend sensitivity to the time period choice in this model’s results over
412 the SH tropics. The WACCM-CEDS tropical UT ozone trend results versus time period (not shown
413 here) lead to a spread in the SH tropical trends that is about halfway between the small MLS trend
414 spread and the larger CAM-chem-CEDS trend sensitivity shown in Fig. 3.

415 **3.1.3 O₃ mapped trends and variability**

416 We now turn to the mapped tropical UT trends by analyzing subsets of the O₃ and CO fields
417 from MLS and the models, based on monthly mean time series for 2005–2020 in latitude/longitude
418 bins, rather than on zonal means. As mentioned previously, these bins are also 4° wide in latitude,
419 and the longitude bins are 30° wide. The same regression methodology as described previously
420 here is used for each of the binned time series; we focus on the WACCM-CEDS and CAM-chem-
421 CEDS ozone trends, as we have found that the CAM-chem-CAMS and CAM-chem-CEDS results
422 are quite similar, in the case of ozone at least. Figure 4 shows the resulting mapped O₃ trends from

423 MLS and the two models for 147 and 215 hPa (top and bottom rows, respectively), with the maps
424 spanning 26°S to 26°N. Hatched bins indicate trends for which the 2σ uncertainty range
425 encompasses the zero trend value which is often interpreted as a low level of “statistical
426 significance”, although one should be cautious (see the previous Section) regarding the strict
427 application of such a criterion or wording. The largest MLS trends are observed over the
428 Indonesian region and (mostly) to the East of that region, as well as over the northern Atlantic.
429 The mapped trends confirm the overall zonal mean result of slightly larger O₃ trends in MLS than
430 in WACCM-CEDS. Broad regions with positive tendencies are observed in both model trend
431 results; these regions include SouthEast Asia, Indonesia, northern Australia, the Atlantic, and
432 northern Africa, with some, but not exact agreement with the regions mentioned above for the
433 larger MLS trends. At 215 hPa, the slightly larger positive trends in CAM-chem-CEDS than in
434 WACCM-CEDS over the Australian region (bottom right quadrant, south of the equator)
435 contribute to the better correspondence between the zonal mean O₃ trend results (Fig. 2c) between
436 CAM-chem-CEDS and MLS over the southern tropics. The mapped trend discrepancies between
437 the simulations and MLS are rarely outside the 2σ error bar ranges. Nevertheless, some of the
438 discrepancies are worth noting, especially when they cover multiple adjacent bins; in particular,
439 the easternmost longitude band shows MLS trends with (significant) positive values, in contrast to
440 the simulation results, with binned trends that are often small and/or negative.

441 We have compared these mapped ozone trend results to those for tropospheric column ozone
442 (TCO) obtained by Ziemke et al. (2019), using a combination of total O₃ columns from the Aura
443 Ozone Monitoring Instrument (OMI) and MLS-based stratospheric O₃ columns. In Fig. 5, we show
444 in the top two rows the trends from MLS ozone at 178 hPa (top map) versus the bottom map which
445 provides the mapped TCO trends for the same time period, obtained from an appropriate horizontal
446 smoothing of the results obtained following the above reference, to make the MLS and TCO
447 resolutions comparable; this smoothing comes from an interpolation versus latitude and a weighted
448 averaging in longitude, since the TCO results have finer longitudinal resolution (5°-wide bins) than
449 the MLS longitudinal grid used here (30°-wide bins). Similarities are observed in the longitudinal
450 pattern of UT O₃ and TCO trends, as shown also for 3 different latitude bins in panel (c) of Fig. 5;
451 variations of a factor of two to three are observed, mostly in the northern half, between the western
452 and eastern hemispheres for both sets of trends, which tend to lie between roughly 0.3 and
453 1.2 % yr⁻¹. However, the agreement between MLS UT O₃ and TCO trends is often worse for other

454 MLS pressure level choices; this can be deduced from panel (d), where R (correlation coefficient)
455 values relating to the longitudinal variations obtained from MLS at different pressures versus the
456 longitudinal variations in TCO are displayed as a function of latitude (y-axis). In fact, one might
457 not expect the MLS ozone UT trends to track the TCO trends very well, given that TCO measures
458 the entire column whereas MLS measures trends in a vertical region about 5 km wide in the upper
459 troposphere, but this was worth looking into. Regional variability and horizontal sampling
460 differences between MLS and OMI will also play a role (see Thompson et al., 2021, for variability
461 aspects of sonde-derived tropospheric trends). Our comparisons imply that the correlation between
462 lower and upper tropospheric ozone trends is not a strict “one-to-one mapping”, but there are
463 nevertheless some similarities between these regions.

464 We have also analyzed the level of explained variance in the regression fits for these binned
465 trend results. Figure 6 shows the square of the correlation coefficient values (R^2) as a function of
466 latitude and longitude for different explanatory variables used in the binned O_3 fits at 147 hPa,
467 based on fit comparisons to the MLS series (top 6 panels), and for the regression fit versus the
468 WACCM-CEDS series (bottom 6 panels). We have ignored the solar component in these plots as
469 it was found to be of negligible importance; we display the remaining contributions, namely the
470 annual, semi-annual, short-term (sum of the 3-month and 4-month terms), QBO, and ENSO terms,
471 as well as the contribution from the full regression fit, which shows that most (but certainly not
472 all) of the time series variance can be explained by such a regression model. The annual term and
473 semi-annual terms can generally explain a large part of the variance, usually followed in
474 importance by the ENSO term, over most of the Pacific. The QBO component is very small in the
475 upper troposphere, even though it is a well-known and large contributor to stratospheric trace gas
476 variability in the lowermost stratosphere. There is also a significant annual cycle in the tropical
477 lowermost stratosphere related to variations in vertical velocities and in the Brewer-Dobson
478 circulation (Randel et al., 2007; Witte et al., 2008). The R^2 patterns observed in the MLS panels
479 are reproduced in a broad sense by the fits to the CCM, as shown in the bottom 6 panels; this is
480 also a result of the close match between the CCM and the MLS O_3 time series, shown earlier in
481 this work. The ENSO model pattern for O_3 does not match the MLS-derived pattern that well over
482 Indonesia, but this comparison is generally better in the Pacific region between -90° and -180° . A
483 somewhat weaker R^2 value in the model simulation also exists in parts of the Eastern hemisphere
484 for the semi-annual term. The combination of these differences helps to explain the somewhat

485 poorer overall fits (and variance contributions) for the model than for MLS. For the most part, it
486 does not matter much which model run is used for these analyses, or even which pressure level is
487 used; indeed, the results at 215 hPa (see Fig. S5) are generally similar to those in Fig. 6.

488 To pursue the ENSO-related patterns further, one can obtain a (mapped) sensitivity coefficient
489 to ENSO from the regression fits regarding this component's importance in ppbv/K (where "K"
490 relates to tropical sea surface temperatures changes). The O₃ ENSO sensitivity is shown in Fig. 7
491 for the 2005–2020 MLS and WACCM-CEDS results at 147 and 215 hPa. This provides more
492 information about the sign of the sensitivity over different regions, and we observe generally
493 positive (negative) sensitivity in the Eastern (Western) hemisphere, for both MLS and WACCM-
494 CEDS cases; moreover, at least at 147 hPa, there are two strong negative minima on each side of
495 the Equator in the central Pacific region. The model results are quite consistent with those from
496 MLS in terms of the ENSO-related sensitivity coefficient patterns and magnitudes, although the
497 model response is often slightly smaller than seen in the MLS result. As we discuss further below,
498 such ozone sensitivity patterns have been described and interpreted before. Figure 16 provides the
499 same analysis, but for the CO sensitivity to ENSO. These maps show a positive CO ENSO
500 sensitivity coefficient throughout the tropics, with local maxima in both the Eastern and Western
501 hemispheres, rather than the O₃ dipole (positive/negative) structure shown in Fig. 7. The model
502 CO ENSO sensitivity broadly matches the MLS results, although it is not as strong; the different
503 patterns in the western hemisphere, compared to the O₃ sensitivity to ENSO, might be caused by
504 differences in O₃ and CO vertical profile gradients in these regions, but this would require further
505 detailed investigations. We also note that, especially in the MLS case, the peak magnitudes of the
506 CO ENSO sensitivity coefficients in Fig. 16 match the peak magnitudes of the positive O₃ ENSO
507 sensitivity in Fig. 7.

508 **3.1.4 O₃ discussion**

511 We have found some climatological differences between the MLS observations of O₃ and CO
512 in the tropical upper troposphere and the WACCM-CEDS simulation, as well as both CAM-chem
513 simulations considered here. For O₃, the models underestimate the mean MLS values at 215 hPa;
514 at 147 hPa, the models are biased high by about 15–25%, and we have no reason to believe that
515 such positive biases result from an average negative bias in the corresponding MLS values.

516 The averaged zonal mean tropical UT O₃ trend from MLS for 2005–2020 is $0.39 \pm 0.28 \text{ \%yr}^{-1}$
517 (or about $0.22 \pm 0.16 \text{ ppbv yr}^{-1}$), where the error bars indicate 2σ uncertainties. We should note
518 that the MLS ozone profile trend detection capability lies within the most stable among ozone
519 sounders, based on the satellite and ground-based ozone intercomparison work by Hubert et al.
520 (2016). In addition, differences between stratospheric ozone columns from MLS and the Aura
521 Ozone Monitoring Instrument (OMI) exhibit no significant drift (Ziemke et al., 2019), thus
522 providing added confidence in the temporal stability of both measurement systems; also, we expect
523 a similar level of confidence in the stability of the MLS CO measurements, since CO is retrieved
524 using the same radiometer as the MLS standard ozone product. We obtain excellent agreement
525 with the MLS tropical UT zonal mean trends from the (averaged) CAM-chem-CEDS O₃ zonal
526 mean trends ($0.38 \pm 0.28 \text{ \%yr}^{-1}$) and somewhat poorer agreement from the smaller WACCM-
527 CEDS trends ($0.21 \pm 0.23 \text{ \%yr}^{-1}$). We also show that the zonal mean MLS O₃ tropical UT trend
528 results for different time period choices, with start and end years adjusted by one or two years, do
529 not significantly depart from the 2005–2020 results; there is more sensitivity to the choice of time
530 period in the CAM-chem-CEDS trend results over the southern tropics.

531 In terms of mapped ozone trends, the largest MLS-derived tropical trends (up to $+1.4\% \text{ yr}^{-1}$) are
532 observed over Indonesia and East of that region, as well as over the northern Atlantic region. The
533 mapped model O₃ UT trends broadly match the MLS trends, albeit with somewhat smaller
534 variations. The significant model maxima over Southeast Asia and the North Atlantic are similar
535 to the significant MLS patterns in those regions. More qualitatively, the Indonesian region displays
536 smaller model O₃ trends than those derived from MLS data; parts of the western Pacific region
537 exhibit some negative trends in the MLS and model trends, but not with good spatial correlation.
538 The mapped MLS-based UT O₃ trends and TCO trends for the same period (see Fig. 5), based on
539 the analyses of Ziemke et al. (2019), provide good correlations in parts of the tropics, with similar
540 values and longitudinal patterns; however, the MLS UT O₃ trend maxima over the western Pacific
541 are symmetric about the equator, whereas the TCO maxima in that region are found in the northern
542 part only. Since the TCO measurement weighting does not favor the UT region, we would not
543 necessarily expect a really high correlation versus the MLS UT trends. **A recent study (Gaudel et**
544 **al., 2024) of tropical tropospheric ozone trends from several satellite-based and in situ datasets**
545 **between 1994 and 2019 yields “maximum mid- and upper tropospheric increases above India,**
546 **Southeast Asia and Malaysia, with values from 3.4 ± 0.8 to $6.8 \pm 1.8 \text{ ppbv decade}^{-1}$.” The tropical**

547 UT O₃ trend results obtained here from MLS data, translated to the same units, are 2.2 ± 1.6 ppbv
548 decade⁻¹, which is consistent with the above results, considering also that the maximum mapped
549 UT trend values obtained here (about 1.4 %yr⁻¹) translate to about 8 ppbv decade⁻¹. The MLS-
550 derived results for zonal mean tropical UT trends versus latitude are tabulated in Table S1 in both
551 sets of units. The OMI/MLS tropical trends (2004–2021) from the above reference are listed as 2
552 ± 5 % decade⁻¹ for 0 to 20°S and 3 ± 2 % decade⁻¹ for 0 to 20°N; these numbers are consistent with
553 the slightly larger UT averages from MLS, which show an increase from ~3 % decade⁻¹ near 20°S
554 to ~4 % decade⁻¹ near 20°N (see Table S1 for more details).

555 **Regarding other past results,** the analyses by Wang et al. (2022) of the IAGOS commercial
556 aircraft database for several regions of the globe indicate that upper tropospheric O₃ values have
557 increased from 1995–2017, with some of the larger trends residing in the tropics. IAGOS-derived
558 trends were previously discussed by Cohen et al. (2018) for the 1994–2013 period, but with an
559 emphasis on the extra-tropics. The IAGOS trend analysis by Gaudel et al. (2020) for 5 tropical
560 regions over 1994–2016 gave positive UT trends in the range 0.3–1.3 % yr⁻¹, with an average of
561 0.5 % yr⁻¹, and largest values over Southeast Asia and Malaysia/Indonesia. As mentioned above,
562 the MLS results also show peak ozone trends over this general region. The above average trend
563 agrees quite well with the average tropical UT O₃ trends (0.39 ± 0.28 %yr⁻¹) we obtain from MLS,
564 which provides more uniform (and daily) tropical coverage. This seems to be unexpectedly good
565 agreement, since there are different sampling characteristics, regions, and time periods for IAGOS
566 versus MLS; given the time period differences, in particular, we should only consider this to be a
567 loose comparison. More detailed comparisons between MLS and IAGOS are difficult and beyond
568 the scope of this work, given the differences in coverage (and in the vertical and horizontal
569 footprints) between these measurement systems.

570 There have been large differences between past satellite-based tropospheric O₃ trends (Gaudel
571 et al., 2018). Leventidou et al. (2018) pointed out that tropical tropospheric ozone column trends
572 derived from a combination of European satellite measurements from 1996 to 2015 showed
573 regional increases as large as 1–2%yr⁻¹, with some negative trends over the oceans, but with
574 significant uncertainties as well (see also Heue et al., 2016, and Ebojie et al., 2016). The TCO
575 analyses by Ziemke et al. (2019) using combined OMI and MLS ozone columns showed that the
576 TCO trends are larger in the 2005–2016 time period than in the two decades before 2005; for the
577 2005–2016 period, the derived TCO trends in the tropics are about 0.4–0.7 % yr⁻¹ (see also Gaudel

578 et al., 2020). These two investigations found regional differences in the TCO trends, with maxima
579 over India, Southeast Asia, the eastern Pacific region, and the tropical Atlantic, while they obtained
580 near zero or slightly negative TCO trends over the Western Pacific. Similar TCO trends (based on
581 combined OMI and MLS data) were also given by Liu et al. (2022) for the 2005–2018 period.

582 Wang et al. (2022) showed that derived ozone trends from ozonesonde profiles agree broadly
583 with the IAGOS results, although the sonde spatio-temporal coverage is naturally more limited,
584 and there can be a fair amount of scatter in the trends between different sonde sites. Thompson et
585 al. (2021) observed significant seasonal variations in derived tropical ozonesonde trends (based on
586 data over the 1998-2019 period from the Southern Hemisphere Additional Ozonesondes, or
587 SHADOZ network); these authors noted that dynamical influences (besides emissions changes)
588 likely play a role in these tropical tropospheric trends, which average $0.1\text{--}0.4\ \text{\%yr}^{-1}$, but with trends
589 in certain regions/seasons (February to May in particular) as large as $1\text{--}2.5\ \text{\%yr}^{-1}$.

590 Zhang et al. (2016) and Wang et al. (2022) have ascribed the positive sign of post-2000 tropical
591 ozone trends to an equatorward redistribution of surface emissions over the years. Moreover, Wang
592 et al. (2022) discussed how increases in aircraft emissions of nitrogen oxides should also have
593 contributed to enhancements in UT ozone. The UT zonal mean model O_3 trends shown in our work
594 are typically larger (by $\sim 30\text{--}50\%$) in the NH tropics than in the SH tropics. This is also true for the
595 model simulation (also from CESM2) provided by Wang et al. (2022); these authors also point out
596 that uncertainties in estimates of ozone precursor emission inventories (including those for volatile
597 organic carbons species, or VOCs) may well contribute to differences between modeled and
598 observational ozone trends. While VOC source strengths might be difficult to invoke as a major
599 source of uncertainty for the tropical regions, other potential model issues (e.g., larger than
600 currently expected uncertainties in lightning-generated ozone in the tropical upper troposphere)
601 may be worth further consideration. We note that there are large differences (a range of a factor of
602 two or more) between the tropospheric ozone burden changes predicted by various global models
603 in the work by Wang et al. (2022). Also, Liu et al. (2022) show that significant regional differences
604 in ozone column trends exist in their model results (using the NASA Goddard Earth Observing
605 System Chemistry Climate Model, GEOSCCM), with near zero trends over the tropical western
606 Pacific; their modeled TCO trend results underestimate the observed positive TCO trends.

607 **Regarding ozone UT variability, we** found that the annual, semi-annual, and ENSO terms
608 dominate the variability in the tropical upper troposphere. The TCO interannual variability has

609 been known to be heavily influenced by ENSO (Ziemke and Chandra, 2003; Ziemke et al., 2010).
610 Oman et al. (2013) found that the ENSO relationship for ozone could be simulated by a chemical
611 climate model driven by observed SSTs. The observed and matching simulated sensitivity
612 coefficients imply increased downwelling from the stratosphere and suppressed convection during
613 El Niño periods for regions of positive sensitivity (Chandra et al., 1998; Sudo and Takahashi,
614 2001; Oman et al., 2013). The MLS UT ozone variations and their relation to ENSO were
615 discussed by Oman et al. (2013), who showed patterns of ozone sensitivity to ENSO at 147 hPa
616 (their Figure 6) that resemble the ones we produced here (in Fig. 7) from analyses of MLS data
617 over almost twice as long a period.

618 **3.2 Tropical UT CO**

619 **3.2.1 CO climatologies**

620 For CO, a similar set of annual mean climatological plots as those from Fig. 1 is provided in
621 Fig. 8. We observe that the model CO values follow the patterns of the MLS UT CO fields fairly
622 well, and the zonal mean model biases are usually around -10% to -20%; the model biases are
623 most often negative, and more so in the northern tropics at 215 hPa. The model mean CO biases
624 shown in Fig. 8 are well within the MLS CO systematic uncertainties mentioned in Sect. 2.1; the
625 CAM-chem-CEDS climatological UT CO is slightly closer to the MLS UT CO climatology than
626 is the WACCM-CEDS CO climatology. As in the case of ozone, the aforementioned model versus
627 data CO biases are found to exist not only for annual averages, but also on a month-to-month basis.
628 The SPARC Data Initiative report (SPARC, 2017) and the more recent update by Hegglin et al.
629 (2021) showed that MLS CO values in the tropical UT are within about 10–15% of the mean values
630 that include other data from ACE-FTS and the Michelson Interferometer for Passive Atmospheric
631 Sounding (MIPAS). However, the MLS mean values are larger than the multi-instrument mean at
632 100 hPa by about 10–20%, which can account for more than half of the MLS/model bias at this
633 level (not shown here). Also, just considering the theoretical systematic uncertainty estimates
634 provided in Sect. 2.1, it is possible that most (or even all) of the bias between models and MLS at
635 100 hPa is caused by a positive bias in the MLS CO data. However, an earlier WACCM-CEDS
636 version (WACCM4) underestimated CO and other hydrocarbon data in the southern tropical UT,
637 as described by Park et al. (2013); those authors noted that model deficiencies in emission source
638 strengths or in the upward rate of transport could potentially explain these model underestimates.

639

640 **3.2.2 CO zonal mean trends**

641 For CO, the zonal mean time series provided in Fig. S2 show that there are some slight
642 differences in the trends between observed and modeled (WACCM-CEDS) CO, with more
643 negative trends in the MLS series than in the model series. The large variability seen in the MLS
644 CO series shows correlation with WACCM-CEDS (see the large correlation coefficient values, R ,
645 in the 12°S series for 147 and 215 hPa). We know that the largest CO peaks in these time series
646 are tied to surface emissions, convection, and subsequent transport into the upper troposphere and
647 lower stratosphere (UTLS), with a strong connection to El Niño-related droughts and intense fire
648 (biomass burning) events (see, e.g., Schoeberl et al., 2006, Jiang et al., 2007, Liu et al., 2013, Park
649 et al., 2021, Duncan et al., 2003, 2007). At 12°N, however, the observed CO variability is
650 somewhat smaller than at 12°S, and the model variability is much more muted, while the model
651 versus MLS phasing agreement is quite poor, especially at 215 hPa (where R is very small and the
652 MLS time series annual phase is very poorly matched by the model). We have checked that this
653 poor correlation is not tied to an issue involving the smoothing of model profiles to account for
654 the MLS averaging kernels; indeed, Fig. S3 shows the small relative impact resulting from a
655 smoothed (versus vertically interpolated) model series on the average CO profile at 215 hPa and
656 12°N, as well as regarding the smoothed time series and its phasing.

657 For the UT CO zonal mean trends, Figure 9 provides results in a similar way to Fig. 2 for ozone,
658 but for just the two MLS CO retrieval levels at 147 and 215 hPa. In contrast to ozone, we can see
659 that the MLS-derived tropical UT CO values have typically decreased from 2005 to 2020; these
660 CO trends display negligible latitude dependence. Using the same approach as for ozone, but based
661 on the Fig. 9 results, we obtain an average MLS-based UT CO trend of $-0.25 \pm 0.30 \text{ \%yr}^{-1}$
662 (equivalent to $-0.20 \pm 0.23 \text{ ppbv yr}^{-1}$). The trends at 215 hPa (-0.16 \%yr^{-1}) are a factor of two
663 smaller than those at 147 hPa (-0.34 \%yr^{-1}), although both of these numbers agree within the (2σ)
664 trend uncertainties of 0.3 \%yr^{-1} ; based on the error bars, the CO trend from MLS at 147 hPa is
665 different from zero, while the corresponding MLS trend at 215 hPa is not. In contrast, the average
666 CAM-chem-CAMS UT CO trend at these levels is $0.22 \pm 0.19 \text{ \% yr}^{-1}$, with little difference
667 between 147 and 215 hPa. The two simulations that use CEDS emissions (WACCM-CEDS and
668 CAM-chem-CEDS) yield smaller trends for CO, namely $0.0 \pm 0.14 \text{ \%yr}^{-1}$, with slightly negative
669 average trends at 147 hPa and slightly positive average trends at 215 hPa. This difference in trends

670 can be explained by significant decreases in Chinese anthropogenic emissions in CEDSV2, despite
671 the increasing anthropogenic tropical CO emissions in both CAMS-GLOB-ANTv5.1 and CEDSV2
672 (see Fig. S4).

673 Furthermore, larger MLS CO abundances in 2020 explain why the MLS CO UT trends are
674 more negative if one stops the analyses in 2018 or 2019, as can be seen from Fig. 10, which is
675 analogous to the ozone trend sensitivity study provided in Fig. 3. Regarding another aspect of CO
676 trend sensitivities, we considered the issue of large peaks in the observed MLS CO time series (see
677 examples in Fig. S2) typically resulting from El Niño related biomass burning events, followed by
678 convective uplift and CO advective transport into the UTLS. If the model has smaller peaks than
679 the MLS data show, it may be that this could explain some differences, or even a change of sign
680 in the trends. This would stand out more if the large peaks occurred close to the beginning or end
681 of the time series. As a sensitivity test, we artificially suppressed the peaks in these series by setting
682 any CO value larger than 2.5 times the (1σ) variability to a value of 1.5 times this variability, and
683 we found the impact on the linear trends to be negligible (well within the error bars shown here).
684 Such a sensitivity study gives added confidence in the robustness of these trends.

685 In Fig. 11, we show the MLS, WACCM-CEDS, and CAM-chem-CEDS climatological mean
686 CO changes over the annual cycle at 215 hPa for 12°N and 12°S, along with the range of variability
687 (twice the standard deviations about the means). The fits from the models to the MLS CO behavior
688 at 12°S are quite good. The MLS CO curves show the two maxima previously observed in seasonal
689 analyses of biomass burning events, with related upward injections of CO and their subsequent
690 transport to the UT being implicated. Based on fire counts from satellite data (see e.g., Duncan et
691 al., 2003, 2007), a March biomass burning maximum has been associated with the northern
692 hemisphere (mainly from Southeast Asia, but also from northern Africa); outflow from the Asian
693 monsoon contributes to the August NH maximum. The September/October maximum arises from
694 the southern hemisphere (Indonesia, Malaysia, Southern Africa, Brazil). We should also note
695 (more broadly) that the climatological double maximum CO structure measured by MLS near 215
696 hPa over the broader (20°S–20°N) tropics is well matched by MIPAS CO zonal means (see SPARC
697 DI, 2017, chapter 4). At 12°N, however, the lack of correlation between the model variations and
698 those deduced from MLS in Fig. 11 appears to stem from the poorly modeled double maximum
699 structure; we also find that these poorer fits occur more generally throughout the northern tropics.
700 The model underestimates the boreal winter buildup of CO (Gaubert et al., 2020; 2023), which

701 may explain a poor representation of the northern hemisphere March/April maximum. Also,
702 biomass burning emission biases can vary regionally and this might explain some of the
703 model/data differences, with some regions providing somewhat better comparisons than others.
704 We do not ascribe the larger model/MLS discrepancies at 215 hPa in the northern tropics to an
705 undue influence of the MLS a priori on the retrievals in this region, as the (averaged) a priori MLS
706 values (although not shown in Fig. 11) follow the WACCM-CEDS fields quite well, and the MLS
707 CO retrievals are producing significantly different variations. To explore this hemispherical
708 asymmetry further, we show CO column comparisons between zonal mean time series from
709 MOPITT, CAM-chem-CEDS and WACCM-CEDS in Fig. 12; all CO columns are averaged over
710 the same latitudes (10°N–14°N and 10°S–14°S). We obtain much better agreement in the phasing
711 of these CO column comparisons for 12°N than we do in the model versus MLS CO comparisons
712 at 215 hPa in Fig. 11. This is clearly seen in the time series evolution, as well as in the correlation
713 coefficients shown in both of these Figures, although R is smaller at 12°N than at 12°S in Fig. 12
714 (but still about 0.75 to 0.8). We also look at this issue for the gridded fields and provide R values
715 for the 12°N and 12°S bins in Fig. 13, where we superpose the column CO model results versus
716 MOPITT and the 215 hPa model results versus MLS as a function of longitude. Again, we observe
717 that R is much higher for the CO total columns than for the 215 hPa level, especially so in the
718 northern tropics. The patterns versus longitude indicate that poorer correlations exist over the
719 Atlantic Ocean (just West of the Greenwich meridian) than over land masses. We do not have clear
720 explanations for the exact patterns in Fig. 13, except for the suggestion that regions with strong
721 land convection might show better UT correlations between models and data, while outflow
722 regions (downwind of convection) in the upper troposphere could be more poorly modeled. The
723 models do not follow the observed UT CO seasonal behavior in a narrow UT region of the northern
724 tropics, even if the modeled seasonal total columns compare well to MOPITT columns in that
725 region. More in-depth analysis would be needed to probe whether this might be caused by a poor
726 representation of emissions and/or transport to this region. Alternatively, it might be that currently
727 unaccounted for variations of the MLS vertical averaging kernels could affect the (properly
728 smoothed) model values in the northern hemisphere tropics at 215 hPa, in ways that are somehow
729 significantly different than what we show in Fig. S3; this is highly unlikely, given that the
730 smoothed model plots in this Figure hardly change if we replace the tropical MLS averaging kernel
731 values used in that plot by kernels appropriate for 70°N. Another potential issue might be poorly

732 understood cloud impacts on the 215 hPa MLS retrievals, specifically in the northern hemisphere
733 tropics; although this is speculative, it might be worth exploring in the future.

734 **3.2.3 CO mapped trends and variability**

735 In Fig. 14, we show the mapped CO trend results for MLS and all three simulations (WACCM-
736 CEDS, CAM-chem-CAMS, and CAM-chem-CEDS) at 147 and 215 hPa. As seen above, MLS
737 CO trends in the UT are generally negative, with the more statistically significant result occurring
738 at 147 hPa (where the trends are more negative than at 215 hPa). There is an indication of slightly
739 positive trends over or near western Africa, mainly at 215 hPa, although this is not statistically
740 significant. The binned model results from CAM-chem-CAMS confirm the zonal mean view from
741 this model, with mostly positive trends, in contrast to the generally negative tendencies in the MLS
742 trend results. The average trends (from both pressure levels) based on all grid cells for MLS is -
743 0.25 \% yr^{-1} , as opposed to $+0.24 \text{ \% yr}^{-1}$ obtained from CAM-chem-CAMS. Of note, these values lie
744 well outside twice the standard errors in the means (of 0.1 \% yr^{-1}), although one should understand
745 that there are limitations in the use of such a small error bar, given the existence of correlations in
746 atmospheric variability between the various bins. When the CEDS emissions are used, as done for
747 WACCM-CEDS and CAM-chem-CEDS, there is a general decrease in the UT CO trends, with
748 some small negative values, although the vast majority of the model CO trends obtained here are
749 not statistically different from zero within any given bin. The averaged UT mapped trend for CAM-
750 chem-CEDS is 0.0 \% yr^{-1} , with twice the standard error in the mean also about 0.1 \% yr^{-1} . While
751 the use of the model CEDS emissions does lead to a better model agreement with the gridded MLS
752 UT CO trends, the MLS-derived trends are still, on the whole, more negative than these simulated
753 CO trends.

754 For CO, we repeat in Fig. 15 the explained variance analysis provided in Fig. 6 for O₃. Overall,
755 the full fits explain less of the variability in the CO case, in part because of the large ENSO-related
756 peaks that occur throughout the MLS and WACCM-CEDS records, which the regression model,
757 as designed, can only imperfectly match. Also, there are regions in the southern tropics where the
758 annual cycle in the model is better fit by the regression than in the MLS case, and this translates
759 to a somewhat better overall full fit. For both MLS and model, the semi-annual cycle component
760 shows peaks over the South Atlantic region, which is likely linked to biomass burning in Africa
761 and related CO transport to the UT following convective activity (e.g., Duncan et al., 2007; Park

762 et al., 2013, 2021). As for the ozone case, the QBO-related UT variability in the tropics is very
763 small (as seen from the QBO R^2 contributions). For both MLS and model representations, the
764 ENSO-related correlation patterns are broadly similar to the ozone case, in that there is larger
765 variance in the more extreme longitudes of both western and eastern sides. As for O_3 , there are
766 somewhat smaller variance contributions in the Eastern hemisphere from ENSO and the semi-
767 annual term than in the MLS case. At 215 hPa (see Fig. S6), the ENSO variance contribution is
768 slightly larger than at 147 hPa only in a small number of bins, but the overall ENSO-related
769 patterns are not stronger, as seen also in the CO sensitivity coefficients to ENSO in Figure 16
770 below, which shows only slight differences between the two pressure levels.
771

772 **3.2.4 CO discussion**

773 **Regarding the CO climatology**, the models underestimate the MLS UT values by up to 20%,
774 and these differences could be readily caused by systematic biases in either MLS or the models,
775 or both. Park et al. (2013) also found that model CO values from a (WACCM4) simulation at
776 147 hPa were smaller than the ACE-FTS (and MLS) CO abundances, especially in the SH sub-
777 tropics; they attributed this to a possible underestimation of surface emissions or transport via deep
778 convection. We note that low biases in simulated tropospheric CO have also been found before at
779 northern latitudes and may arise from various factors, such as underestimated CO emissions, high
780 biases in modeled tropospheric OH (Strode et al., 2016; Gaubert et al., 2023), or issues with
781 simulated CO dry deposition rates (Stein et al., 2014). Based on our model/MLS comparisons of
782 UT CO seasonal changes, we find significantly poorer matches at 215 hPa in the northern tropics
783 than in the southern tropics. The detailed causes of this discrepancy are currently not clear to us,
784 given the better matches (correlation coefficients) we obtain between MOPITT total CO columns
785 and modeled CO columns. Potential causes could include model inaccuracies (possibly related to
786 convection and/or CO emissions and subsequent transport in this fairly narrow latitude region), or
787 an alternate explanation having to do with poorly understood limitations of the MLS data in this
788 same region.

789 For the CO trends, the average tropical MLS UT trend is $-0.25 \pm 0.30 \text{ \%yr}^{-1}$, whereas the
790 corresponding trends from CAM-chem-CEDS and WACCM-CEDS are close to zero (0.0 ± 0.14
791 \%yr^{-1}) for this region; these average trend results are statistically in agreement, even if the MLS
792 CO trends tend to generally be more negative than the simulation results. However, the CAM-

793 chem-CAMS simulations (which use CAMS anthropogenic CO emissions, see sect. 2.2), yield
794 statistically significant positive average tropical UT CO trends ($+0.22 \pm 0.19 \text{ \%yr}^{-1}$). More
795 specifically, these simulated latitude-dependent trends are significantly different from the MLS
796 CO trends in the 12°N - 24°N latitude bins. Larger MLS CO abundances in 2020 explain why the
797 MLS CO UT trends are more negative if one stops the analyses in 2018 or 2019. The mapped
798 MLS CO trends in the UT are also negative, with the more statistically significant result (stronger
799 negative trends) occurring at 147 hPa.

800 While there have not been any past decades-long trend estimates for CO in the broad tropical
801 UT region, our results yield somewhat smaller rates of decrease than other trends mentioned in the
802 Introduction, for example -0.5 to -2 \%yr^{-1} , based on IAGOS UT data at northern midlatitudes
803 (Cohen et al., 2018). The mapped model UT CO trends obtained here confirm the zonal mean
804 model results. Column CO in the free troposphere has generally shown decreasing trends since the
805 turn of the century, typically between about -0.5 and -1.5 \%yr^{-1} , as observed in particular by
806 MOPITT and AIRS (Worden et al., 2013a, Strode et al., 2016; Buchholz et al., 2021; Hedelius et
807 al., 2021). Liu et al. (2022) presented a recent analysis of MOPITT CO data from 2005–2018,
808 along with tropospheric model comparisons to observed CO and O₃ time series. These authors
809 found (as shown here and described for MLS and ACE-FTS data by Park et al., 2021) that their
810 modeled and observational time series both exhibit large interannual variability, with some of the
811 largest interannual changes driven by El Niño events in 2006 and 2015 and related biomass burning
812 and CO enhancements tied to droughts over the Indonesian region (see also Logan et al., 2008;
813 Zhang et al., 2011; Livesey et al., 2013; Worden et al., 2013b; Park et al., 2013; Field et al., 2016).
814 Liu et al. (2022) found that modeled CO column trends over various regions of the globe were
815 generally negative, although a lower latitude region (India) exhibited a positive model trend. Jiang
816 et al. (2017) provide some arguments (and other references) pointing to flat biomass burning
817 emission trends over Africa for the first 10–15 years since the turn of the century. Not including
818 the strong tropical anomaly caused by El Niño in 2015, they infer a negative trend in global
819 biomass burning emissions. Uncertainties in the temporal evolution of OH (a major sink for CO)
820 could also explain model CO trend issues. However, Jiang et al. (2017) implied that changes in
821 global OH abundances could not readily explain global CO decreases, given constraints from
822 methyl chloroform surface data (this species also having OH as a major sink, as discussed by
823 Montzka et al., 2011) and despite large uncertainties in OH, especially during the last decade.

824 Rather, these authors conclude that decreasing CO emissions from anthropogenic and biomass
825 burning sources are the main cause of tropospheric CO decreases, although some regional
826 increasing emission trends do exist. While a systematic model bias cannot readily lead to a
827 significant discrepancy in model trend estimates (in percent per year) versus observations, time-
828 dependent emission biases could (e.g., Gaubert et al., 2023). To first order, the decreasing UT CO
829 tropical trends derived from MLS for 2005–2020 agree with (but tend to be smaller in magnitude
830 than) total column CO trends discussed previously in the literature. As discussed by others, some
831 temporal non-linearity in CO trends may be responsible for some of the differences between past
832 tropospheric CO trend results over different periods.

833 For CO in particular, the temporal variability that MLS has observed in the upper troposphere
834 is difficult to fit completely using standard linear regression, given the existence of short-term
835 variability in the troposphere (e.g., Dunkerton and Crum, 1995; Ziemke et al., 2015), as well as
836 large episodic and somewhat random enhancements in the UT CO abundances. Regarding this CO
837 variability, we note that ACE-FTS UT CO monthly zonal mean time series track those from MLS,
838 as shown by Park et al. (2021); this helps to validate the UT time series and variability from MLS.
839 We find that the CO sensitivity to ENSO is much more spatially uniform in sign than the O₃
840 sensitivity; UT O₃ generally increases toward the tropopause while CO decreases, leading to
841 opposite sensitivities to increased upwelling phase over the Pacific (Figs. 7 and 16). In some
842 regions, the CO sensitivity has the same sign as for ozone, and in other regions, it differs;
843 moreover, the model’s UT CO sensitivity coefficient to ENSO seems to broadly match the
844 observational sensitivity from MLS, as it shows positive values throughout the tropics. These
845 different behaviors between tropical UT O₃ and CO seem to mainly reflect a stronger (and positive)
846 sensitivity to biomass burning events in the case of CO.

847

848 **5 Conclusions**

849 We have analyzed tropical ozone (O₃) and carbon monoxide (CO) distributions in the upper
850 troposphere (UT) and their temporal changes for 2005–2020 using Aura Microwave Limb Sounder
851 (MLS) observations and chemistry climate model simulations. Upper tropospheric trends and
852 variability diagnostics were obtained from multiple linear regression analyses.

853

854 ***Tropical UT O₃:***

855 We have compared the model and MLS annual ozone climatologies, focusing on the 147 hPa
856 and 215 hPa pressure levels; the model abundances are typically ~5–15% smaller than MLS O₃ at
857 215 hPa, but larger than the MLS values at 147 hPa by ~20%. MLS O₃ has an averaged UT zonal
858 mean trend at 20°S–20°N of $+0.39 \pm 0.28$ %yr⁻¹. We obtain excellent agreement with the above
859 result from the (averaged) CAM-chem-CEDS O₃ zonal mean trends (0.38 ± 0.28 %yr⁻¹) and
860 somewhat poorer agreement from the smaller WACCM-CEDS trends (0.21 ± 0.23 %yr⁻¹). Our
861 analyses for specific latitude/longitude bins yield positive mapped O₃ trends up to 1.4 %yr⁻¹ over
862 Indonesia and East of that region, as well as over tropical Africa and the tropical Atlantic. Positive
863 tropical UT mapped O₃ trends are generally captured by the model simulations, although in a more
864 muted way. We find broad similarities (and some differences) between the mapped MLS UT O₃
865 trends and corresponding mapped trends of tropospheric column ozone for the same time period.
866

867 ***Tropical UT CO:***

868 The model climatologies generally show an underestimate versus the MLS CO climatology,
869 with model average biases usually about -10% to -20%. Also, in the northern hemisphere tropics,
870 we find significantly poorer model fits to the observed phasing of CO seasonal changes at 215 hPa
871 than at 147 hPa. This discrepancy is much smaller for the comparison of modeled and
872 Measurements of Pollution in the Troposphere (MOPITT) V9J CO columns. The MLS zonal mean
873 CO UT trend is -0.25 ± 0.30 %yr⁻¹, whereas the corresponding model CO trends are close to zero
874 (0.0 ± 0.14 %yr⁻¹) when the anthropogenic emissions used in CAM-chem and WACCM are taken
875 from Community Emissions Data System (CEDS) version 2. The non-CEDS version of CAM-
876 chem (the CAM-chem-CAMS simulation) yields averaged CO UT trends of 0.22 ± 0.19 %yr⁻¹, in
877 contrast to the negative tendencies prevalent in the MLS CO trends throughout the tropics. The
878 negative MLS tropical UT CO trends for 2005–2020 agree with (but tend to be smaller in
879 magnitude than) previously published total column CO trends. We also find that the sensitivity of
880 UT CO to El Niño / Southern Oscillation (ENSO) is positive at all tropical longitudes, in contrast
881 to the (well-known) dipolar longitudinal structure that exists for the UT O₃ ENSO sensitivity.
882

883 The MLS-derived upper tropospheric tropical trends in O₃ and CO arise from a well-sampled
884 multi-year data set, with the results showing a first-order correlation to large-scale changes in

885 lower tropospheric composition (O_3 increases and CO decreases). We find that there are broad
886 similarities (and a few differences) between the measured UT trends and corresponding results
887 from model simulations, which incorporate state-of-the-art representations of the complex
888 interplay between emissions, photochemistry, convection, and transport in the upper troposphere
889 and lower stratosphere. These results will contribute to the continuing assessments of tropospheric
890 evolution, in particular the large community efforts regarding TOAR-II and CMIP-7.

891 Changes in O_3 precursor emissions have been implicated previously as a driver for global
892 tropospheric O_3 changes (e.g., long-term increases), while decreasing CO emissions from
893 anthropogenic and biomass burning sources have been suggested as the main causes of recent
894 decreases in tropospheric CO. We believe that further investigations into how well different
895 models of O_3 and CO in the tropical UT match the corresponding MLS UT trends are warranted,
896 to provide better understanding of differences between models. There may still be adjustments to
897 make to the models regarding the assumed CO surface emissions, convection, and/or transport-
898 related issues, even though such studies are beyond the scope of this paper. Indeed, biomass
899 burning from Africa or South America and emissions from Asia, followed by transport, can (and
900 will continue to) influence the tropical upper tropospheric abundances of CO and O_3 (e.g.,
901 Tsvilidou et al., 2023). On a longer timescale, the troposphere is a region where the relative
902 importance of multiple factors might change over the multi-decadal timescale of climate change;
903 also, longer-term projections from (free running) models may not be representative of changes
904 from a particular decade or two (see Fiore et al., 2022, regarding model ensemble projections). For
905 example, long-term positive trends in the influx of ozone from the stratosphere to the troposphere
906 may be expected as a result of climate change (Meul et al., 2018), probably with more of an
907 influence on the extra-tropical upper troposphere. Regarding the tropics, Stevenson et al. (2013)
908 showed that a number of chemistry climate model simulations of climate change scenarios yielded
909 long-term ozone decreases in the lower troposphere as a result of enhancements in water vapor
910 (implying more ozone destruction), but low latitude upper tropospheric ozone could be expected
911 to rise, following increased production from lightning. Obtaining accurate enough observations of
912 large-scale tropospheric composition change over the long-term is expected to represent a
913 continuing, but worthy challenge.

914

915 **Data availability.**

916 The MLS data files analyzed here come from the MLS Level 3 data sets (zonal mean and gridded
917 quantities), which are publicly available from the Goddard Earth Sciences Data and Information Services
918 Center (GES DISC) at <https://earthdata.nasa.gov/eosdis/daacs/gesdisc>.
919 The MOPITT Version 9 products are available from NASA through the Earthdata portal
920 (<https://earthdata.nasa.gov/>; https://asdc.larc.nasa.gov/project/MOPITT/MOP03JM_9; or directly from the
921 ASDC archive (<https://asdc.larc.nasa.gov/data/MOPITT/>). We used the following site,
922 ftp://ftp.seismo.nrcan.gc.ca/spaceweather/solar_flux/monthly_averages/solflux_monthly_average.txt to
923 obtain monthly means of the Canadian F10.7 solar flux measurements (Tapping, 2013); these series (see
924 <http://www.spaceweather.gc.ca>) were included in our regression fits. The QBO-related equatorial wind
925 monthly time series were obtained from the public website at [https://www.geo.fu-](https://www.geo.fu-berlin.de/en/met/ag/strat/produkte/qbo)
926 [berlin.de/en/met/ag/strat/produkte/qbo](https://www.geo.fu-berlin.de/en/met/ag/strat/produkte/qbo). The multivariate ENSO index dataset was obtained from the NOAA
927 Physical Sciences Laboratory website at <https://www.psl.noaa.gov/enso/mei/> (Wolter and Timlin, 2011;
928 Zhang et al., 2019). OMI/MLS tropospheric ozone data were obtained from the NASA satellite tropospheric
929 ozone webpage https://acd-ext.gsfc.nasa.gov/Data_services/cloud_slice/.

930

931 **Supplement.** Supplementary material is included as a separate file.

932

933 **Author contributions.** LF analyzed the MLS and model data for trends and variability, and prepared the
934 manuscript, along with contributions from all co-authors. DEK, CGB, and BG provided inputs for running
935 the model runs, as well as properly averaged and formatted outputs from the model, as well as pertinent
936 model-related comments and interpretation of results. JRZ provided TCO datasets and comments on the
937 manuscript. NJL, MJS, WGR, and others on the MLS team provided analyses and expertise to enable the
938 production of the Aura MLS data sets; NJL, MJS, and WGR also provided comments on the manuscript;
939 RAF provided programming assistance for the creation of the MLS data sets and for storage and analyses
940 of the MLS and model files.

941

942 **Competing interests.** The authors declare that they have no conflict of interest.

943

944 **Acknowledgments.** We are thankful to the whole MLS team (past and present) for their contributions over
945 the years to the MLS instrument, data, processing, and database management. We very much acknowledge
946 the referees, who helped improve the initial manuscript with quite a list of useful and detailed comments.
947 We acknowledge the encouragement from Owen Cooper and Helen Worden to link our paper to the
948 TOAR-II Copernicus special issue; thanks also to Kai-Lan Chang for briefly reviewing aspects of our

949 statistical approach regarding the guidelines adopted for reporting TOAR-linked results. WACCM-CEDS
950 is a component of the CESM, supported by the National Science Foundation (NSF). We acknowledge high-
951 performance computing support from Cheyenne (doi:10.5065/D6RX99HX) provided by NCAR's
952 Computational and Information Systems Laboratory, sponsored by the NSF. F10.7 data collection and
953 dissemination are supported by the National Research Council of Canada, with the participation of Natural
954 Resources Canada and support by the Canadian Space Agency. Work at the Jet Propulsion Laboratory,
955 California Institute of Technology, was performed under contract with the National Aeronautics and Space
956 Administration (80NM0018D0004). Copyright 2024. All rights reserved.

957

958 **Financial support.** LF and RAF were funded by the NASA Atmospheric Composition Modeling and
959 Analysis Program (ACMAP). NJL, MJS, and WGR (as well as LF) were supported by the Aura Microwave
960 Limb Sounder project. DEK, BG, and CGB were funded separately by NASA and NSF grants. Part of this
961 material is based on work supported by the National Center for Atmospheric Research, which is a major
962 facility sponsored by the National Science Foundation under Cooperative Agreement No. 1852977. The
963 NSF NCAR MOPITT project is supported by the National Aeronautics and Space Administration (NASA)
964 Earth Observing System (EOS) program.

965 **References**

- 966 Andela, N., Morton, D. C., Giglio, L., Chen, Y., van der Werf, G. R., Kasibhatla, P. S., DeFries, R. S., Collatz, G. J.,
967 Hantson, S., Kloster, S., Bachelet, D., Forrest, M., Lasslop, G., Li, F., Mangeon, S., Melton, J. R., Yue, C., and
968 Randerson, J. T.: A human-driven decline in global burned area, *Science*, 356(6345):1356-1362, doi:
969 10.1126/science.aal4108, 2017.
- 970 Bouarar, I., Gaubert, B., Brasseur, G. P., Steinbrecht, W., Doumbia, T., Tilmes, S., et al.: Ozone anomalies in the free
971 troposphere during the COVID-19 pandemic, *Geophys. Res. Lett.*, 48, e2021GL094204.
972 <https://doi.org/10.1029/2021GL094204>, 2021.
- 973 Bourassa, A. E., Degenstein, D. A., Randel, W. J., Zawodny, J. M., Kyrölä, E., McLinden, C. A., Sioris, C. E., and
974 Roth, C. Z.: Trends in stratospheric ozone derived from merged SAGE II and Odin-OSIRIS satellite observations,
975 *Atmos. Chem. Phys.*, 14, 6983-6994, <https://doi.org/10.5194/acp-14-6983-2014>, 2014.
- 976 Brasseur, G. P., Gupta, M., Anderson, B. E., Balasubramanian, S., Barrett, S., Duda, D., Fleming, G., Forster, P. M.,
977 Fuglestedt, J., Gettelman, A., Halthore, R. N., Jacob, D., Jacobson, M. Z., Khodayari, A., Liou, K.-N., Lund, M.
978 T., Miake-Lye, R. C., Minnis, P., Olsen, S., Penner, J. E., Prinn, R., Schumann, U., Selkirk, H. B., Sokolov, A.,
979 Unger, N., Wolfe, P., Wong, H.-W., Wuebbles, D. W., Yi, B., Yang, P., and Zhou, C.: Impact of aviation on
980 climate, FAA's Aviation Climate Change Research Initiative (ACCRI) Phase II, *Bull. Amer. Met. Soc.*,
981 10.1175/BAMS-D-13-00089.1, 2016.
- 982 Buchholz, B. R., Worden H. M., et al.: Air pollution trends measured from Terra: CO and AOD over industrial, fire-
983 prone, and background regions, *Remote Sensing of Environment*, 256, 112275,
984 <https://doi.org/10.1016/j.rse.2020.112275>, 2021.
- 985 Burkholder, J. B., Sander, S. P., Abbatt, J. P. D., Barker, J. R., Cappa, C., Crouse, J. D., Dibble, T. S., Huie, R. E.,
986 Kolb, C. E., Kurylo, M. J., Orkin, V. L., Percival, C. J., Wilmouth, D. M., and Wine, P. H.: Chemical kinetics and
987 photochemical data for use in atmospheric studies, Evaluation No. 19, JPL Publication 19-5, Jet Propulsion
988 Laboratory, California Institute of Technology, Pasadena, <http://jpldataeval.jpl.nasa.gov> (last access: 1 March
989 2022), 2019.
- 990 Calvo, N., Garcia, R. R., Randel, W. J., and Marsh, D.: Dynamical mechanism for the increase in tropical upwelling
991 in the lowermost tropical stratosphere during warm ENSO events, *J. Atmos. Sci.*, 67, 2331–2340,
992 <https://doi.org/10.1175/2010JAS3433.1>, 2010.
- 993 Chandra, S., Ziemke, J. R., Min, W., and Read, W. G.: Effects of 1997–1998 El Niño on tropospheric ozone and water
994 vapor, *Geophys. Res. Lett.*, 25(20), 3867–3870, <https://doi.org/10.1029/98GL02695>, 1998.
- 995 Coddington, O., Lean, J., Pilewskie, P., Snow, M., and Lindholm, D.: A solar irradiance climate data record, *Bull.*
996 *Amer. Meteor. Soc.*, <https://doi.org/10.1175/BAMS-D-14-00265.1>, 2016.
- 997 Cohen, Y., Petetin, H., Thouret, V., Marécal, V., Josse, B., Clark, H., Sauvage, B., Fontaine, A., Athier, G., Blot, R.,
998 Boulanger, D., Cousin, J.-M., and Nédélec, P.: Climatology and long-term evolution of ozone and carbon
999 monoxide in the upper troposphere–lower stratosphere (UTLS) at northern midlatitudes, as seen by IAGOS from
1000 1995 to 2013, *Atmos. Chem. Phys.*, 18, 5415–5453, <https://doi.org/10.5194/acp-18-5415-2018>, 2018.

1001 Collins, W. J., Derwent, R. G., Garnier, B., C. E. Johnson, C. E., Sanderson, M. G., and Stevenson, D. S.: Effect of
1002 stratosphere-troposphere exchange on the future tropospheric ozone trend, *J. Geophys. Res.*, 108, D12, 8528,
1003 <https://doi.org/10.1029/2002JD002617>, 2003.

1004 Cooper, O. R., Parrish, D. D., Ziemke, J. R., Balashov, N. V., Cupeiro, M., Galbally, I., Gilge, S., Horowitz, L., Jensen,
1005 N. R., Lamarque, J.-F., Naik, V., Oltmans, S. J., Schwab, J., Shindell, D. T., Thompson, A. M., Thouret, V., Wang,
1006 Y., and Zbinden, R. M.: Global distribution and trends of tropospheric ozone: An observation-based review,
1007 *Elementa*, 2, 000029, <https://doi.org/10.12952/journal.elementa.000029>, 2014.

1008 Crutzen, P. J.: A discussion of the chemistry of some minor constituents in stratosphere and troposphere, *Pure Appl.*
1009 *Geophys.*, 106, 1385–1399, <https://doi.org/10.1007/BF00881092>, 1973.

1010 Crutzen, P. J., and Andreae, M. O.: Biomass burning in the tropics: Impact on atmospheric chemistry and
1011 biogeochemical cycles, *Science*, 250, 1669–1678, <https://doi.org/10.1126/science.250.4988.1669>, 1990.

1012 Danabasoglu, G., Lamarque, J.-F., Bacmeister, J., Bailey, D. A., DuVivier, A. K., Edwards, J., Emmons, L. K.,
1013 Fasullo, J., Garcia, R., Gettelman, A., Hannay, C., Holland, M. M., Large, W. G., Lauritzen, P. H., Lawrence, D.
1014 M., Lenaerts, J. T. M., Lindsay, K., Lipscomb, W. H., Mills, M. J., Neale, R., Oleson, K. W., Otto-Bliesner, B.,
1015 Phillips, A. S., Sacks, W., Tilmes, S., van Kampenhout, L., Vertenstein, M., Bertini, A., Dennis, J., Deser, C.,
1016 Fischer, C., Fox-Kemper, B., Kay, J. E., Kinnison, D. E., Kushner, P. J., Larson, V. E., Long, M. C.,
1017 Mickelson, S., Moore, J. K., Nienhouse, E., Polvani, L., Rasch, P. J., and Strand, W. G.: The Community Earth
1018 System Model Version 2 (CESM2), *J. Adv. in Modeling Earth Systems*, 12,
1019 <https://doi.org/10.1029/2019MS001916>, 2020.

1020 Darnenov, A., and da Silva, A. M.: The Quick Fire Emissions Dataset (QFED) - Documentation of versions 2.1, 2.2
1021 and 2.4, NASA/TM–2015–104606, 2015;38:183, <http://gmao.gsfc.nasa.gov/pubs/tm/>, 2014.

1022 Davis, N. A., Callaghan, P., Simpson, I. R., and Tilmes, S.: Specified dynamics scheme impacts on wave-mean flow
1023 dynamics, convection, and tracer transport in CESM2 (WACCM6), *Atmos. Chem. Phys.*, 22, 197–
1024 214, <https://doi.org/10.5194/acp-22-197-2022>, 2022.

1025 Deeter, M., Francis, G., Gille, J., Mao, D., Martínez-Alonso, S., Worden, H., Ziskin, D., Drummond, J., Commane,
1026 R., Diskin, G., and McKain, K.: The MOPITT Version 9 CO product: sampling enhancements and validation,
1027 *Atmos. Meas. Tech.*, 15, 2325–2344, <https://doi.org/10.5194/amt-15-2325-2022>, 2022.

1028 Doherty, R. M., Stevenson, D. S., Johnson, C. E., Collins, W. J., and Sanderson, M. G.: Tropospheric ozone and El
1029 Niño–Southern Oscillation: Influence of atmospheric dynamics, biomass burning emissions, and future climate
1030 change, *J. Geophys. Res.-Atmos.*, 111, D19304, <https://doi.org/10.1029/2005JD006849>, 2006.

1031 Duncan, B. N., Martin, R. V., Staudt, A. C., Yevich, R., and Logan, J. A.: Interannual and seasonal variability of
1032 biomass burning emissions constrained by satellite observations, *J. Geophys. Res.-Atmos.*, 108, 4100,
1033 <https://doi.org/10.1029/2002jd002378>, 2003.

1034 Duncan, B. N., Strahan, S. E., Yoshida, Y., Steenrod, S. D., and Livesey, N.: Model study of the cross-tropopause
1035 transport of biomass burning pollution, *Atmos. Chem. Phys.*, 7, 3713–3736, [https://doi.org/10.5194/acp-7-3713-](https://doi.org/10.5194/acp-7-3713-2007)
1036 [2007](https://doi.org/10.5194/acp-7-3713-2007), 2007.

1037 Dunkerton, T. J., and Crum, F. X.: Eastward propagating eastward ~2- to 15-day equatorial convection and its relation
1038 to the tropical intraseasonal oscillation, *J. Geophys. Res.*, 100, D12, 25781–25790,
1039 <http://dx.doi.org/10.1029/95JD02678>, 1995.

1040 Ebojje, F., Burrows, J. P., Gebhardt, C., Ladstter-Weienmayer, A., von Savigny, C., Rozanov, A., Weber, M., and
1041 Bovensmann, H.: Global tropospheric ozone variations from 2003 to 2011 as seen by SCIAMACHY, *Atmos.*
1042 *Chem. Phys.*, 16, 417–436, <https://doi.org/10.5194/acp-16-417-2016>, 2016.

1043 Efron, B., and Tibshirani, R.: *An Introduction to the Bootstrap*, Monographs on Statistics and Applied Probability 57,
1044 Chapman and Hall, 1993.

1045 Emmons, L. K., Walters, S., Hess, P. G., Lamarque, J. F., Pfister, G. G., Fillmore, D., Granier, C. Guenther, A.
1046 Kinnison, D., Laepple, T., Orlando J., Tie, X., Tyndall, G., Wiedinmyer, C., Baughcum S. L., and Kloster,
1047 S.: Description and evaluation of the Model for Ozone and Related chemical Tracers, version 4 (MOZART-
1048 4). *Geoscientific Model Development*, 3(1), 43-67. <https://doi.org/10.5194/gmd-3-43-2010>.

1049 Emmons, L. K., Schwantes, R. H., Orlando, J. J., Tyndall, G., Kinnison, D., Lamarque, J.-F., Marsh, D., Mills, M. J.,
1050 Tilmes, S., Bardeen, C., Buchholz, R. R., Conley, A., Gettelman, A., Garcia, R., Simpson, I., Blake, D. R.,
1051 Meinardi, S., and Pétron, G.: The Chemistry Mechanism in the Community Earth System Model version 2
1052 (CESM2), *Journal of Advances in Modeling Earth Systems*, 12, <https://doi.org/10.1029/2019MS001882>, 2020.

1053 Feely, R. A., Gammon, R. H., Taft, B. A., Pullen, P. E., Waterman, L. S., Conway, T. J., Gendron, J. F., and
1054 Wisegarver, D. P.: Distribution of chemical tracers in the eastern equatorial Pacific during and after the 1982–
1055 1983 El Niño/Southern Oscillation Event, *J. Geophys. Res.-Oceans*, 92, 6545–6558,
1056 <https://doi.org/10.1029/JC092iC06p06545>, 1987.

1057 Field, R. D., van der Werf, G. R., Fanin, T., Fetzer, E. J., Fuller, R., Jethva, H., Levy, R., Livesey, N. J., Luo, M.,
1058 Torres, O., and Worden, H. M.: Indonesian fire activity and smoke pollution in 2015 show persistent nonlinear
1059 sensitivity to El Niño-induced drought, *Proceedings of the National Academy of Sciences of the United States of*
1060 *America*, 113, 9204–9209, <https://doi.org/10.1073/pnas.1524888113>, 2016.

1061 Fiore, A. M., Hancock, S. E., Lamarque, J.-F., Correa, G. P., Chang, K.-L., Ru, M., Cooper, O., Gaudel, A., Polvani,
1062 L. M., Sauvage, B., and Ziemke, J. R.: Understanding recent tropospheric ozone trends in the context of large
1063 internal variability: a new perspective from chemistry-climate model ensembles, *Environ. Res.: Climate* 1 (2022)
1064 025008, <https://doi.org/10.1088/2752-5295/ac9cc2>, 2022.

1065 Froidevaux, L., Kinnison, D. E., Wang, R., Anderson, J., and Fuller, R. A.: Evaluation of CESM1 (WACCM) free-
1066 running and specified dynamics atmospheric composition simulations using global multispecies satellite data
1067 records, *Atmos. Chem. Phys.*, 19, 4783–4821, <https://doi.org/10.5194/acp-19-4783-2019>, 2019.

1068 Froidevaux, L., Kinnison, D. E., Santee, M. L., Millán, L. F., Livesey, N. J., Read, W. G., Bardeen, C. G., Orlando, J.
1069 J., and Fuller, R. A.: Upper stratospheric ClO and HOCl trends (2005–2020): Aura Microwave Limb Sounder and
1070 model results, *Atmos. Chem. Phys.*, 22, 4779–4799, <https://doi.org/10.5194/acp-22-4779-2022>, 2022.

1071 Gaubert, B., Worden, H. M., Arellano, A. F. J., Emmons, L. K., Tilmes, S., Barré, J., Martínez Alonso, S., Vitt, F.,
1072 Anderson, J. L., Alkemade, F., Houweling, S., and Edwards, D. P.: Chemical feedback from decreasing carbon
1073 monoxide emissions, *Geophys. Res. Lett.*, 44, 9985–9995, <https://doi.org/10.1002/2017GL074987>, 2017.

1074 Gaubert, B., Emmons, L. K., Raeder, K., Tilmes, S., Miyazaki, K., Arellano Jr., A. F., Elguindi, N., Granier, C., Tang,
1075 W., Barré, J., Worden, H. M., Buchholz, R. R., Edwards, D. P., Franke, P., Anderson, J. L., Saunio, M., Schroeder,
1076 J., Woo, J.-H., Simpson, I. J., Blake, D. R., Meinardi, S., Wennberg, P. O., Crouse, J., Teng, A., Kim, M.,
1077 Dickerson, R. R., He, H., Ren, X., Pusede, S. E., and Diskin, G. S.: Correcting model biases of CO in East Asia:
1078 impact on oxidant distributions during KORUS-AQ, *Atmos. Chem. Phys.*, 20, 14617–14647,
1079 <https://doi.org/10.5194/acp-20-14617-2020>, 2020.

1080 Gaubert, B., Edwards, D. P., Anderson, J. L., Arellano, A.F., Barré, J., Buchholz, R.R., Darras, S., Emmons, L.K.,
1081 Fillmore, D., Granier, C., et al.: Global Scale Inversions from MOPITT CO and MODIS AOD, *Remote Sens.* 15,
1082 4813, <https://doi.org/10.3390/rs15194813>, 2023.

1083 Gaudel, A., Cooper, O. R., Ancellet, G., Barret, B., Boynard, A., Burrows, J. P., Clerbaux, C., Coheur, P. F., Cuesta,
1084 J., Cuevas, E., Doniki, S., Dufour, G., Ebojje, F., Foret, G., Garcia, O., Granados-Muñoz, M. J., Hannigan, J. W.,
1085 Hase, F., Hassler, B., Huang, G., Hurtmans, D., Jaffe, D., Jones, N., Kalabokas, P., Kerridge, B., Kulawik, S.,
1086 Latter, B., Leblanc, T., Le Flochmoën, E., Lin, W., Liu, J., Liu, X., Mahieu, E., McClure-Begley, A., Neu, J. L.,
1087 Osman, M., Palm, M., Petetin, H., Petropavlovskikh, I., Querel, R., Rahpoe, N., Rozanov, A., Schultz, M. G.,
1088 Schwab, J., Siddans, R., Smale, D., Steinbacher, M., Tanimoto, H., Tarasick, D. W., Thouret, V., Thompson, A.
1089 M., Trickl, T., Weatherhead, E., Wespes, C., Worden, H. M., Vigouroux, C., Xu, X., Zeng, G., and Ziemke, J.:
1090 Tropospheric Ozone Assessment Report: Present-day distribution and trends of tropospheric ozone relevant to
1091 climate and global atmospheric chemistry model evaluation, *Elem. Sci. Anth.*, 6, 39,
1092 <https://doi.org/10.1525/elementa.291>, 2018.

1093 Gaudel, A., Cooper, O. R., Chang, K.-L., Bourgeois, I., Ziemke, J. R., Strode, S. A., Oman, L. D., Sellitto, P., Nédélec,
1094 P., Blot, R., Thouret, V., and Granier, C.: Aircraft observations since the 1990s reveal increases of tropospheric
1095 ozone at multiple locations across the Northern Hemisphere, *Sci. Adv.*, 6, eaba8272,
1096 <https://doi.org/10.1126/sciadv.aba8272>, 2020.

1097 Gaudel, A., Bourgeois, I., Li, M., Chang, K.-L., Ziemke, J., Sauvage, B., Stauffer, R. M., Thompson, A. M., Kollonige,
1098 D. E., Smith, N., Hubert, D., Keppens, A., Cuesta, J., Heue, K.-P., Veffkind, P., Aikin, K., Peischl, J., Thompson,
1099 C. R., Ryerson, T. B., Frost, G. J., McDonald, B. C., and Cooper, O. R.: Tropical tropospheric ozone distribution
1100 and trends from in situ and satellite data, *Atmos. Chem. Phys.*, <https://doi.org/10.5194/egusphere-2023-3095>,
1101 2024.

1102 Gelaro, R., McCarty, W., Suarez, M. J., Todling, R., Molod, A., Takacs, L., Randles, C. A., Darmenov,
1103 A., Bosilovich, M. G., Reichle, R., Wargan, K., Coy, L., Cullather, R., Draper, C., Akella, S., Buchard,
1104 V., Conaty, A., da Silva, A. M., Gu, W., Kim, G.-K., Koster, R., Lucchesi, R., Merkova, D., Nielsen, J.
1105 E., Partyka, G., Pawson, S., Putman, W., Rienecker, M., Schubert, S. D., Sienkiewicz, M., and Zhao, B.: The
1106 Modern-Era Retrospective Analysis for Research and Applications, Version 2 (MERRA2), *J. Clim.*, 30, 5419–
1107 5454, <https://doi.org/10.1175/JCLI-D-16-0758.1>, 2017.

1108 Gettelman, A., Mills, M. J., Kinnison, D. E., Garcia, R. R., Smith, A. K., Marsh, D. R., Tilmes, S., Vitt, F., Bardeen,
1109 C. G., McInerny, J., Liu, H.-L., Solomon, S. C., Polvani, L. M., Emmons, L. K., Lamarque, J.-F., Richter, J. H.,
1110 Glanville, A. S., Bacmeister, J. T., Phillips, A. S., Neale, R. B., Simpson, I. R., DuVivier, A. K., Hodzic, A., and

1111 Randel, W. J.: The Whole Atmosphere Community Climate Model version 6 (WACCM6), *J. Geophys. Res.-*
1112 *Atmos.*, 124, 12,380–12,403, <https://doi.org/10.1029/2019JD030943>, 2019.

1113 Gratz, L. E., Jaffe, D. A., and Hee, J. R.: Causes of increasing ozone and decreasing carbon monoxide in springtime
1114 at the Mt. Bachelor Observatory from 2004 to 2013, *Atm. Env.*, 109, 323–330,
1115 <http://dx.doi.org/10.1016/j.atmosenv.2014.05.076>, 2015.

1116 He, H., Stehr, J. W., Hains, J. C., Krask, D. J., Doddridge, B. G., Vinnikov, K. Y., Canty, T. P., Hosley, K. M.,
1117 Salawitch, R. J., Worden, H. M., and Dickerson, R. R.: Trends in emissions and concentrations of air pollutants in
1118 the lower troposphere in the Baltimore/Washington airshed from 1997 to 2011, *Atmos. Chem. Phys.*, 13,
1119 <https://doi.org/10.5194/acp-13-7859-2013>, 2013.

1120 Hedelius, J. K., Toon, G. C., Buchholz, R. R., Iraci, L. T., Podolske, J. R., Roehl, C. M., et al.: Regional and urban
1121 column CO trends and anomalies as observed by MOPITT over 16 years, *J. Geophys. Res.-Atmos.*, 126,
1122 e2020JD033967, <https://doi.org/10.1029/2020JD033967>, 2021.

1123 Hegglin, M. I., and Shepherd, T. G.: Large Climate-Induced Changes in Ultraviolet Index and Stratosphere-to
1124 Troposphere Ozone Flux, *Nature Geoscience*, 2, 687–691, <http://dx.doi.org/10.1038/ngeo604>, 2009.

1125 Hegglin, M. I., Tegtmeier, S., Anderson, J., Bourassa, A. E., Brohede, S., Degenstein, D., Froidevaux, L., Funke, B.,
1126 Gille, J., Kasai, Y., Kyrölä, E. T., Lumpe, J., Murtagh, D., Neu, J. L., Pérot, K., Remsberg, E. E., Rozanov, A.,
1127 Toohey, M., Urban, J., von Clarmann, T., Walker, K. A., Wang, H.-J., Arosio, C., Damadeo, R., Fuller, R. A.,
1128 Lingenfelter, G., McLinden, C., Pendlebury, D., Roth, C., Ryan, N. J., Sioris, C., Smith, L., and Weigel, K.:
1129 Overview and update of the SPARC Data Initiative: comparison of stratospheric composition measurements from
1130 satellite limb sounders, *Earth Syst. Sci. Data*, 13, 1855–1903, <https://10.5194/essd-13-1855-2021>, 2021.

1131 Hess, P. G., and Zbinden, R.: Stratospheric impact on tropospheric ozone variability and trends: 1990–2009, *Atmos.*
1132 *Chem. Phys.*, 13, 649–674, <https://doi.org/10.5194/acp-13-649-20132013>, 2013.

1133 Heue, K.-P., Coldewey-Egbers, M., Delcloo, A., Lerot, C., Loyola, D., Valks, P., and van Roozendaal, M.: *Atmos.*
1134 *Meas. Tech.*, 9, 5037–5051, <https://doi.org/10.5194/amt-9-5037-2016>, 2016.

1135 Horr, P., Borken-Kleefeld, J., Caro, D., Dessens, O., Endresen, O., Gauss, M., Grewe, V., Hauglustaine, D., Isaksen,
1136 I. S. A., Jockel, P., Lelieveld, J., Myhre, G., Meijer, E., Olivie, D., Prather, M., Schnadt Poberaj, C., Shine, K. P.,
1137 Staehelin, J., Tang, Q., van Aardenne, J., van Velthoven, P., and Sausen, R.: The impact of traffic emissions on
1138 atmospheric ozone and OH: results from QUANTIFY, *Atmos. Chem. Phys.*, 9, 3113–3136, [www.atmos-chem-](http://www.atmos-chem-phys.net/9/3113/2009/)
1139 [phys.net/9/3113/2009/](http://www.atmos-chem-phys.net/9/3113/2009/), 2009.

1140 Hsu, J. and Prather, M. J.: Is the residual vertical velocity a good proxy for stratosphere-troposphere exchange of
1141 ozone?, *Geophys. Res. Lett.*, 41, 9024–9032, <https://doi.org/10.1002/2014GL061994>, 2014.

1142 Huang, L., Fu, R., Jiang, J. H., Wright, J. S., and Luo, M.: Geographic and seasonal distributions of CO transport
1143 pathways and their roles in determining CO centers in the upper troposphere, *Atmos. Chem. Phys.*, 12, 4683–4698,
1144 <https://doi.org/10.5194/acp-12-4683-2012>, 2012.

1145 Huang, L., Fu, R., and Jiang, J. H.: Impacts of fire emissions and transport pathways on the interannual variation of
1146 CO in the tropical upper troposphere, *Atmos. Chem. Phys.*, 14, 4087–4099, [https://doi.org/10.5194/acp-14-4087-](https://doi.org/10.5194/acp-14-4087-2014)
1147 [2014](https://doi.org/10.5194/acp-14-4087-2014), 2014.

1148 Huang, L., Jiang, J. H., Murray, L. T., Damon, M. R., Su, H., and Livesey, N. J.: Evaluation of UTLS carbon monoxide
1149 simulations in GMI and GEOS-Chem chemical transport models using Aura MLS observations, *Atmos. Chem.*
1150 *Phys.*, 16, 5641–5663, <https://doi.org/10.5194/acp-16-5641-2016>, 2016.

1151 Hubert, D., Lambert, J.-C., Verhoelst, T., Granville, J., Keppens, A., Baray, J.-L., Bourassa, A. E., Cortesi, U.,
1152 Degenstein, D. A., Froidevaux, L., Godin-Beekmann, S., Hoppel, K. W., Johnson, B. J., Kyrölä, E., Leblanc, T.,
1153 Lichtenberg, G., Marchand, M., McElroy, C. T., Murtagh, D., Nakane, H., Portafaix, T., Querel, R., Russell III, J.
1154 M., Salvador, J., Smit, H. G. J., Stebel, K., Steinbrecht, W., Strawbridge, K. B., Stübi, R., Swart, D. P. J., Taha,
1155 G., Tarasick, D. W., Thompson, A. M., Urban, J., van Gijssel, J. A. E., Van Malderen, R., von der Gathen, P.,
1156 Walker, K. A., Wolfram, E., and Zawodny, J. M.: Ground-based assessment of the bias and long-term stability of
1157 14 limb and occultation ozone profile data records, *Atmos. Meas. Tech.*, 9, 2497–2534,
1158 <https://doi.org/10.5194/amt-9-2497-2016>, 2016.

1159 Jiang, J. H., Livesey, N. J., Su, H., Neary, L., McConnell, J. C., and Richards, N. A. D.: Connecting surface emissions,
1160 convective uplifting, and long-range transport of carbon monoxide in the upper troposphere: New observations
1161 from the Aura Microwave Limb Sounder, *Geophys. Res. Lett.*, 34, L18812, <https://doi.org/10.1029/2007g1030638>,
1162 2007.

1163 Jiang, Z., Worden, J. R., Worden, H., Deeter, M., Jones, D. B. A., Arellano, A. F., and Henze, D. K.: A 15-year record
1164 of CO emissions constrained by MOPITT CO observations, *Atmos. Chem. Phys.*, 17, 4565–4583,
1165 <https://doi.org/10.5194/acp17-4565-2017>, 2017.

1166 Jones, C. D., Collins, M., Cox, P. M., and Spall, S. A.: The Carbon Cycle Response to ENSO: A Coupled Climate–
1167 Carbon Cycle Model Study, *J. Climate*, 14, 4113–4129, [https://doi.org/10.1175/1520-
1168 0442\(2001\)014<4113:tccte>2.0.CO;2](https://doi.org/10.1175/1520-0442(2001)014<4113:tccte>2.0.CO;2), 2001.

1169 Kinnison, D. E., Brasseur, G. P., Walters, S., Garcia, R. R., Sassi, F., Boville, B. A., Marsh, D. Harvey, L., Randall,
1170 C., Randel, W., Lamarque, J. F., Emmons, L. K., Hess, Orlando, J., Tyndall, G., and Pan, L.: Sensitivity of
1171 chemical tracers to meteorological parameters in the MOZART-3 chemical transport model, *J. Geophys. Res.*,
1172 112, D20302, <https://doi.org/10.1029/2006JD007879>, 2007.

1173 Khalil, M. A. K., and Rasmussen, R. A.: The global cycle of carbon monoxide: trends and mass balance, *Chemosphere*,
1174 20, Nos. 1–2, pp. 227–242, [https://doi.org/10.1016/0045-6535\(90\)90098-E](https://doi.org/10.1016/0045-6535(90)90098-E), 1990.

1175 Kumar, A., Wu, S., Weise, M. F., Honrath, R., Owen, R. C., Helmig, D., Kramer, L., Val Martin, M., and Li, Q.: Free-
1176 troposphere ozone and carbon monoxide over the North Atlantic for 2001–2011, *Atmos. Chem. Phys.*, 13, 12537–
1177 12547, <https://doi.org/10.5194/acp-13-12537-2013>, 2013.

1178 Laken, B. A., and Shahbaz, T.: Satellite-Detected Carbon Monoxide Pollution during 2000–2012: Examining Global
1179 Trends and also Regional Anthropogenic Periods over China, the EU and the USA, *Climate*, 2014, 2, 1-16,
1180 <https://doi.org/10.3390/cli2010001>, 2014.

1181 Lee, D. S., Fahey, D. W., Skowron, A., Allen, M. R., Burkhardt, U., Chen, Q., Doherty, S. J., Freeman, S., Forster, P.
1182 M., Fuglestedt, J., Gettelman, A., De Leon, R. R., Lim, L. L., Lund, M. T., Millar, R. J., Owen, B., Penner, J. E.,
1183 Pitari, G., Prather, M. J., Sausen, R., and Wilcox, L. J.: The contribution of global aviation to anthropogenic climate
1184 forcing for 2000 to 2018, *Atmos. Env.*, 244, 117834, doi.org/10.1016/j.atmosenv.2020.117834, 2021.

1185 Leventidou, E., Weber, M., Eichmann, K.-U., Burrows, J. P., Heue, K.-P., Thompson, A. M., and Johnson, B. J.:
1186 Harmonisation and trends of 20-year tropical tropospheric ozone data, *Atmos. Chem. Phys.*, 18, 9189–9205,
1187 <https://doi.org/10.5194/acp-18-9189-2018>, 2018.

1188 Li, L., and Liu, Y.: Space-borne and ground observations of the characteristics of CO pollution in Beijing, 2000–2010,
1189 *Atmos. Env.*, 45, 2367–2372. <https://doi.org/10.1016/j.atmosenv.2011.02.026>, 2011.

1190 Liu, J., Logan, J. A., Murray, L. T., Pumphrey, H. C., Schwartz, M. J., and Megretskaia, I. A.: Transport analysis and
1191 source attribution of seasonal and interannual variability of CO in the tropical upper troposphere and lower
1192 stratosphere, *Atmos. Chem. Physics*, 13, 129–146. <https://doi.org/10.5194/acp-13-129-2013>, 2013.

1193 Liu, J., Strode, S. A., Liang, Q., Oman, L. D., Colarco, P. R., Fleming, E. L., Manyin, M. E., Douglass, A. R., Ziemke,
1194 J. R., Lamsal, L. N., and Li, C.: Change in tropospheric ozone in the recent decades and its contribution to global
1195 total ozone, *J. Geophys. Res.-Atmos.*, 127, e2022JD037170. <https://doi.org/10.1029/2022JD037170>, 2022.

1196 Livesey, N. J., and Read, W. G.: Direct retrieval of line-of-sight atmospheric structure from limb sounding
1197 observations, *Geophys. Res. Lett.*, 27, 891-894, <https://doi.org/10.1029/1999GL010964>, 2000.

1198 Livesey, N. J., Van Snyder, W., Read, W. G., and Wagner, P. A.: Retrieval algorithms for the EOS Microwave Limb
1199 Sounder (MLS), *IEEE Trans. Geosci. Remote Sens.*, 44, 1144-1155, <https://doi.org/10.1109/TGRS.2006.872327>,
1200 2006.

1201 Livesey, N. J., Filipiak, M. J., Froidevaux, L., Read, W. G., Lambert, A., Santee, M. L., Jiang, J. H., Waters, J. W.,
1202 Cofield, R. E., Cuddy, D. T., Daffer, W. H., Drouin, B. J., Fuller, R. A., Jarnot, R. F., Jiang, Y. B., Knosp, B. W.,
1203 Li, Q. B., Perun, V. S., Schwartz, M. J., Snyder, W. V., Stek, P. C., Thurstans, R. P., Wagner, P. A., Pumphrey, H.
1204 C., Avery, M., Browell, E. V., Cammas, J.-P., Christensen, L. E., Edwards, D. P., Emmons, L. K., Gao, R.-S., Jost,
1205 H.-J., Loewenstein, M., Lopez, J. D., Nédélec, P., Osterman, G. B., Sachse, G. W., and Webster, C. R.: Validation
1206 of Aura Microwave Limb Sounder O₃ and CO observations in the upper troposphere and lower stratosphere, *J.*
1207 *Geophys. Res.*, 113, D15S02, <https://doi.org/10.1029/2007JD008805>, 2008.

1208 Livesey, N. J., Logan, J. A., Santee, M. L., Waters, J. W., Doherty, R. M., Read, W. G., Froidevaux, L., and Jiang, J.
1209 H.: Interrelated variations of O₃, CO and deep convection in the tropical/subtropical upper troposphere observed
1210 by the Aura Microwave Limb Sounder (MLS) during 2004-2011, *Atmos. Chem. Phys.*, 13, 579–598,
1211 <https://doi.org/10.5194/acp-13-579-2013>, 2013.

1212 Livesey, N. J., Read, W. G., Wagner, P. A., Froidevaux, L., Santee, M. L., Schwartz, M. J., Lambert, A., Millan Valle,
1213 L. F., Pumphrey, H. C., Manney, G. L., Fuller, R. A., Jarnot, R. F., Knosp, B. W., and Lay, R. R.: EOS MLS
1214 Version 5.0x Level 2 and 3 data quality and description document, Tech. rep., Jet Propulsion Laboratory D-105336
1215 Rev. B, Jan. 30, 2022, <https://mls.jpl.nasa.gov/eos-aura-mls/documentation.php>, 2022.

1216 Logan, Jennifer A.: Tropospheric ozone: Seasonal behavior, trends, and anthropogenic influence, *J. Geophys. Res.-*
1217 *Atmos.*, 90, 10463–10482, <https://doi.org/10.1029/JD090iD06p10463>, 1985.

1218 Logan, J. A., Prather, M. J., Wofsy, S. C., and McElroy, M. B.: Tropospheric chemistry: a global perspective, *J.*
1219 *Geophys. Res.*, 86, 7210–7254, <https://doi.org/10.1029/JC086iC08p07210>, 1981.

1220 Logan, J. A., Megretskaia, I., Nassar, R., Murray, L. T., Zhang, L., Bowman, K. W., Worden, H. M., and Luo, M.:
1221 Effects of the 2006 El Niño on tropospheric composition as revealed by data from the Tropospheric Emission
1222 Spectrometer (TES), *Geophys. Res. Lett.*, 35, L03816, <https://doi.org/10.1029/2007GL031698>, 2008.

1223 McDuffie, E. E., Smith, S. J., O'Rourke, P., Tibrewal, K., Venkataraman, C., Marais, E. A., Zheng, B., Crippa, M.,
1224 Brauer, M., and Martin, R. V.: A global anthropogenic emission inventory of atmospheric pollutants from sector-
1225 and fuel-specific sources (1970–2017): an application of the Community Emissions Data System (CEDS), *Earth*
1226 *Syst. Sci. Data*, 12, 3413–3442, <https://doi.org/10.5194/essd-12-3413-2020>, 2020.

1227 Meinshausen, M., Vogel, E., Nauels, A., Lorbacher, K., Meinshausen, N., Etheridge, D. M., Fraser, P. J., Montzka, S.
1228 A., Rayner, P. J., Trudinger, C. M., Krumme, P. B., Beyerle, U., Canadell, J. G., Daniel, J. S., Enting, I. G., Law,
1229 R. M., Lunder, C. R., O'Doherty, S., Prinn, R. G., Reimann, S., Rubino, M., Velders, G. J. M., Vollmer, M. K.,
1230 Wang, R. H.-J., and Weiss, R.: Historical greenhouse gas concentrations for climate modelling (CMIP6),
1231 *Geoscientific Model Development*, 10(5), 2057–2116. <https://doi.org/10.5194/gmd-10-2057-2017>, 2017.

1232 Meinshausen, M., Nicholls, Z. R. J., Lewis, J., Gidden, M. J., Vogel, E., Freund, M., Beyerle, U., Gessner, C., Nauels,
1233 A., Bauer, N., Canadell, J. G., Daniel, J. S., John, A., Krummel, P. B., Luderer, G., Meinshausen, N., Montzka, S.
1234 A., Rayner, P. J., Reimann, S., Smith, S. J., van den Berg, M., Velders, G. J. M., Vollmer, M. K., and Wang, R.
1235 H. J.: The shared socio-economic pathway (SSP) greenhouse gas concentrations and their extensions to 2500,
1236 *Geosci. Model Dev.*, 13, 3571–3605, <https://doi.org/10.5194/gmd-13-3571-2020>, 2020.

1237 Meul, S., Langematz, U., Kröger, P., Oberländer-Hayn, S., and Jöckel, P.: Future changes in the stratosphere-to-
1238 troposphere ozone mass flux and the contribution from climate change and ozone recovery, *Atmos. Chem. Phys.*,
1239 18, 7721–7738, <https://doi.org/10.5194/acp-18-7721-2018>, 2018.

1240 Miyazaki, K., Bowman, K., Sekiya, T., Takigawa, M., Neu, J. L., Sudo, K., Osterman, G., and Eskes, H.: Global
1241 tropospheric ozone responses to reduced NO_x emissions linked to the COVID-19 worldwide lockdowns, *Science*
1242 *Advances*, 7(24), eabf7460, <https://doi.org/10.1126/sciadv.abf7460>, 2021.

1243 Monks, P. S., Archibald, A. T., Colette, A., Cooper, O., Coyle, M., Derwent, R., Fowler, D., Granier, C., Law, K. S.,
1244 Mills, G. E., Stevenson, D. S., Tarasova, O., Thouret, V., von Schneidmesser, E., Sommariva, R., Wild, O., and
1245 Williams, M. L.: Tropospheric ozone and its precursors from the urban to the global scale from air quality to short-
1246 lived climate forcer, *Atmos. Chem. Phys.*, 15, 8889–8973, <https://doi.org/10.5194/acp-15-8889-2015>, 2015.

1247 Montzka, S. A., Krol, M., Dlugokencky, E., Hall, B., Jöckel, P., and Lelieveld, J.: Small Interannual Variability of
1248 Global Atmospheric Hydroxyl, *Science*, 331, 67–69, <https://doi.org/10.1126/science.1197640>, 2011.

1249 Murray, L. T., Mickley, L. J., Kaplan, J. O., Sofen, E. D., Pfeiffer, M., and Alexander, B.: Factors controlling
1250 variability in the oxidative capacity of the troposphere since the Last Glacial Maximum, *Atmos. Chem. Phys.*, 14,
1251 3589–3622, <https://doi.org/10.5194/acp-14-3589-2014>, 2014.

1252 Nassar, R., Logan, J. A., Megretskaia, I. A., Murray, L. T., Zhang, L., & Jones, D. B. A., Analysis of tropical
1253 tropospheric ozone, carbon monoxide, and water vapor during the 2006 El Niño using TES observations and the
1254 GEOS-Chem model, *J. Geophys. Res.-Atmos.*, 114, D17304, <https://doi.org/10.1029/2009jd011760>, 2009.

1255 Neely, R. R., and Schmidt, A.: VolcanEESM: Global volcanic sulphur dioxide (SO₂) emissions database from 1850
1256 to present - Version 1.0., <https://doi.org/10.5285/76ebdc0b-0eed-4f70-b89e-55e606bcd568>, 2016.

1257 Neu, J. L., Flury, T., Manney, G. L., Santee, M. L., Livesey, N. J., and Worden, J.: Tropospheric ozone variations
1258 governed by changes in stratospheric circulation, *Nat. Geosci.*, 7, 340–344, <https://doi.org/10.1038/ngeo2138>,
1259 2014.

1260 O'Neill, B. C., Tebaldi, C., van Vuuren, D. P., Eyring, V., Friedlingstein, P., Hurtt, G., Knutti, R., Kriegler, E.,
1261 Lamarque, J.-F., Lowe, J., Meehl, G. A., Moss, R., Riahi, K., and Sanderson, B. M.: The Scenario Model
1262 Intercomparison Project (Scenario MIP) for CMIP6, *Geosci. Model Dev.*, 9, 3461–3482,
1263 <https://doi.org/10.5194/gmd-9-3461-2016>, 2016.

1264 Oman, L. D., Ziemke, J. R., Douglass, A. R., Waugh, D. W., Lang, C., Rodriguez, J. M., and Nielsen, J. E.: The
1265 response of tropical tropospheric ozone to ENSO, *Geophys. Res. Lett.*, 38, L13706,
1266 <https://doi.org/10.1029/2011gl047865>, 2011.

1267 Oman, L. D., Douglass, A. R., Ziemke, J. R., Rodriguez, J. M., Waugh, D. W., and Nielsen, J. E.: The ozone response
1268 to ENSO in Aura satellite measurements and a chemistry-climate simulation, *J. Geophys. Res.*, 118, 965–976,
1269 <https://doi.org/10.1029/2012jd018546>, 2013.

1270 Park, M., Randel, W. J., Kinnison, D. E., Emmons, L. K., Bernath, P. F., and Walker, K. A., Boone, C. D., and Livesey,
1271 N. J.: Hydrocarbons in the upper troposphere and lower stratosphere observed from ACE-FTS and comparisons
1272 with WACCM, *J. Geophys. Res.-Atmos.*, 118, 1964–1980, <https://doi.org/10.1029/2012JD018327>, 2013.

1273 Park, K., Wang, Z., Emmons, L. K., and Mak, J. E.: Variation of atmospheric CO, $\delta^{13}\text{C}$, and $\delta^{18}\text{O}$ at high northern
1274 latitude during 2004–2009: Observations and model simulations, *J. Geophys. Res.-Atmos.*, 120, 11,024–11,036,
1275 <https://doi.org/10.1002/2015JD023191>, 2015.

1276 Park, M., Worden, H. M., Kinnison, D. E., Gaubert, B., Tilmes, S., Emmons, L. K., Santee, M. L., Froidevaux, L.,
1277 and Boone, C. D.: Fate of pollution emitted during the 2015 Indonesian fire season, *J. Geophys. Res.-Atmos.*, 126,
1278 e2020JD033474, <https://doi.org/10.1029/2020JD033474>, 2021.

1279 Patel, A., Mallika, C., Chandrab, N., Patrab, P. K., Steinbacher, M., Revisiting regional and seasonal variations in
1280 decadal carbon monoxide variability: Global reversal of growth rate, *Science of the Total Environment*, 909,
1281 168476, <https://doi.org/10.1016/j.scitotenv.2023.168476>, 2024.

1282 Petzold, A., Thouret, V., Gerbig, C., Zahn, A., Brenninkmeijer, C. A. M., Gallagher, M., Hermann, M., Pontaud, M.,
1283 Ziereis, H., Boulanger, D., Marshall, J., Nédélec, P., Smit, H. G. J., Friess, U., Flaud, J.-M., Wahner, A., Cammas,
1284 J.-P., and Volz-Thomas, A.: Global-scale atmosphere monitoring by in-service aircraft – current achievements and
1285 future prospects of the European Research Infrastructure IAGOS, *Tellus B*, 67, 28452,
1286 <https://doi.org/10.3402/tellusb.v67.28452>, 2015.

1287 Price, C., and Rind, D.: A simple lightning parameterization for calculating global lightning distributions, *J. Geophys.*
1288 *Res.-Atmos.*, 97, 9919–9933, <https://doi.org/10.1029/92JD00719>, 1992.

1289 Price, C., Penner, J., and Prather, M.: NO_x from lightning: 1. Global distribution based on lightning physics, *J.*
1290 *Geophys. Res.-Atmos.*, 102(D5), 5929–5941. <https://doi.org/10.1029/96JD03504>, 1997.

1291 Randel, W. J., Park, M., Wu, F., and Livesey, N. J.: A large annual cycle in ozone above the tropical tropopause linked
1292 to the Brewer-Dobson circulation, *J. Atmos. Sci.*, 64, 4479–4488, <https://doi.org/10.1175/2007JAS2409.1>, 2007.

1293 Read, W. G., Shippony, Z., and Snyder, W. V.: The clear-sky unpolarized forward model for the EOS Aura microwave
1294 limb sounder (MLS), *IEEE Trans. Geosci. Remote Sens.*, 44, 1367–1379,
1295 <https://doi.org/10.1109/TGRS.2006.862267>, 2006.

1296 Riahi, K., van Vuuren, D. P., Kriegler, E., Edmonds, J., O'Neill, B. C., Fujimori, S., Bauer, N., Calvin, K., Dellink,
1297 R., Fricko, O., Lutz, W., Popp, A., Crespo Cuaresma, J., Samir, K. C., Leimbach, M., Jiang, L., Kram, T., Rao, S.,
1298 Emmerling, J., Ebi, K., Hasegawa, T., Havlik, P., Humpenöder, F., Da Silva, A., Smith, S., Stehfest, E., Bosetti,
1299 V., Eom, J., Gernaat, D., Masui, T., Rogelj, J., Strefler, J., Drouet, L., Krey, V., Luderer, G., Harmsen, M.,
1300 Takahashi, K., Baumstark, L., Doelman, J. C., Kainuma, M., Klimont, Z., Marangoni, G., Lotze-Campen, H.,
1301 Obersteiner, M., Tabeau, A., Tavoni, M.: The Shared Socioeconomic Pathways and their energy, land use, and
1302 greenhouse gas emissions implications: An overview, *Global Environ. Chang.*, 42, 1045–1068,
1303 <https://doi.org/10.1016/j.gloenvcha.2016.05.009>, 2017.

1304 Rodgers, C.: *Inverse Methods for Atmospheric Sounding: Theory and Practice*, Vol. 2 of Series on Atmospheric,
1305 Oceanic and Planetary Physics, World Scientific, Singapore, 2000.

1306 Rowlinson, M. J., Rap, A., Arnold, S. R., Pope, R. J., Chipperfield, M. P., McNorton, J., Forster, P., Gordon, H.,
1307 Pringle, K. J., Feng, W., Kerridge, B. J., Latter, B. L., and Siddans, R.: Impact of El Niño–Southern Oscillation on
1308 the interannual variability of methane and tropospheric ozone, *Atmos. Chem. Phys.*, 19, 8669–8686,
1309 <https://doi.org/10.5194/acp-19-8669-2019>, 2019.

1310 Schoeberl, M. R., Duncan, B. N., Douglass, A. R., Waters, J., Livesey, N., Read, W., and Filipiak, M.: The carbon
1311 monoxide tape recorder, *Geophys. Res. Lett.*, 33, L12811, <https://doi.org/10.1029/2006gl026178>, 2006.

1312 Schumann, U., and Huntrieser, H.: The global lightning-induced nitrogen oxides source, *Atmos. Chem. Phys.*, 7,
1313 3823–3907, <https://doi.org/10.5194/acp-7-3823-2007>, 2007.

1314 Soulié, A., Granier, C., Darras, S., Zilbermann, N., Doumbia, T., Guevara, M., Jalkanen, J.-P., Keita, S., Liousse, C.,
1315 Crippa, M., Guizzardi, D., Hoesly, R., and Smith, S. J.: Global anthropogenic emissions (CAM5-GLOB-ANT) for
1316 the Copernicus Atmosphere Monitoring Service simulations of air quality forecasts and reanalyses, *Earth Syst.
1317 Sci. Data*, 16, 2261–2279, <https://doi.org/10.5194/essd-16-2261-2024>, 2024.

1318 Souri, A. H., Choi, Y., Jeon, W., Woo, J.-H., Zhang, Q., and Kurokawa, J.: Remote sensing evidence of decadal
1319 changes in major tropospheric ozone precursors over East Asia, *J. Geophys. Res.-Atmos.*, 122, 2474–2492,
1320 <https://doi.org/10.1002/2016JD025663>, 2017.

1321 SPARC: The SPARC Data Initiative: Assessment of stratospheric trace gas and aerosol climatologies from satellite
1322 limb sounders, M. I. Hegglin and S. Tegtmeier (eds.), SPARC Report No. 8, WCRP-5/2017, available at
1323 www.sparc-climate.org/publications/sparc-reports/, 2017.

1324 Stein, O., M. G. Schultz, M. G., Bouarar, I., Clark, H., Huijnen, V., A. Gaudel, A., George, M., and Clerbaux, C.: On
1325 the wintertime low bias of Northern Hemisphere carbon monoxide found in global model simulations, *Atmos.
1326 Chem. Phys.*, 14, 9295–9316, <https://doi.org/10.5194/acp-14-9295-2014>, 2014.

1327 Steinbrecht, W., Kubistin, D., Plass-Dülmer, C., Davies, J., Tarasick, D. W., Gathen, P. v. d., Deckelmann, H., Jepsen,
1328 N., Kivi, R., Lyall, N., Palm, M., Notholt, J., Kois, B., Oelsner, P., Allaart, M., Piters, A., Gill, M., Van Malderen,
1329 R., Delcloo, A. W., Sussmann, R., Mahieu, E., Servais, C., Romanens, G., Stübi, R., Ancellet, G., Godin-

1330 Beekmann, S., Yamanouchi, S., Strong, K., Johnson, B., Cullis, P., Petropavlovskikh, I., Hannigan, J. W.,
1331 Hernandez, J.-L., Diaz Rodriguez, A., Nakano, T., Chouza, F., Leblanc, T., Torres, C., Garcia, O., Röhling, A. N.,
1332 Schneider, M., Blumenstock, T., Tully, M., Paton-Walsh, C., Jones, N., Querel, R., Strahan, S., Stauffer, R. M.,
1333 Thompson, A. M., Inness, A., Engelen, R., Chang, K.-L., and Cooper, O. R.: COVID-19 Crisis Reduces Free
1334 Tropospheric Ozone Across the Northern Hemisphere, *Geophys. Res. Lett.*, 48, e2020GL091987,
1335 <https://doi.org/10.1029/2020GL091987>, 2021.

1336 Stevenson, D. S., Young, P. J., Naik, V., Lamarque, J.-F., Shindell, D. T., Voulgarakis, A., Skeie, R. B., Dalsoren, S.
1337 B., Myhre, G., Berntsen, T. K., Folberth, G. A., Rumbold, S. T., Collins, W. J., MacKenzie, I. A., Doherty, R. M.,
1338 Zeng, G., van Noije, T. P. C., Strunk, A., Bergmann, D., Cameron-Smith, P., Plummer, D. A., Strode, S. A.,
1339 Horowitz, L., Lee, Y. H., Szopa, S., Sudo, K., Nagashima, T., Josse, B., Cionni, I., Righi, M., Eyring, V., Conley,
1340 A., Bowman, K. W., Wild, O., and Archibald, A.: Tropospheric ozone changes, radiative forcing and attribution
1341 to emissions in the Atmospheric Chemistry and Climate Model Intercomparison Project (ACCMIP), *Atmos.*
1342 *Chem. Phys.*, 13, 3063–3085, <https://doi.org/10.5194/acp-13-3063-2013>, 2013.

1343 Strode, S. A., Worden, H. M., Damon, M., Douglass, A. R., Duncan, B. N., Emmons, L. K., Lamarque, J.-F., Manyin,
1344 M., Oman, L. D., Rodriguez, J. M., Strahan, S. E., and Tilmes, S.: Interpreting space-based trends in carbon
1345 monoxide with multiple models, *Atmos. Chem. Phys.*, 16, 7285–7294, <https://doi.org/10.5194/acp-16-7285-2016>,
1346 2016.

1347 Sudo, K. and Takahashi, M.: Simulation of tropospheric ozone changes during 1997–1998 El Niño: Meteorological
1348 impact on tropospheric photochemistry, *Geophys. Res. Lett.*, 28, 4091–4094,
1349 <https://doi.org/10.1029/2001GL013335>, 2001.

1350 Sudo, K., Takahashi, M., and Akimoto, H.: Future changes in stratosphere-troposphere exchange and their impacts on
1351 future tropospheric ozone simulations, *Geophys. Res. Lett.*, 30, 24, 2256, <https://doi.org/10.1029/2003GL018526>
1352 , 2003.

1353 Tapping, K.F.: The 10.7 cm solar radio flux (F10.7), *Space Weather*, 11, 394–406, <https://doi.org/10.1002/swe.20064>,
1354 2013.

1355 Thompson, A. M., Doddridge, B. G., Witte, J. C., Hudson, R. D., Luke, W. T., Johnson, J. E., Johnson, B. J., Oltmans,
1356 S. J., and Weller, R.: A tropical Atlantic ozone paradox: Shipboard and satellite views of a tropospheric ozone
1357 maximum and wave-one in January–February 1999, *Geophys. Res. Lett.*, 27, 3317–3320,
1358 <https://doi.org/10.1029/1999GL011273>, 2000.

1359 Thompson, A. M., Witte, J. C., Oltmans, S. J., Schmidlin, F. J., Logan, J. A., Fujiwara, M., Kirchhoff, V. W. J., Posny,
1360 F., Coetzee, G. J. R., Hoegger, B., Kawakami, S., Ogawa, T., Fortuin, J. P. F., and Kelder, H. M.: Southern
1361 Hemisphere Additional Ozonesondes (SHADOZ) 1998–2000 tropical ozone climatology. 2. Tropospheric
1362 variability and the zonal wave-one, *J. Geophys. Res.-Atmos.*, 108(D2), 8241,
1363 <https://doi.org/10.1029/2002JD002241>, 2003.

1364 Thompson, A. M., Stauffer, R. M., Wargan, K., Witte, J. C., Kollonige, D. E., and Ziemke, J. R.: Regional and
1365 seasonal trends in tropical ozone from SHADOZ profiles: Reference for models and satellite products, *J. Geophys.*
1366 *Res.-Atmos.*, 126, e2021JD034691, <https://doi.org/10.1029/2021JD034691>, 2021.

1367 Tilmes, S., Hodzic, A., Emmons, L. K., Mills, M. J., Gettelman, A., Kinnison, D. E., Park, M., Lamarque, J.-F., Vitt,
1368 F., Shrivastava, M., Campuzano-Jost, P., Jimenez, J. L., and Liu, X.: Climate forcing and trends of organic
1369 aerosols in the Community Earth System Model (CESM2), *J. of Adv. in Modeling Earth Systems*, 11, 4323–4351,
1370 <https://doi.org/10.1029/2019MS001827>, 2019.

1371 Tsvilidou, M., Sauvage, B., Bennouna, Y., Blot, R., Boulanger, D., Clark, H., Le Flochmoën, E., Nédélec, P., Valérie
1372 Thouret, V., Wolff, P., and Barret, B.: Tropical tropospheric ozone and carbon monoxide distributions:
1373 characteristics, origins, and control factors, as seen by IAGOS and IASI, *Atmos. Chem. Phys.*, 23, 14039–14063,
1374 <https://doi.org/10.5194/acp-23-14039-2023>, 2023.

1375 Verma, S., Yadava, P. K., Lal, D. M., Mall, R. K., Kumar, H., and Payra, S.: Role of Lightning NO_x in Ozone
1376 Formation: A Review, *Pure Appl. Geophys.*, <https://doi.org/10.1007/s00024-021-02710-5>, 2021.

1377 Voulgarakis, A., Marlier, M. E., Faluvegi, G., Shindell, D. T., Tsigaridis, K., and Mangeon, S.: Interannual variability
1378 of tropospheric trace gases and aerosols: The role of biomass burning emissions, *J. Geophys. Res.-Atmos.*, 120,
1379 7157–7173, <https://doi.org/10.1002/2014JD022926>, 2015.

1380 Wang, P.-H., Fishman, J., Harvey, V. L., and Hitchman, M. H.: Southern tropical upper tropospheric zonal ozone
1381 wave-1 from SAGE II observations (1985–2002), *J. Geophys. Res.-Atmos.*, 111, D08305,
1382 <https://doi.org/10.1029/2005JD006221>, 2006.

1383 Wang, H., Lu, X., Jacob, D. J., Cooper, O. R., Chang, K.-L., Li, K., Gao, M., Liu, Y., Sheng, B., Wu, K., Wu, T.,
1384 Zhang, J., Sauvage, B., Nédélec, P., Blot, R., and Fan, S.: Global tropospheric ozone trends, attributions, and
1385 radiative impacts in 1995–2017: an integrated analysis using aircraft (IAGOS) observations, ozonesonde, and
1386 multi-decadal chemical model simulations, *Atmos. Chem. Phys.*, 22, 13753–13782, <https://doi.org/10.5194/acp-22-13753-2022>, 2022.

1388 Warner, J., Carminati, F., Wei, Z., Lahoz, W., and Attié, J.-L.: Tropospheric carbon monoxide variability from AIRS
1389 under clear and cloudy conditions, *Atmos. Chem. Phys.*, 13, 12469–12479, <https://doi.org/10.5194/acp-13-12469-2013>, 2013.

1391 Waters, J., Froidevaux, L., Harwood, R., Jarnot, R., Pickett, H., Read, W., Siegel, P., Cofield, R., Filipiak, M., Flower,
1392 D., Holden, J., Lau, G., Livesey, N., Manney, G., Pumphrey, H., Santee, M., Wu, D., Cuddy, D., Lay, R., Loo, M.,
1393 Perun, V., Schwartz, M., Stek, P., Thurstans, R., Boyles, M., Chandra, S., Chavez, M., Chen, G.-S., Chudasama,
1394 B., Dodge, R., Fuller, R., Girard, M., Jiang, J., Jiang, Y., Knosp, B., LaBelle, R., Lam, J., Lee, K., Miller, D.,
1395 Oswald, J., Patel, N., Pukala, D., Quintero, O., Scaff, D., Snyder, V., Tope, M., Wagner, P., and Walch, M.: The
1396 Earth Observing System Microwave Limb Sounder (EOS MLS) on the Aura satellite, *IEEE Transac. Geosci.*
1397 *Remote Sens.*, 44, 5, <https://doi.org/10.1109/TGRS.2006.873771>, 2006.

1398 Witte, J. C., Schoeberl, M. R., Douglass, A. R., and Thompson, A. M.: The quasi-biennial oscillation in tropical ozone
1399 from SHADOZ and HALOE, *Atmos. Chem. Phys.*, 8, 3929–3936, <https://doi.org/10.5194/acp-8-3929-2008>, 2008.

1400 Wolter, K., and Timlin, M. S.: El Niño/Southern Oscillation behaviour since 1871 as diagnosed in an extended
1401 multivariate ENSO index (MEI.ext), *Intl. J. Climatology*, 31, 1074–1087, <https://doi.org/10.1002/joc.2336>, 2011.

1402 Worden, H. M., Deeter, M. N., Frankenberg, C., George, M., Nichitiu, F., Worden, J., Aben, I., Bowman, K. W.,
1403 Clerbaux, C., Coheur, P. F., de Laat, A. T. J., Detweiler, R., Drummond, J. R., Edwards, D. P., Gille, J. C.,

1404 Hurtmans, D., Luo, M., Martinez- Alonso, S., Massie, S., Pfister, G., and Warner, J. X.: Decadal record of satellite
1405 carbon monoxide observations, *Atmos. Chem. Phys.*, 13, 837–850, <https://doi.org/10.5194/acp-13-837-2013>,
1406 2013a.

1407 Worden, J., Wecht, K., Frankenberg, C., Alvarado, M., Bowman, K., Kort, E., Kulawik, S., Lee, M., Payne, V., and
1408 Worden, H.: CH₄ and CO distributions over tropical fires during October 2006 as observed by the Aura TES
1409 satellite instrument and modeled by GEOS-Chem, *Atmos. Chem. Phys.*, 13, 3679–3692,
1410 <https://doi.org/10.5194/acp-13-3679-2013>, 2013b.

1411 Yoon, J., and Pozzer, A.: Model-simulated trend of surface carbon monoxide for the 2001–2010 decade, *Atmos.*
1412 *Chem. Phys.*, 14, 10465–10482, <https://doi.org/10.5194/acp-14-10465-2014>, 2014.

1413 Zhang, L., Li, Q. B., Jin, J., Liu, H., Livesey, N., Jiang, J. H., Mao, Y., Chen, D., Luo, M., and Chen, Y.: Impacts of
1414 2006 Indonesian fires and dynamics on tropical upper tropospheric carbon monoxide and ozone, *Atmos. Chem.*
1415 *Phys.*, 11, 10929–10946, <https://doi.org/10.5194/acp-11-10929-2011>, 2011.

1416 Zhang, S., Zhao, P., He, L., Yang, Y., Liu, B., He, W., Cheng, Y., Liu, Y., Liu, S., Hu, Q., Huang, C., Wu, Y., On-
1417 board monitoring (OBM) for heavy-duty vehicle emissions in China: Regulations, early-stage evaluation and
1418 policy recommendations, *Science of the Total Environment*, Vol. 731, 139045, ISSN 0048-9697,
1419 <https://doi.org/10.1016/j.scitotenv.2020.139045>, 2020.

1420 Zhang, T., Hoell, A., Perlwitz, J., Eischeid, J., Murray, D., Hoerling, M., and Hamill, T.: Towards Probabilistic
1421 Multivariate ENSO Monitoring, *Geophys. Res. Lett.*, 46, <https://doi.org/10.1029/2019GL083946>, 2019.

1422 Zhang, Y., Cooper, O. R., Gaudel, A., Thompson, A. M., Nédélec, P., Ogino, S.-Y., and West, J. J.: Tropospheric
1423 ozone change from 1980 to 2010 dominated by equatorward redistribution of emissions, *Nat. Geosci.*, 9, 875–879,
1424 <https://doi.org/10.1038/ngeo2827>, 2016.

1425 Zheng, B., Chevallier, F., Ciais, P., Yin, Y., Deeter, M. N., Worden, H. M., Wang, Y., Zhang, Q., and He, K.: Rapid
1426 decline in carbon monoxide emissions and export from East Asia between years 2005 and 2016, *Environ. Res.*
1427 *Lett.*, 13, 044007, <https://doi.org/10.1088/1748-9326/aab2b3>, 2018.

1428 Ziemke, J. R., and Chandra, S.: La Niña and El Niño–induced variabilities of ozone in the tropical lower atmosphere
1429 during 1970–2001, *Geophys. Res. Lett.*, 30, 3, 1142, <https://doi.org/10.1029/2002GL016387>, 2003.

1430 Ziemke, J. R., Chandra, S., Oman, L. D., and Bhartia, P. K.: A new ENSO index derived from satellite measurements
1431 of column ozone, *Atmos. Chem. Phys.*, 10, 3711–3721, <https://doi.org/10.5194/acp-10-3711-2010>, 2010.

1432 Ziemke, J. R., A. R. Douglass, A. R., L. D. Oman, L. D., S. E. Strahan, S. E., and B. N. Duncan, B. N.: Tropospheric
1433 ozone variability in the tropics from ENSO to MJO and shorter timescales, *Atmos. Chem. Phys.*, 15, 8037–8049,
1434 <https://doi.org/10.5194/acp-15-8037-2015>, 2015.

1435 Ziemke, J. R., Oman, L. D., Strode, S. A., Douglass, A. R., Olsen, M. A., McPeters, R. D., Bhartia, P. K., Froidevaux,
1436 L., Labow, G. J., Witte, J. C., Thompson, A. M., Haffner, D. P., Kramarova, N. A., Frith, S. M., Huang, L.-K.,
1437 Jaross, G. R., Seftor, C. J., Deland, M. T., and Taylor, S. L.: Trends in global tropospheric ozone inferred from a
1438 composite record of TOMS/OMI/MLS/OMPS satellite measurements and the MERRA-2 GMI simulation, *Atmos.*
1439 *Chem. Phys.*, 19, 3257–3269, <https://doi.org/10.5194/acp-19-3257-2019>, 2019.

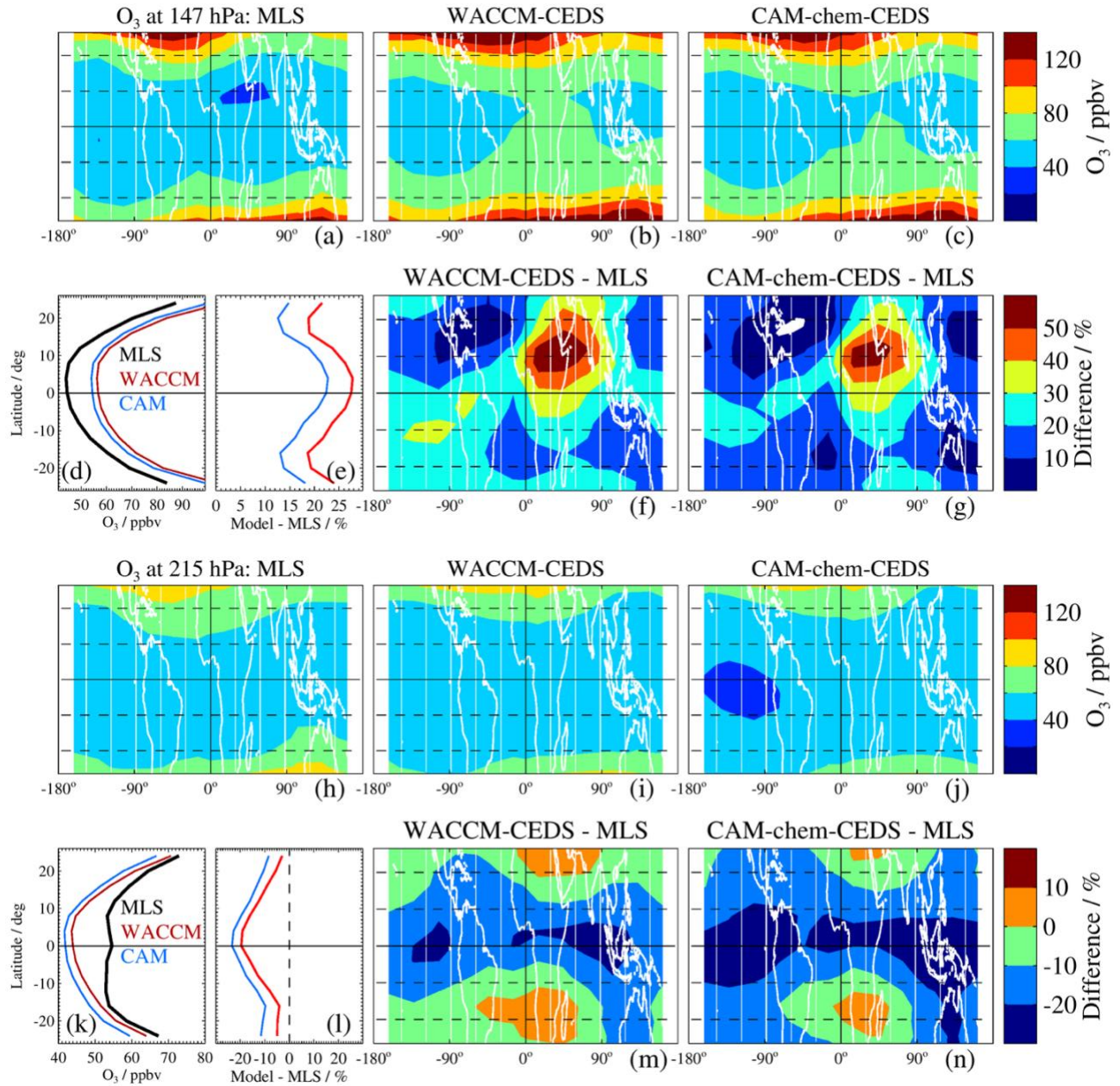
1440 Ziemke, J. R., Kramarova, N. A., Frith, S. M., Huang, L.-K., Haffner, D. P., and Wargan, K.: NASA satellite
1441 measurements show global-scale reductions in free tropospheric ozone in 2020 and again in 2021 during COVID-
1442 19, *Geophys. Res. Lett.*, 49, e2022GL098712, <https://doi.org/10.1029/2022GL098712>, 2022.
1443

1444 **Table 1.** Some characteristics of the three chemistry climate model simulations used in this work.
 1445

Model Designation	Simulation Name	CO Anthropogenic Emissions Dataset	CO Biomass Burning dataset	Nudging timescale (hours)	Tropical Lightning NO_x (Tg N yr⁻¹)	Aircraft NO_x Dataset¹
CAM-chem	CAM-chem-CAMS	CAMS-GLOB-ANT_v5.1	QFED	6	2.34	Soulié et al. (2024)
CAM-chem	CAM-chem-CEDS	CEDSv2	QFED	6	2.34	Soulié et al. (2024)
WACCM	WACCM-CEDS	CEDSv2	QFED	12	2.78	CMIP6

1446
 1447 ¹For 2005–2014, the aircraft NO_x emissions for WACCM-CEDS and both CAM-chem model simulations
 1448 are identical. From 2015 onward, the WACCM-CEDS emissions are kept constant.
 1449

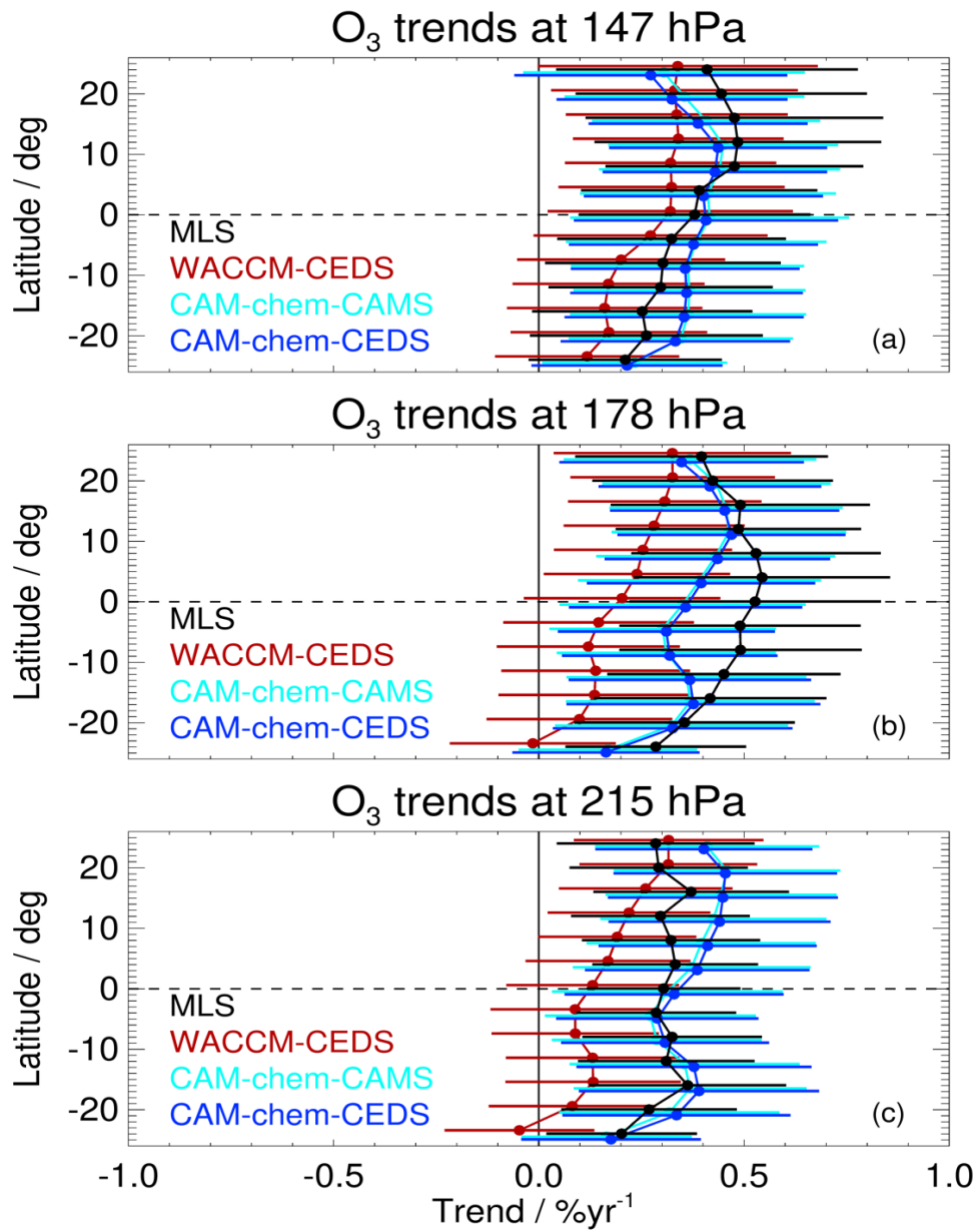
1450
 1451
 1452



1455
 1456
 1457
 1458
 1459
 1460
 1461
 1462
 1463
 1464
 1465

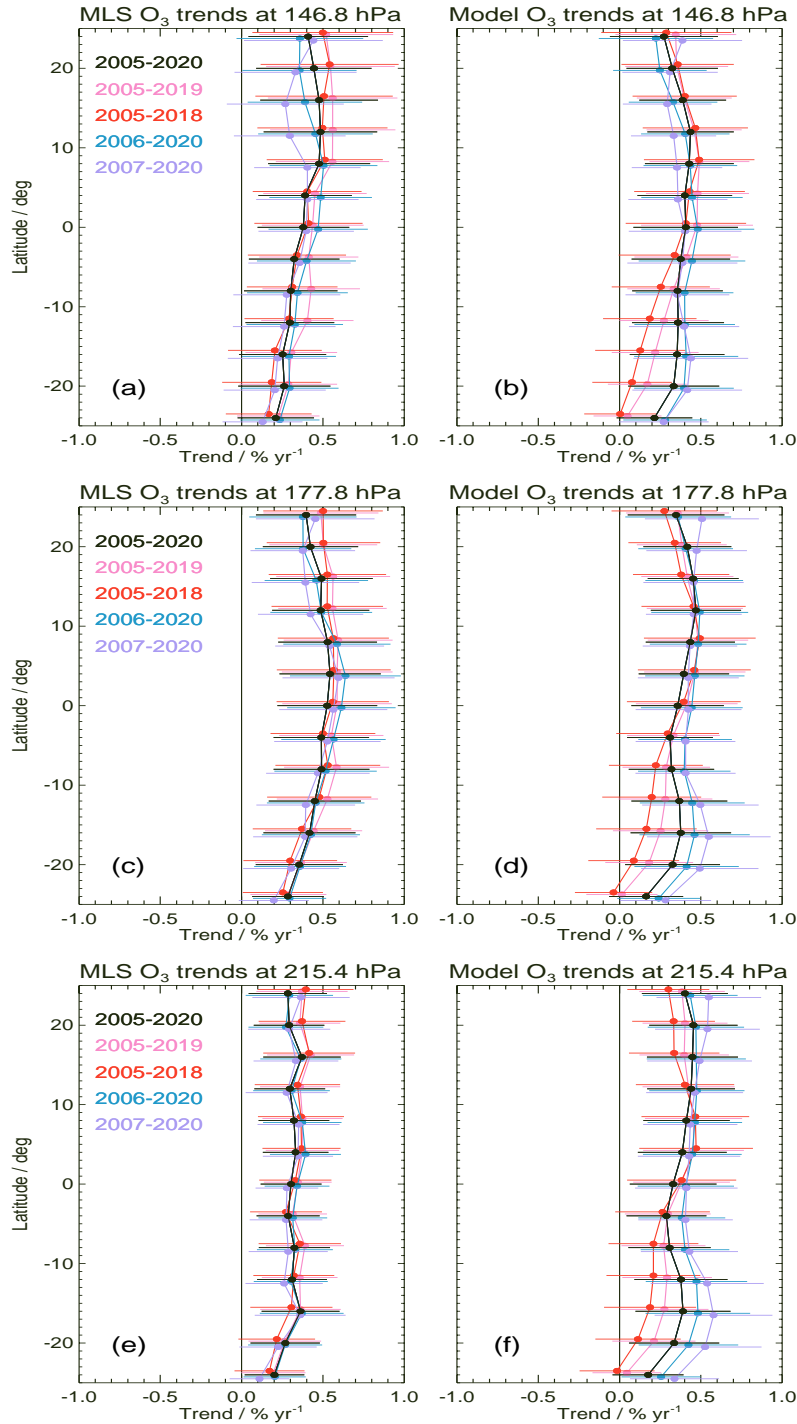
Figure 1. Annually-averaged climatological comparisons between MLS and model ozone fields for 2005-2020 at low latitudes (26°S to 26°N) at 147 hPa ((a) through (g)) and at 215 hPa ((h) through (n)). For 147 hPa: (a) climatological O₃ maps from MLS, (b) from WACCM-CEDS, (c) from CAM-chem-CEDS; (d) shows the zonal mean climatology from the MLS data and both model simulations, with (e) giving the differences in zonal means for both model simulations minus MLS (color-coded as shown in the (d) legend), while (f) provides a difference map of the climatologies from WACCM-CEDS minus MLS, and (g) gives the difference map for CAM-chem-CEDS minus MLS. Panels (h) through (n) provide the same information as (a) through (g), but for 215 hPa. We note that in panels (d) and (k), CAM is an abbreviation for the CAM-chem-CEDS simulation, and WACCM is an abbreviation for the WACCM-CEDS simulation.

1466
1467
1468



1469
1470
1471
1472
1473
1474
1475

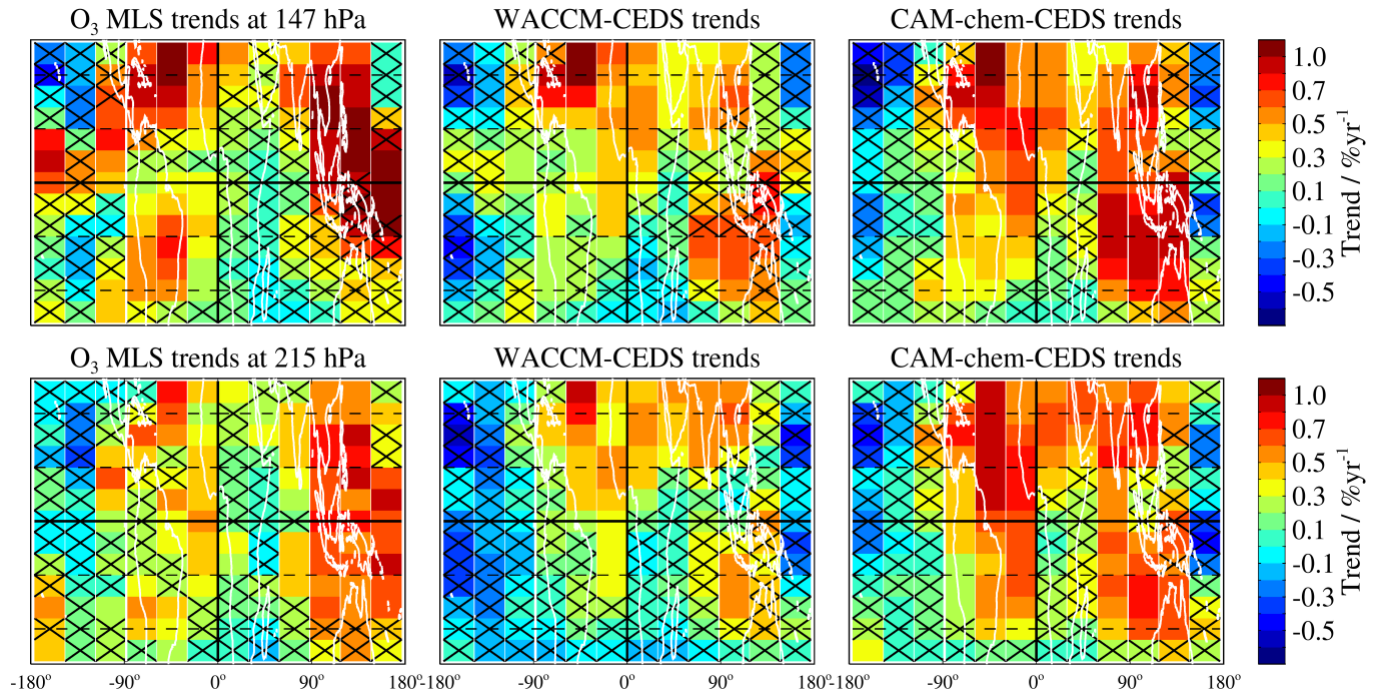
Figure 2. Ozone zonal mean trends versus latitude in the tropical upper troposphere, for 2005–2020, based on MLR analyses of time series from MLS (black), WACCM-CEDS (red), CAM-chem-CAMS (cyan) and CAM-chem-CEDS (blue). Each row corresponds to a different pressure level: (a) for 147 hPa, (b) for 178 hPa, and (c) for 215 hPa, as labeled above each panel. Error bars give the uncertainties (2σ) in the estimated linear trends (see text for more details).



1476
 1477
 1478
 1479
 1480
 1481
 1482
 1483
 1484
 1485

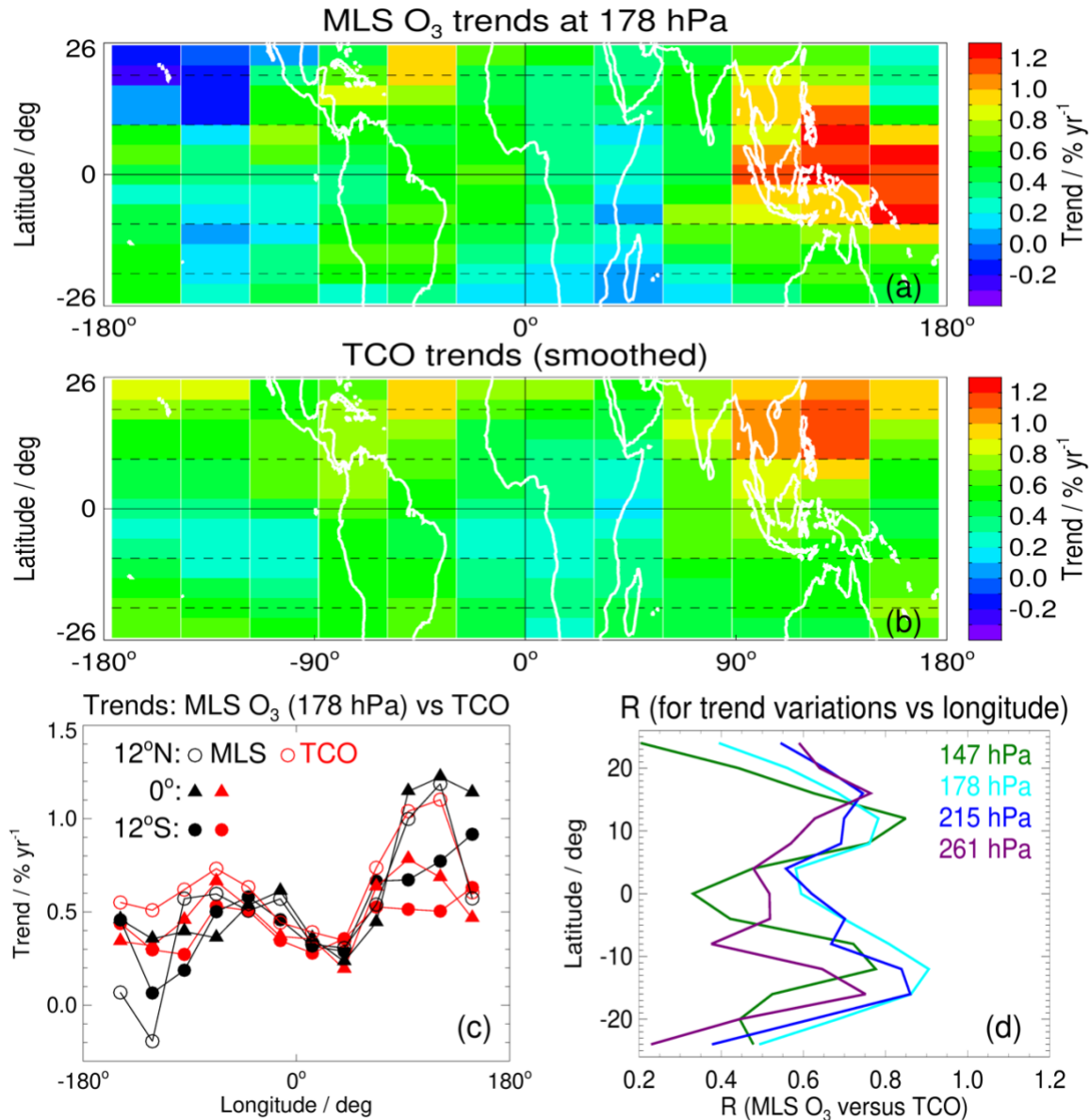
Figure 3. Ozone zonal mean trends versus latitude in the tropical upper troposphere, with results from MLS data analyses shown in the left panels, and model results from CAM-chem-CEDS in the right panels. Each row corresponds to a different pressure level, as labeled. All panels show the trend sensitivity to the time period used in the regression fits. For example, black is used to show the period from 2005 through 2020; results from four other time periods are also shown, with the start or end year shifted by one or two years (see legend for the meaning of the various colors). The error bars given here represent the (2σ) uncertainties in the estimated linear trends.

1486
1487



1488
1489
1490
1491
1492
1493
1494
1495

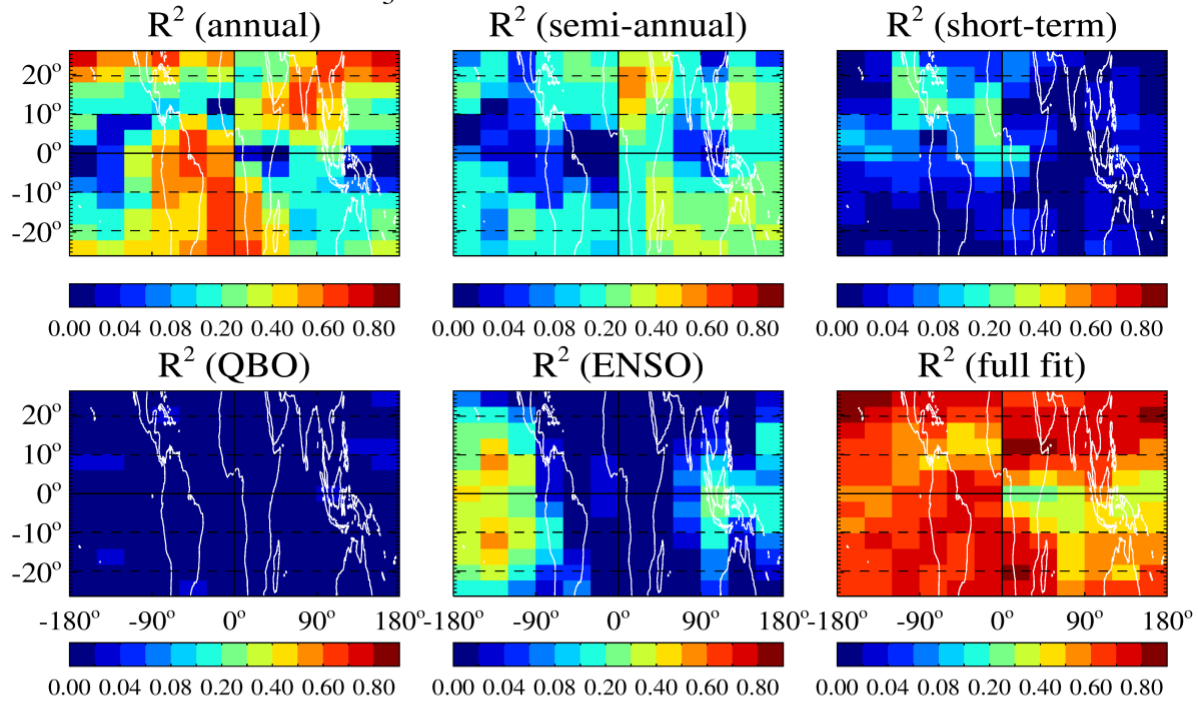
Figure 4. Maps of upper tropospheric O₃ trends (% yr⁻¹) in the tropics for 147 hPa (top row) and 215 hPa (bottom row); the latitude range is from 26°S to 26°N, with maps all centered on the Greenwich meridian. MLS trends (left column) are compared to trends from WACCM-CEDS (middle column) and CAM-chem-CEDS (right column). Black crosses show grid boxes for which the trend estimate is not significantly different from zero (based on our 2σ error estimates).



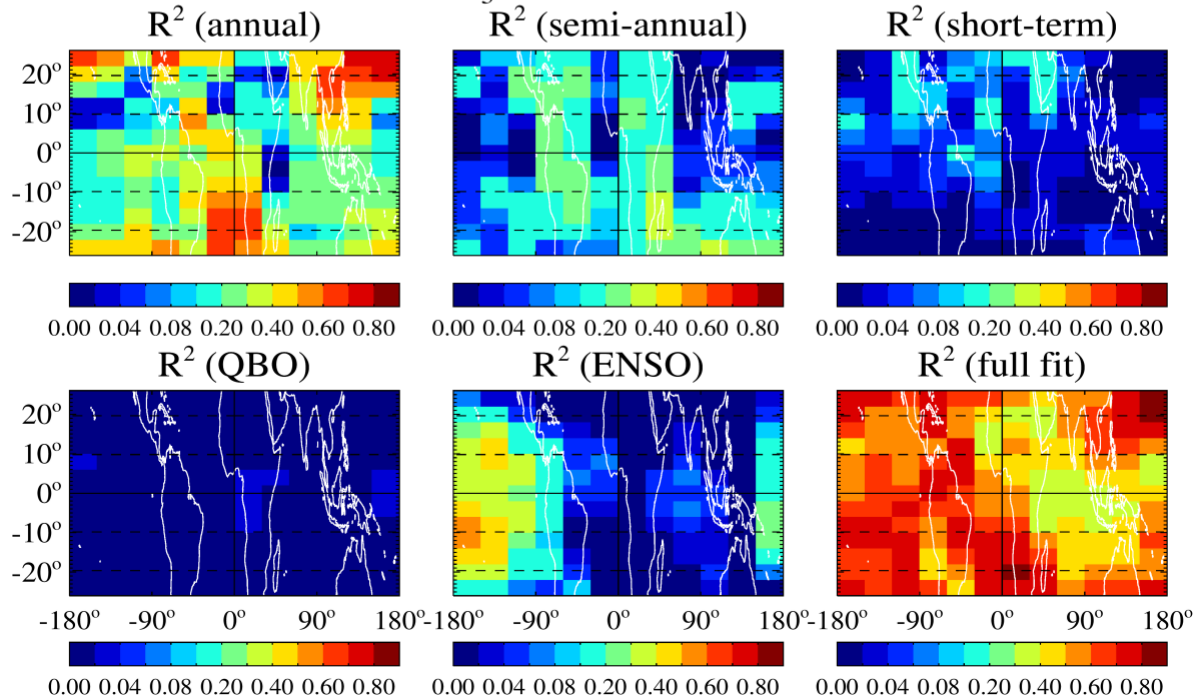
1496
 1497
 1498
 1499
 1500
 1501
 1502
 1503
 1504
 1505
 1506

Figure 5. (a) The top map shows MLS ozone trends (2005–2020) at 178 hPa, (b) the bottom map displays horizontally-smoothed tropospheric column ozone trends for the same time period, following the analyses of Ziemke et al. (2019), (c) cross sections of the above mapped trends in 4°-wide latitude bins centered at 12°N, 0°, and 12°S (see legend) for MLS (black) and TCO (red), and (d) correlation coefficient values R (on the x axis) between the MLS ozone trends at different pressures (see legend) and the TCO trends as a function of longitude, at different tropical latitudes (y axis). This panel provides a broader picture of the trend correlations, which exhibit a minimum near the Equator and maxima near 12°S and 12°N.

MLS O₃: Variance Contributions at 147 hPa



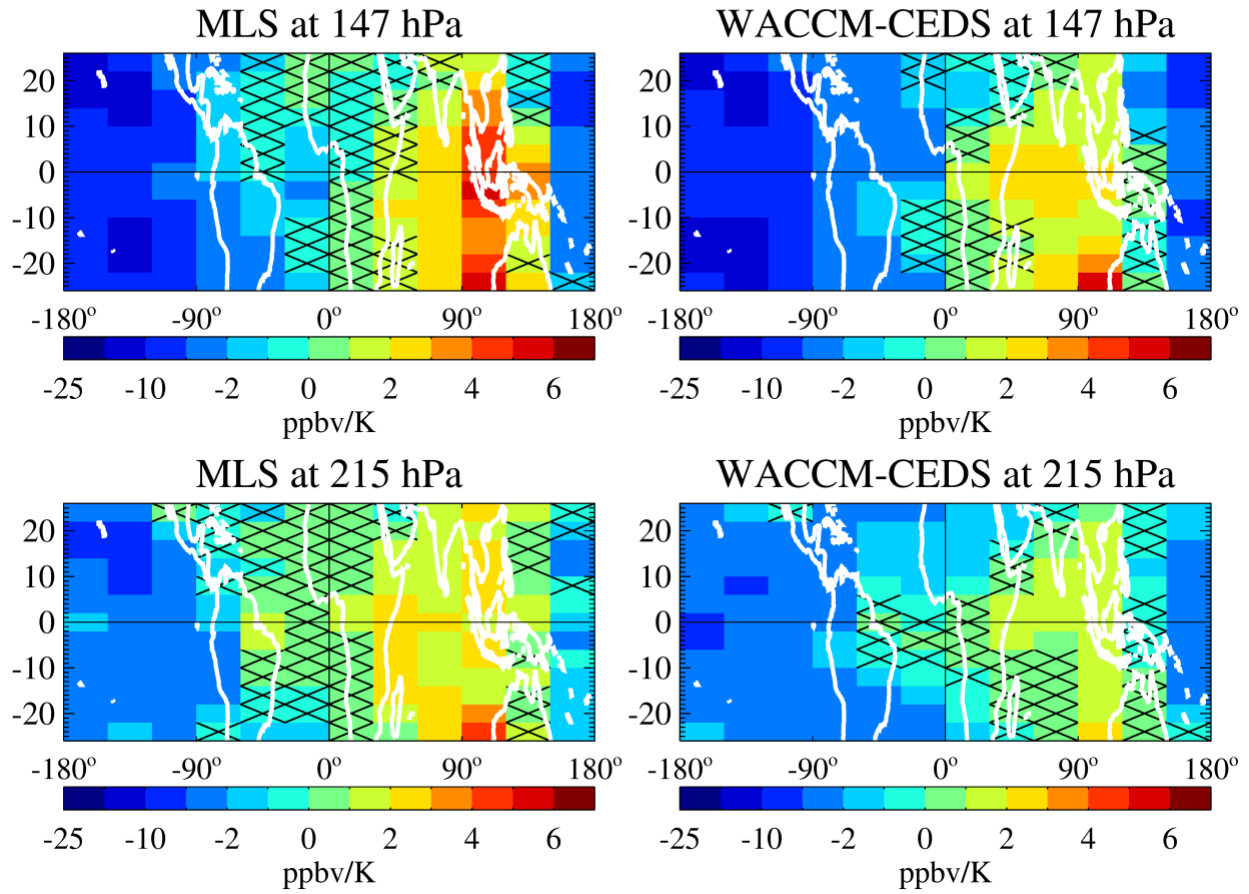
WACCM-CEDS O₃: Variance Contributions at 147 hPa



1507
1508
1509
1510
1511
1512
1513

Figure 6. Contributions to the time series variance from the main fitted components of the regression to the gridded tropical MLS ozone time series at 147 hPa (top 6 panels) and the same for the WACCM-CEDS time series (bottom 6 panels). The titles in each panel indicate that the explained variance is from specific components (annual, semi-annual, short-term, meaning 3- and 4-months, QBO, ENSO, and full fit).

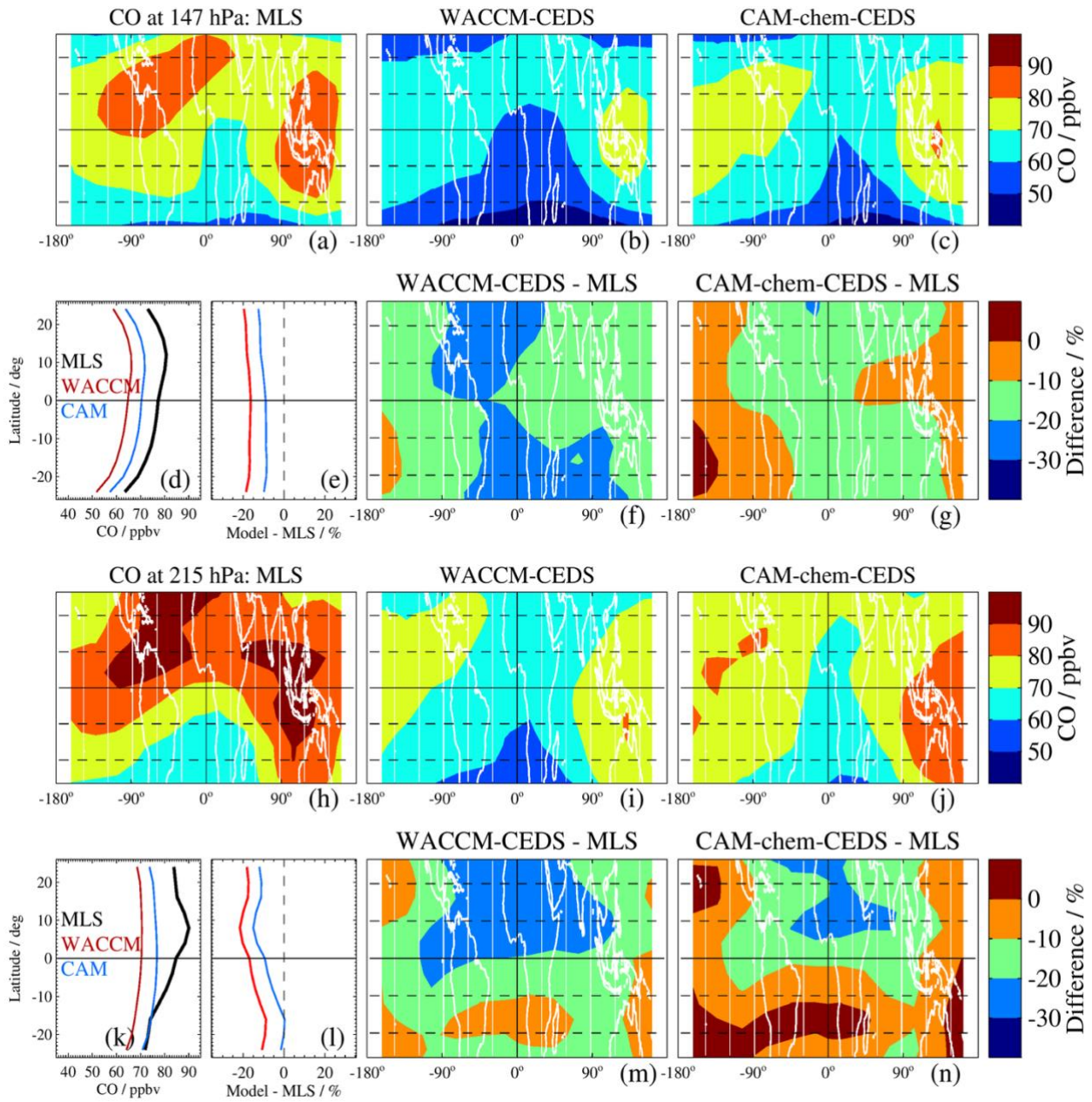
O₃: sensitivity coefficient to ENSO



1514
1515
1516
1517
1518
1519
1520
1521

Figure 7. Sensitivity coefficient to ENSO for ozone at 147 hPa (top panels) and 215 hPa (bottom panels); MLS results are shown in the left panels and the WACCM-CEDS results in the right panels. The black crosses show the grid boxes for which the sensitivity is not significantly different from zero (based on the 2σ error estimates). Note that this color bar is assymmetric, with much larger negative values than positive values.

1522
1523



1524
1525
1526
1527
1528
1529
1530
1531
1532
1533

Figure 8. Same as Fig. 1, but for CO.

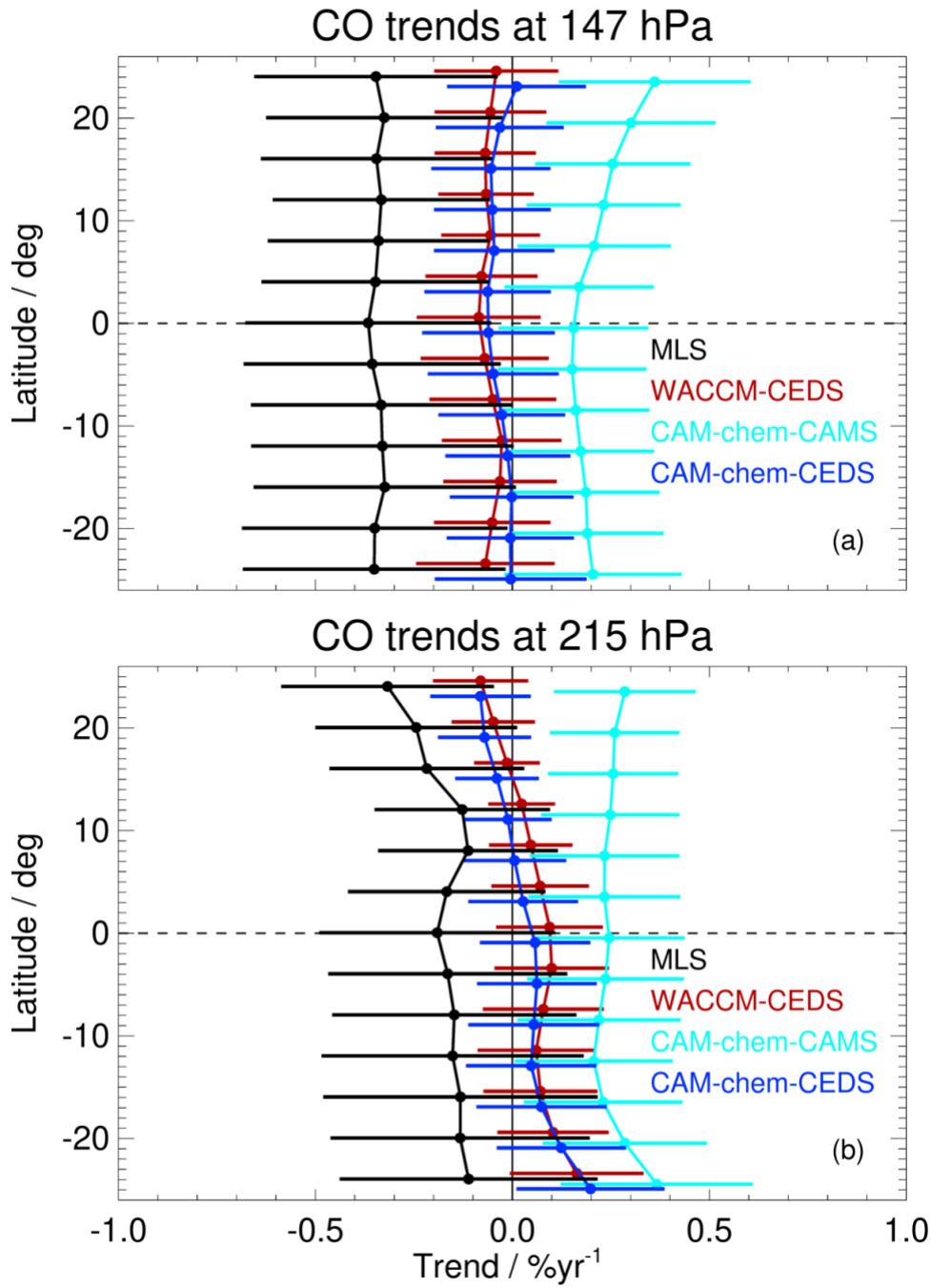
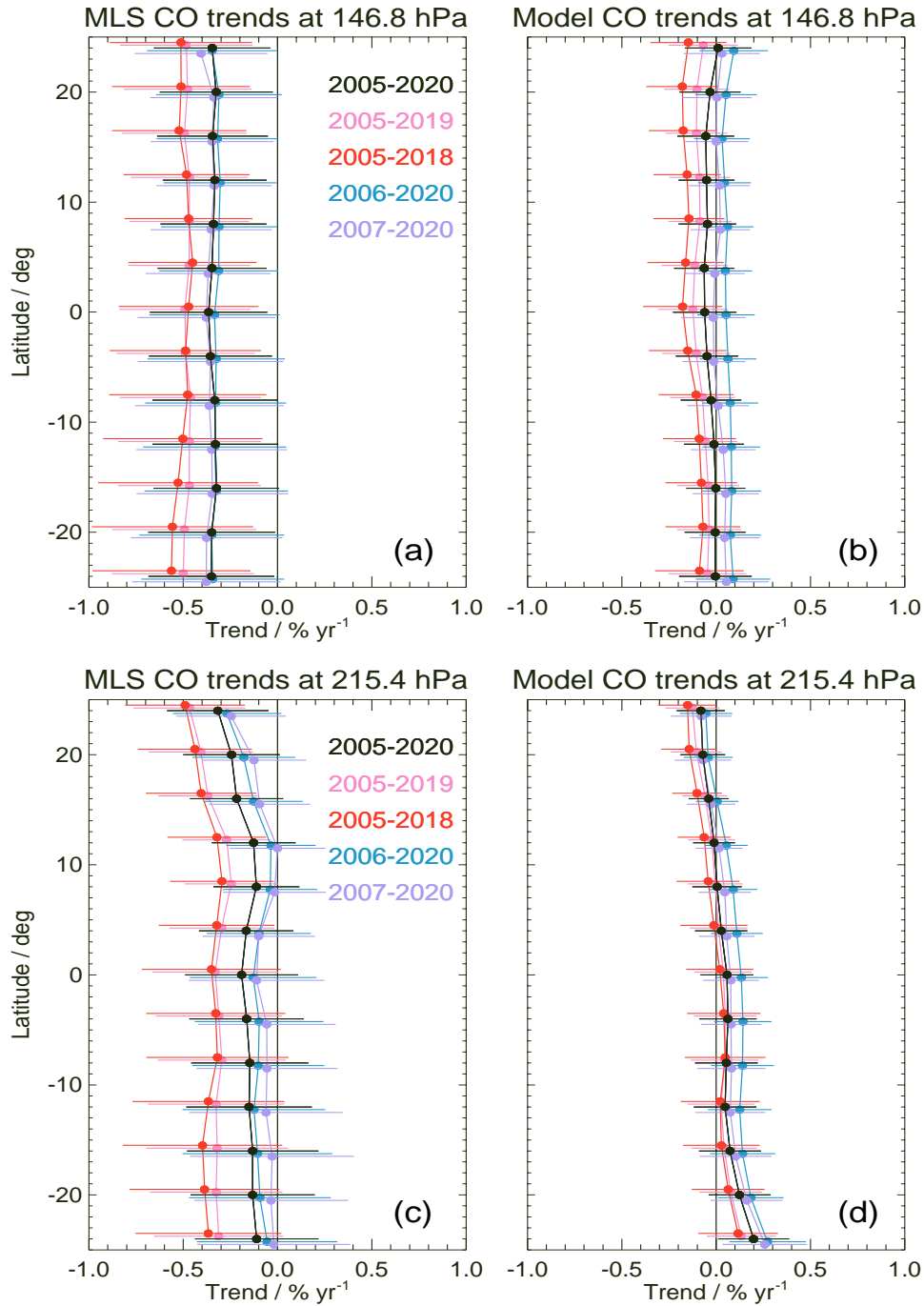


Figure 9. Same as Fig. 2, but for CO zonal mean trends for (a) 147 hPa, and (b) 215 hPa.

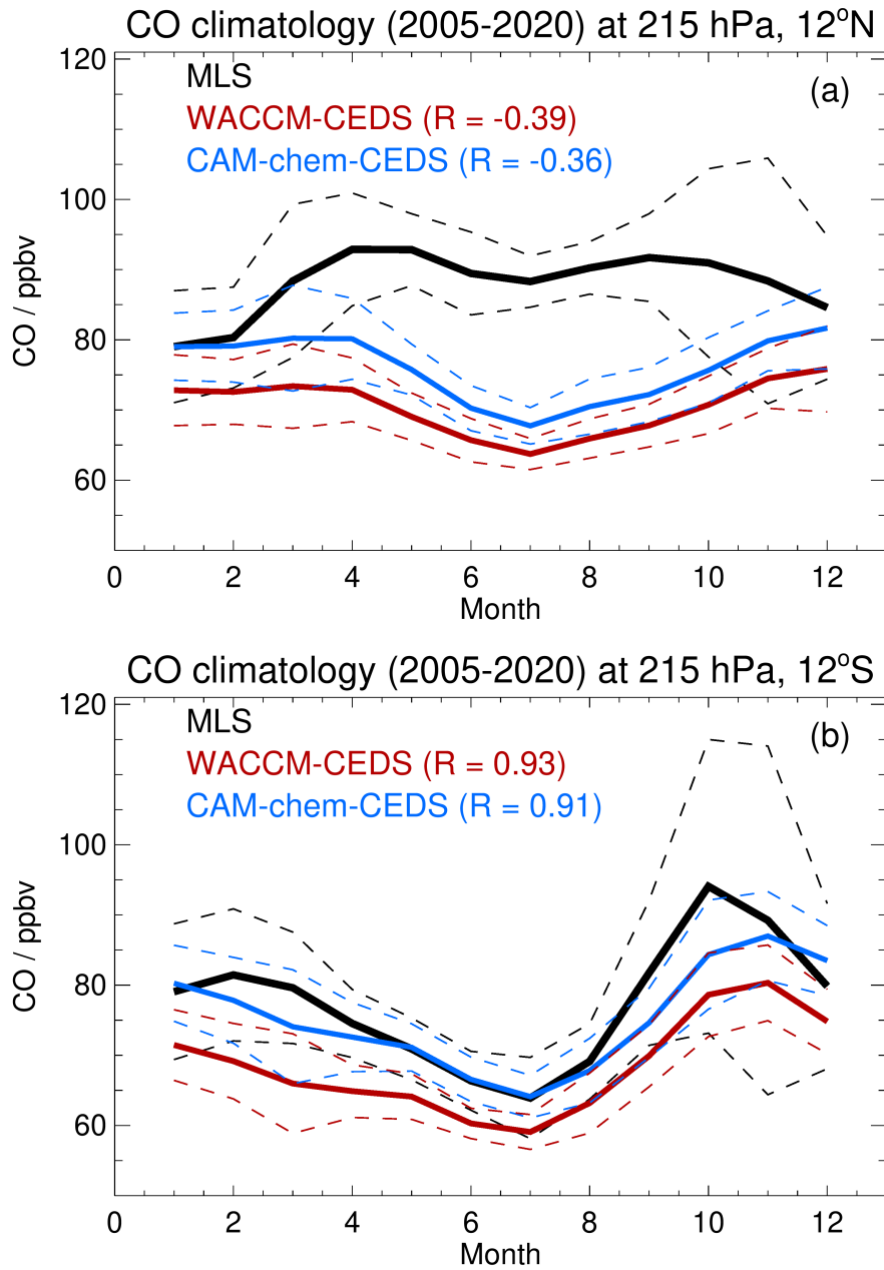
1535
 1536
 1537
 1538
 1539
 1540
 1541
 1542



1543
 1544
 1545
 1546
 1547

Figure 10. Same as Fig. 3, but for CO tropical zonal mean trends from MLS and CAM-chem-CEDS at the MLS CO UT retrieval levels of 147 and 215 hPa.

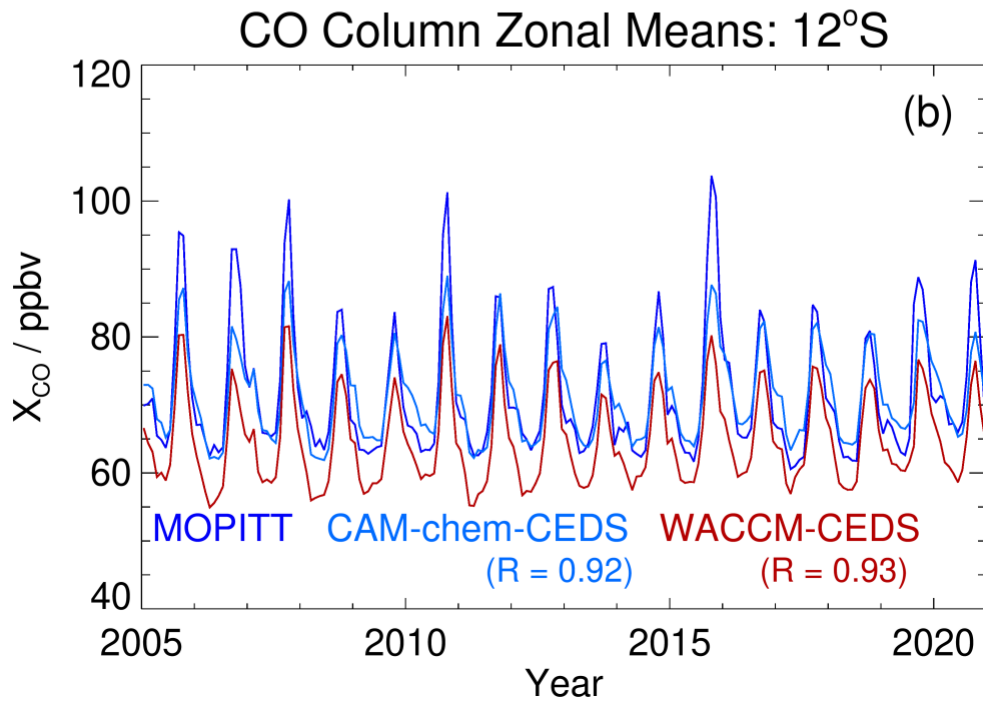
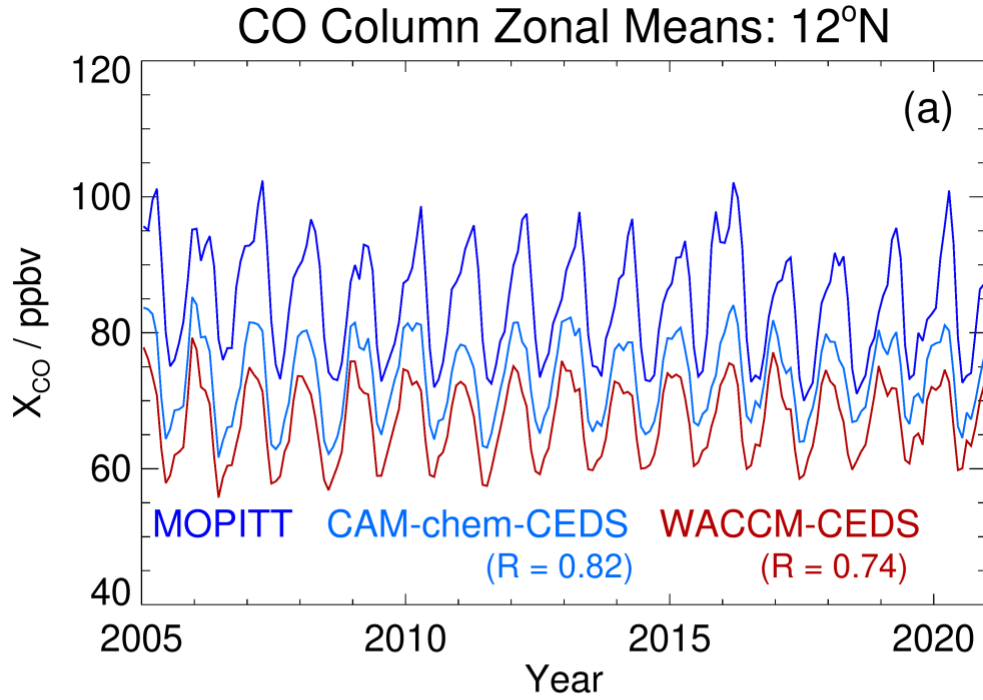
1548
1549
1550
1551
1552
1553



1554
1555
1556
1557
1558
1559
1560
1561

Figure 11. CO climatology at 215 hPa (using the 2005–2020 period) from MLS, WACCM-CEDS, and CAM-chem-CEDS for 4°-wide latitude bins centered at (a) 12°N and (b) 12°S. The thick solid lines represent the mean values from MLS (black), WACCM-CEDS (red) and CAM-chem-CEDS (blue), with corresponding variability estimates (twice the standard deviations) given by the colored dashed lines about each mean.

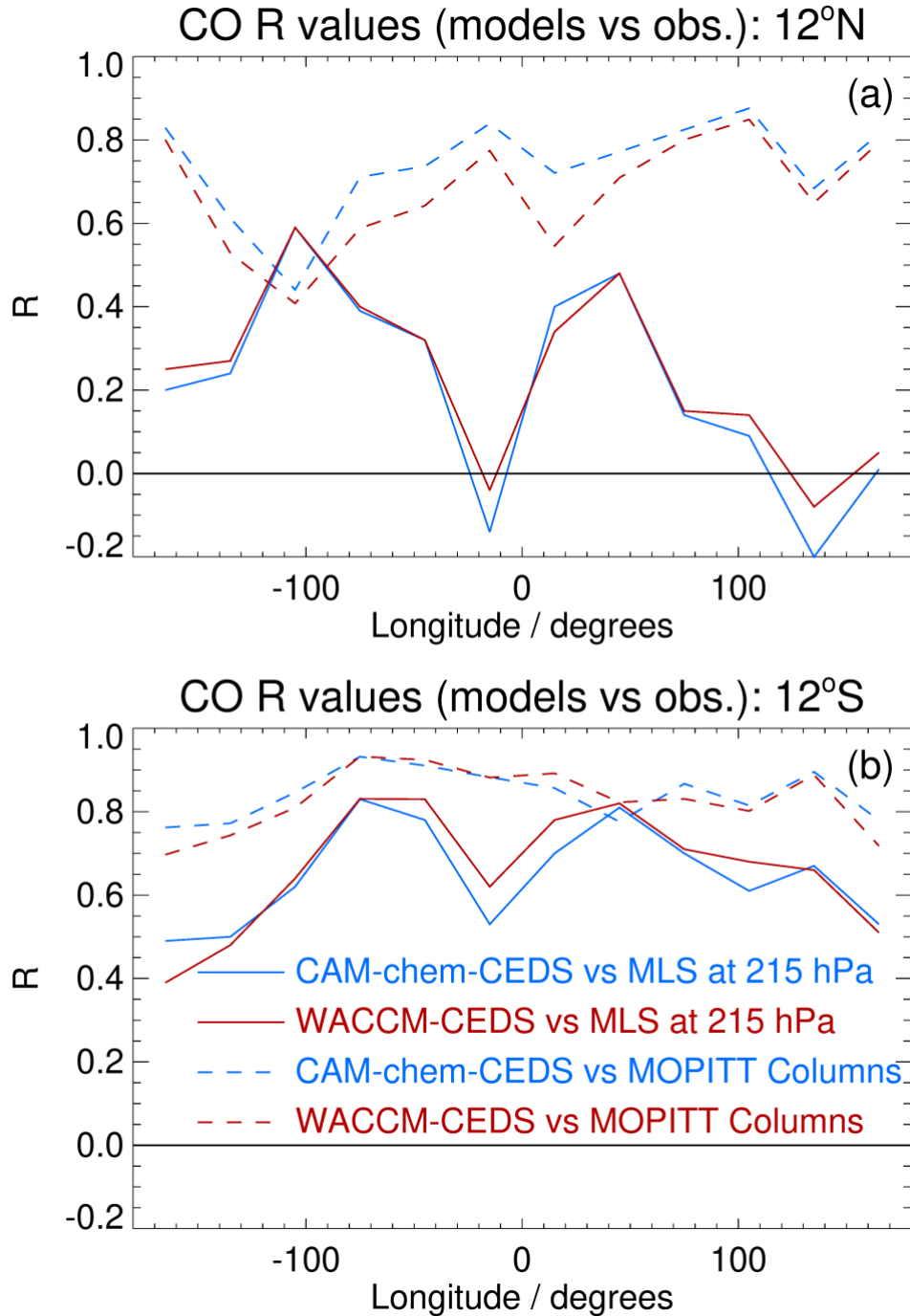
1562
1563



1564
1565
1566
1567
1568
1569
1570

Figure 12. CO column comparisons between zonal mean time series from MOPITT (purple) X_{CO} (see text) and from CAM-chem-CEDS (blue) and WACCM-CEDS (red) for 4°-wide latitude bins centered at (a) 12°N and (b) 12°S.

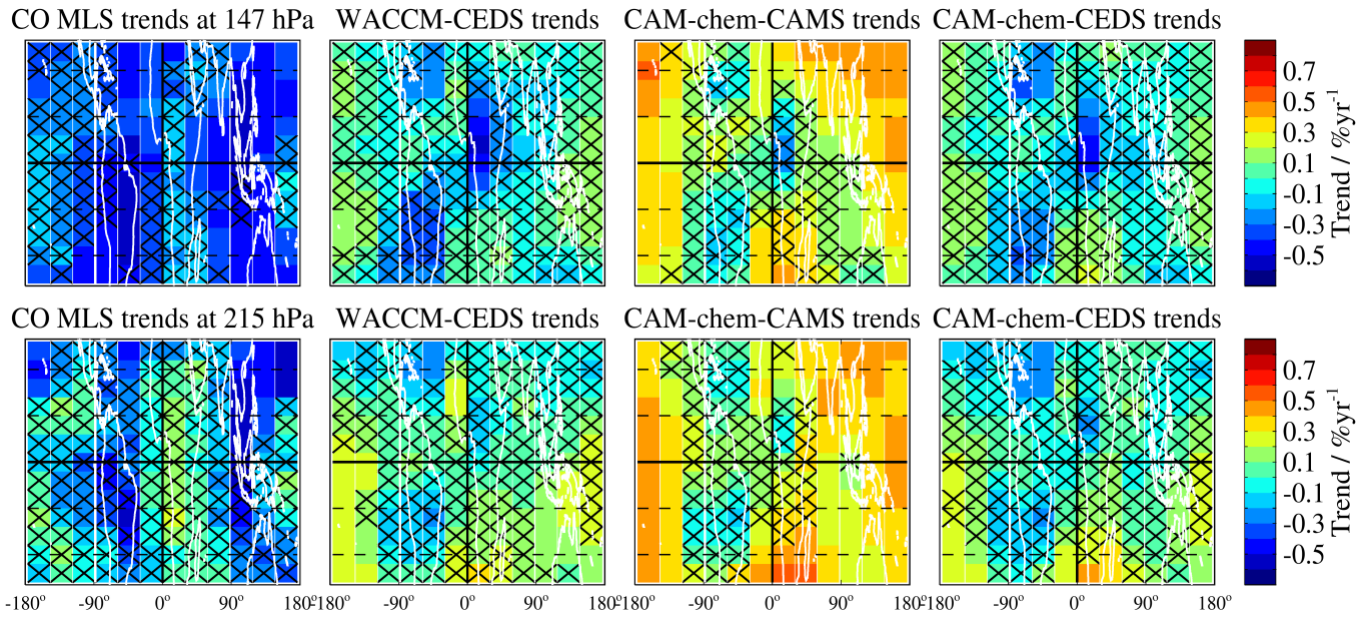
1571
1572



1573
1574
1575
1576
1577
1578
1579

Figure 13. Correlation coefficient values (R) for the zonal mean time series from the model CO columns (CAM-chem-CEDS in blue, WACCM-CEDS in red) versus MOPITT columns (dashed) and from the same two models' CO mixing ratios versus MLS CO at 215 hPa (solid) for 4°-wide latitude bins centered at (a) 12°N and (b) 12°S.

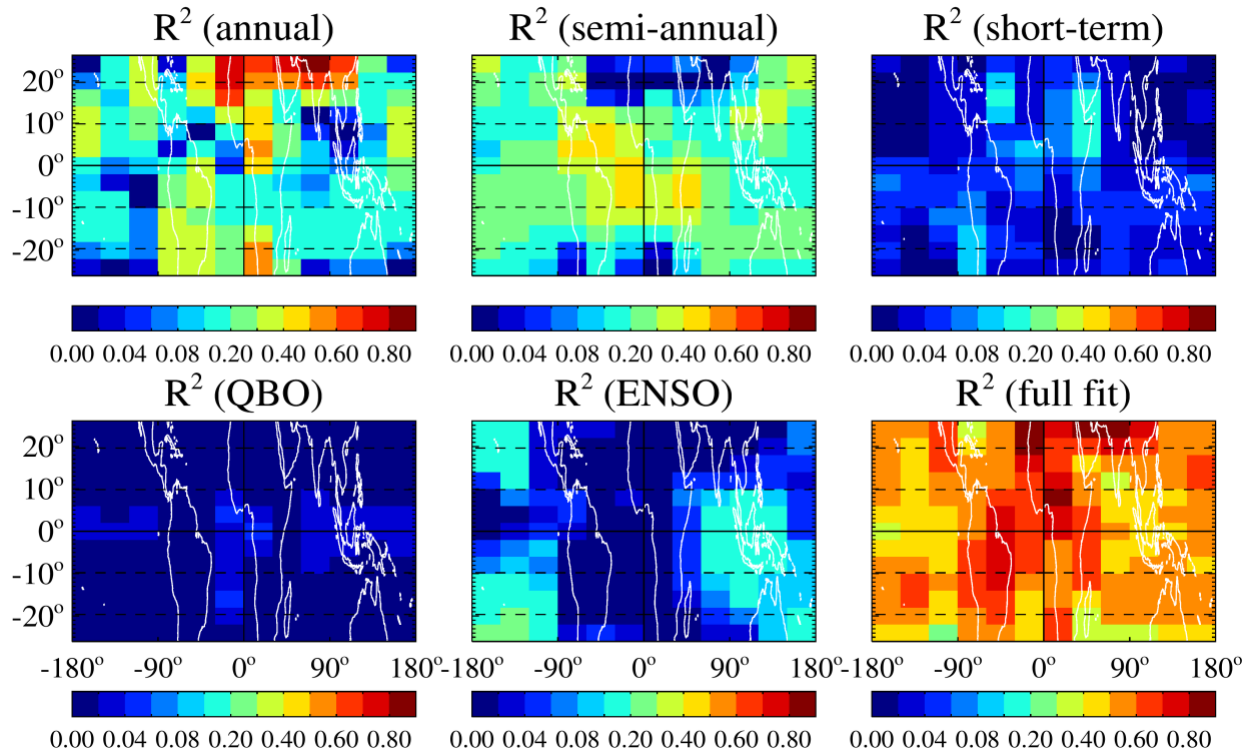
1580
1581



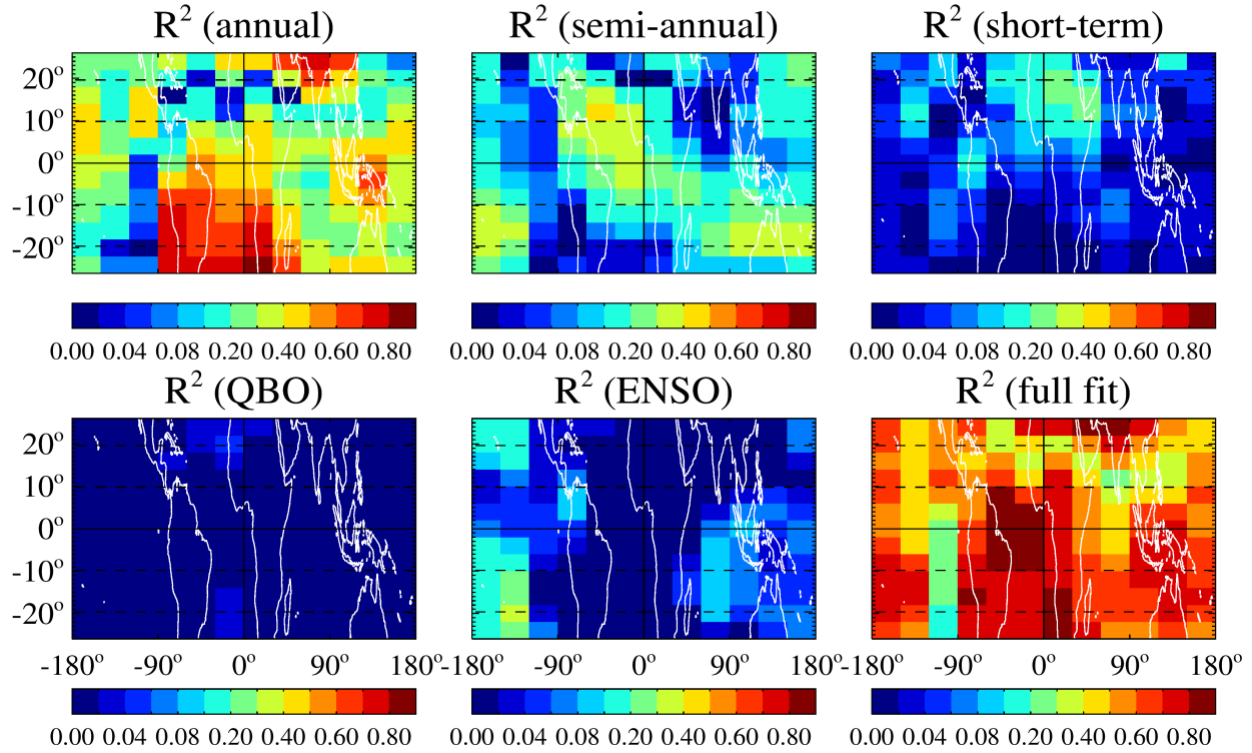
1582
1583
1584
1585

Figure 14. Same as Fig. 4, but for CO trends and all three model simulation results.

MLS CO: Variance Contributions at 147 hPa



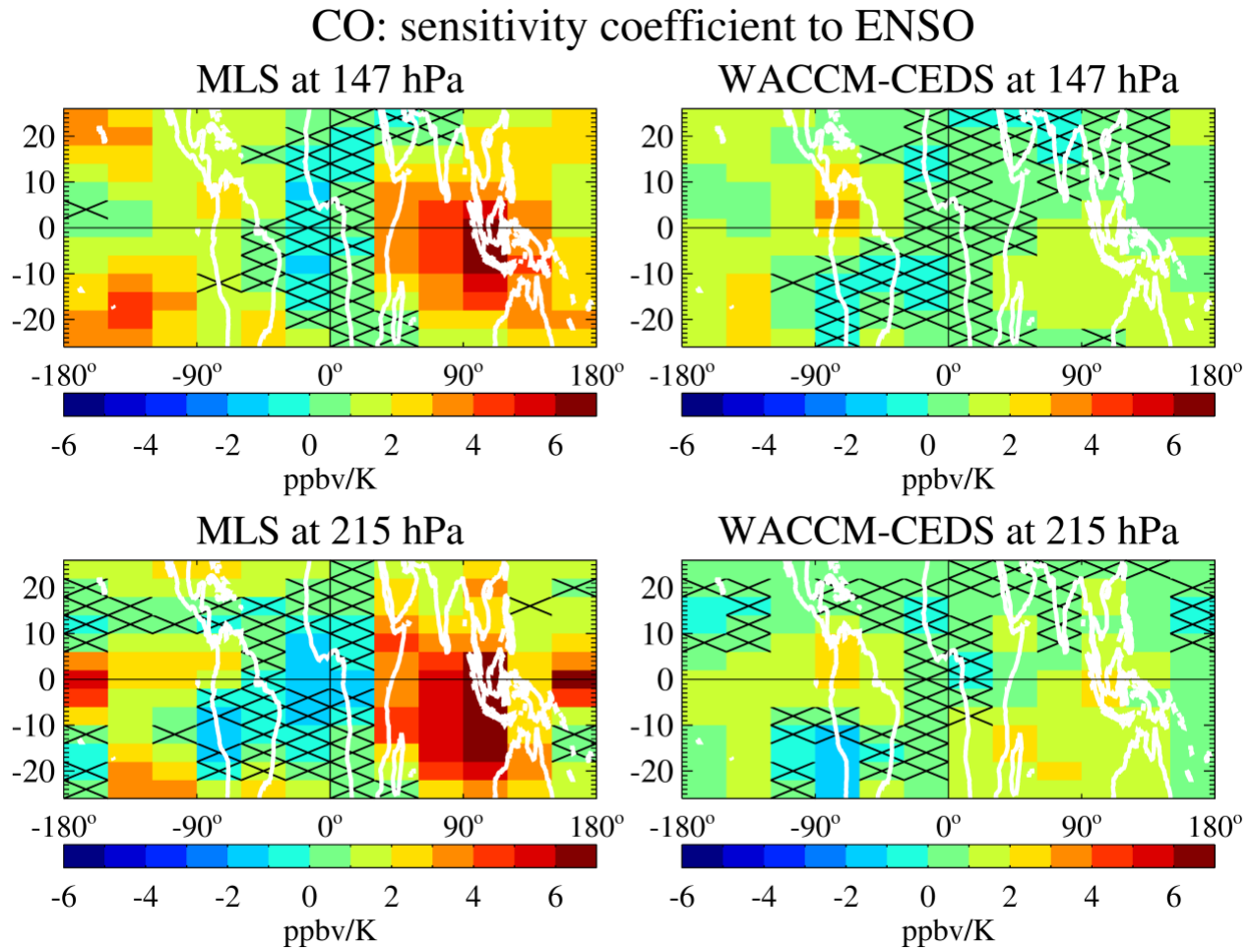
WACCM-CEDS CO: Variance Contributions at 147 hPa



1586
1587
1588

Figure 15. Same as Fig. 6, but for CO

1589
1590



1591
1592
1593
1594
1595

Figure 16. Same as Fig. 7, but for CO; unlike for O₃, there is no need here for an asymmetric color bar, but the positive range is the same as in the O₃ Figure.